DOE/ID/12079-46
ESL-62

DOE/ID/12079--46

DE82 019925

COMPUTER SIMULATION OF LOW-FREQUENCY ELECTROMAGNETIC DATA ACQUISITION

by

William A. SanFilipo

and

Gerald W. Hohmann

Earth Science Laboratory

University of Utah Research Institute

420 Chipeta Way

Salt Lake City, Utah 84108

Date Published - February 1982

Prepared for the Department of Energy

Division of Geothermal Energy

Under Contract DE-AC07-80 ID/12079

DISCLAIMER

NOTICE

This report was prepared to document work sponsored by the United States Government. Neither the United States nor its agent, the United States Department of Energy, nor any Federal employees, nor any of their contractors, subcontractors or their employees, makes any warranty, express or implied, or assumes any legal liability or responsibility for the accuracy, completeness, or usefulness of any information, apparatus, product or process disclosed, or represents that its use would not infringe privately owned rights.

NOTICE

Reference to a company or product name does not imply approval or recommendation of the product by the University of Utah or the U.S. Department of Energy to the exclusion of others that may be suitable.

CONTENTS

ABSTRACT 1
INTRODUCTION 2
ACTIVE SOURCE SIGNAL 4
SYNTHETIC NOISE 5
FREQUENCY DOMAIN DATA ACQUISITION 10
TIME DOMAIN DATA ACQUISITION 12
REMOTE REFERENCE NOISE REMOVAL 17
CONCLUSIONS 21
ACKNOWLEDGEMENTS 23
REFERENCES 24
APPENDIX A 25
FIGURE CAPTIONS 31

ABSTRACT

Computer simulation of low frequency electromagnetic (LFEM) digital data acquisition in the presence of natural field noise demonstrates several important limitations and considerations. Without the use of a remote reference noise removal scheme it is difficult to obtain an adequate ratio of signal to noise below 0.1 Hz for frequency domain processing and below 0.3 Hz base frequency for time domain processing for a typical source-receiver configuration. A digital high-pass filter substantially facilitates rejection of natural field noise above these frequencies but, at lower frequencies where much longer stacking times are required, it becomes ineffective.

Use of a remote reference to subtract natural field noise extends these low-frequency limits a decade, but this technique is limited by the resolution and dynamic range of the instrumentation. Gathering data in short segments so that natural field drift can be offset for each segment allows a higher gain setting to minimize dynamic range problems.

INTRODUCTION

Low-frequency electromagnetic (LFEM) techniques are useful where large depths of exploration are desired, such as in geothermal exploration or regional crustal studies. As an aid in optimizing signal extraction for LFEM utilizing digital data acquisition systems with in-field processing, we simulated a digital magnetic field receiver on a computer.

The basic configuration modeled consists of a vertical magnetic field signal induced by a large horizontal loop source at the surface of a homogeneous half-space, corrupted by synthetic natural field noise, and measured with a digital receiver having finite resolution and dynamic range (Figure 1). By scaling the integer word size of the analog-to-digital (A/D) converter to the anticipated dynamic range requirement, which is determined by low frequency natural field drifts, we can simulate quantization errors. Frequency domain processing consists of sin/cos correlation of the stacked data, yielding real and imaginary components or corresponding amplitude and phase. Time domain processing consists of digital integration of the stacked decay response over three time windows of different width and delay.

We generate colored synthetic noise having an amplitude spectral density matched to measured natural field spectra by low-pass filtering pseudo-random numbers and adding them to the active source signal. Included is a digital high-pass filter for enhanced noise rejection and a remote reference for noise subtraction assuming that the noise is coherent over distances large compared to the source-receiver separation.

The scheme for remote reference noise subtraction uses a least squares fit to find the transfer tensor between the base receiver field components and the horizontal field components at the remote receiver, using a short data segment recorded with the transmitter off. This accounts for both lateral conductivity change and relative alignment errors between the base and remote magnetometers. Subsequent LFEM data collection can implement the noise subtraction in real time.

ACTIVE SOURCE SIGNAL

For detection of targets having dimensions and depths to tens of kilometers, a large source moment operating at low frequencies with source-receiver separations of a few kilometers or more will be required. A one kilometer square loop carrying a current of ten amperes (equivalant source moment of 10^7 amp-m^2) would be a practical source obtainable with readily available equipment. Although data would be recorded above 0.3 Hz, we are concerned mainly with low-frequency data acquisition because of the rapidly increasing noise power with decreasing frequency.

The current is a square wave for frequency domain processing and an alternating-polarity pulse train with equal on/off times for time domain systems. The vertical magnetic induction in gammas at a distance r from a vertical magnetic dipole of moment M over a half-space of conductivity σ and free space permeability μ_0 is given by (Kraichman, 1976):

$$B = \frac{100\,M}{r^3}\left\{\frac{9-(9+9\theta^{1/2}+4\theta+\theta^{3/2})\,e^{-\theta^{1/2}}}{2\theta}\right\}$$

in which θ is given by $-i2\pi\mu_0\sigma f r^2$ and f is the frequency in Hz.

We Fourier transform the sampled current waveform with an FFT algorithm, multiply each harmonic up to the Nyquist frequency by the earth response calculated from the above expression, and inverse transform the resulting spectrum to get the signal waveform at the receiver. The examples in this paper are for a half-space resistivity of 100 ohm-m, distances of 10 km for frequency domain and 5 km for time domain, and base frequencies of 0.3 Hz, 0.1 Hz, 0.03 Hz, and 0.01 Hz. A sampling rate of 128 points/cycle is adequate for frequency domain analysis in which we are

only concerned with the fundamental, but 512 pts/cycle are used for the time domain simulations in which we desire broad-band data.

SYNTHETIC NOISE

Generation

Natural magnetic field fluctuations below 0.1 Hz have an amplitude density spectrum (defined as the square root of the average power density spectrum) that increases rapidly with decreasing frequency. Measured amplitude spectral densities shown in Figure 2 from two magnetotelluric surveys (Bostick, personnal communication) vary approximately as f-4 between 0.2 Hz and .05 Hz.

We designed a digital filter that can be applied to computer generated pseudo-random white noise so that it simulates the essential characteristics of natural field noise. In particular we are interested in the drift associated with power at periods longer than the time interval of a single segment of data. A non-recursive convolution filter with a moderate sampling frequency (e.g., 50 Hz) would be too long to be practical. Hence, recursive filtering is required for simulating the natural field spectrum.

Since a double-pole double-zero transfer function has the desired rapid falloff in the transition zone between the corner frequencies, we designed a second-order recursive (IIR) filter with empirically determined corner frequencies and gain. The design procedure in which the z-transform is found from the transfer function follows Kulhanek (1976) and Oppenheim and Schafer (1975). The filter parameters are adjusted until the amplitude spectral density adequately matches the field data as shown in Figure 2.

Normalized spectral estimates are computed from the square root of ensemble power averages; the individual power estimates are obtained from squared magnitudes of periodograms six cycles in length, windowed with a Hanning cosine bell and normalized as described by Bostick and Smith (1979).

Using normally distributed, zero-mean, unity-variance, pseudo-random white noise input, the filtered synthetic noise spectrum matches the field data spectra with the double pole at 0.01 Hz, the double zero at 0.6 Hz, and a gain of 7×10^{-4}. Synthetic noise generated continuously and processed in segments preserves continuity from one segment to the next, so that a real time data stream can be simulated in short blocks. The decreased amplitude at higher sampling rates (shown at 0.002 Hz and 0.0078 Hz) results from a combination of filter digitization alias and numerical error.

Noise Reduction by Data Processor

The estimates of the real and imaginary parts of the output of frequency domain processing of a coherent signal corrupted by white noise in which data are stacked and sin/cos correlated have a standard error of $(P/(NT))^{1/2}$ (Appendix A). Here P is the input white noise power spectral density, N is the number of cycles stacked, and T is the period of the correlator. The processing frequency response is derived in Appendix A and shown in Figure 3. Given by the expression sinc $(NT/a(\omega-\omega_i))$, it has a main lobe centered at the correlation frequency and side lobes at each harmonic of the data window. The output noise for a white noise input is proportional to the integral of the squared frequency response up to the Nyquist frequency, which is inversely proportional to the length of the data window. Generalization to colored noise is only approximate and

requires that the noise power spectral density be nearly constant within the correlation bandwidth (i.e., main lobe and adjacent side lobes).

The 0.05-Hz to 0.2-Hz band has a rapidly varying noise spectrum, so that the white noise approximation breaks down. In order to understand the influence of colored noise on the output of data processing, we performed computer experiments with simulated natural field noise. We examined the noise rejection with stacking for our colored noise by generating, correlating, and averaging real and imaginary parts for several values of N. Repeating the process about 30 times permits calculation of ensemble estimates of the correlation output variances.

Application of a digital high-pass filter is the obvious approach to reduce the low-frequency noise. The simple filter used here consists of subtracting from each data point the data value averaged over a symmetric window of width one period. The filter transfer function is $1-\mathrm{sinc}(\pi f/f_0)$. The filter response shown in Figure 4 monotonically decreases from unity at the fundamental to zero at DC, is unity at the harmonics, and has no phase shift.

Representative results of frequency domain processing of geomagnetic noise are shown in Figure 5 at 0.1 Hz and Figure 6 at 0.3 Hz and .01 Hz. At 0.1 Hz. the standard deviation of the sine correlation output (real part) of the noise is greater than the cosine output (imaginary part) for N< 200, when the input data have not been high-pass filtered. This can be understood heuristically by considering the large low-frequency power as approximately a linear drift (W. R. Sill, personal communication) so that:

$$\frac{1}{NT}\int_0^{NT}(at)\sin\left(\frac{2\pi t}{T}\right)dt = \frac{a}{NT}\left[\left(\frac{T}{2\pi}\right)^2\sin\left(\frac{2\pi t}{T}\right)-\left(\frac{tT}{2\pi}\right)\cos\left(\frac{2\pi t}{T}\right)\right]\Bigg|_0^{NT}$$

$$= -aT/2\pi$$

and

$$\frac{1}{NT}\int_0^{NT}(at)\cos\left(\frac{2\pi t}{T}\right)dt = \frac{a}{NT}\left[\left(\frac{T}{2\pi}\right)^2\cos\left(\frac{2\pi t}{T}\right)+\left(\frac{tT}{2\pi}\right)\sin\left(\frac{2\pi t}{T}\right)\right]\Bigg|_0^{NT}$$

$$=0$$

Thus low-frequency noise is not distributed equally into the real and imaginary parts.

Extrapolating back from N=400 (where the bandwidth is narrowest and the white noise approximation best) in Figure 5 we see that the imaginary part does fall off as $N^{-1/2}$ but the real part falls off significantly faster for unfiltered input noise. The high-pass digital filter applied to these data will be discussed in a later section. At 0.01 Hz (Figure 6) the white noise approximation holds for both real and imaginary parts and they are nearly equal, but at 0.3 Hz the effects of the color are even more pronounced than at 0.1 Hz.

Output noise decreases with increasing correlation period for a given number of cycles stacked with white noise input, because the data window length increases. However, with similated natural field noise input, the output noise increases with period as seen in Figure 6 because the noise power within the correlation pass band increases.

Time domain processing implies a broad band response to noise. Our computer experiment for examining time domain noise reduction consists of digitally integrating synthetic noise over periodic time windows of length $S<T/2$ and stacking with alternating polarities. The output is recorded for several values of N. Repeating this process about 30 times we calculate

ensemble r.m.s. estimates of the noise as a function of N.

The theoretical white noise standard error derived in Appendix A is $(P/(2NS))^{1/2}$. There is a contribution from each of the odd harmonics of the base frequency, as shown by the frequency response in Figure 6. Note that, in both time and frequency domain, white noise rejection is proportional to the square root of the total integration time. However, in the time domain this rejection is independent of the base frequency.

The time domain output noise for simulated natural field noise input, shown in Figure 8, has a stacking fall-off rate faster than $N^{-1/2}$ for base frequencies above 0.1 Hz. The output noise decreases with base frequency $f = 1/T$ and is insensitive to the integration window length S: quadrupling S at 0.1 Hz resulted in almost exactly the same noise output per unit integration time and is therefore not shown.

In Figure 7 we see that the locations of the pass bands are determined by the base frequency. Thus for colored noise, the noise levels within the pass bands depend on the base frequency. Since the noise power decreases rapidly with frequency, only the pass band centered at the base frequency is important. The effect of the integration over S is to reduce the contribution of each peak by the factor $\mathrm{sinc}(n\pi fs)$, which is significantly less than one only at the higher harmonics, since $S \ll T$. If the input noise is not band-limited, as $S \to 0$ the output noise becomes infinite. However, in practice the input noise is band-limited by sampling, so that output noise approaches a finite limit.

Although true natural field noise may have important characteristics, such as non-stationarity and coherent wavetrains not incorporated in our

synthetic noise, our results show that theoretical analysis for white noise is not generally applicable.

FREQUENCY DOMAIN DATA ACQUISITION

Having analyzed some aspects of pure noise behavior, we now consider the running average of correlation output as data consisting of a coherent signal corrupted by natural field noise are stacked. We generate the EM signal as previously described, introduce the instrument response for a 2-pole anti-alias filter using an FFT algorithm, and correlate to get the desired signal. Our results show that the correlation output using an 8-bit sine table is not significantly different from that with full floating-point precision.

Analog to digital (A/D) quantization errors in the noise-free signal are introduced and the correlation repeated for reference. The noise is added to the full precision signal in one-period segments, quantization errors are incorporated in the resulting sum, sin/cos correlation is applied, and running averages of the real and imaginery output are recorded. We specify the dynamic range of the A/D converter, and monitor the number of times the data stream drifts off scale, assuming the offset is re-zeroed each time. The appropriate dynamic range can be judged by experience; quantization errors are a problem if they are comparable to residual natural field noise when the dynamic range is expanded (resolution reduced) to eliminate off-scale drifts. Results show that, for reasonable stacking times, residual natural field noise is always much greater than quantization errors.

An example of running average correlation output at 0.3 Hz in Figure 9

shows that the real part behaves erratically, especially for small values of N. The error bars at 64 cycles and 100 cycles indicate the ensemble standard deviation; the correlation outputs wander in and out of the expected error range during stacking. We also observe the low-frequency noise corrupting the real part much more than the imaginary part. The improved convergence of the real part after high-pass filtering at 0.3 Hz is dramatic.

The error that remains after 60 cycles for the filtered data is random error although the convergence is quite smooth. In this particular example, the results are within one standard deviation up to 60 cycles of data but outside one standard deviation from 60 to 100 cycles of data. We thus emphasize the statistical interpretation of the expected noise as a function of cycles stacked; a single sample of data behaves much like a random walk process. The error bars are a better measure of the improvement with the high-pass filter than the smoothing of a single data sample. More than one independant sample of data should always be taken in the field to verify reproducibility.

Figure 10 shows the corresponding running average amplitude and phase. Again, the filtered output converges in a smoother manner, but the influence of noise can linger after the appearance of convergence, demonstrating the need to make repeat measurements. The ratio of signal to noise after 100 cycles of filtered and stacked data at 0.3 Hz is quite good. The example in Figure 11 using 0.1 Hz data appears qualitatively similar to that for 0.3 Hz data; the corresponding amplitude and phase are shown in Figure 12. Since noise characteristics are defined in a statistical sense, over short time intervals the noise has varying features

that can corrupt data in a randomly time-varying fasnion. In these first two examples, the corrupting effect of the noise is essentially uniform during stacking. Another example at 0.1 Hz shown in Figure 13, with amplitude and phase in Figure 14, demonstrates the effect of a rapid noise drift during the first cycle of stacking during which the real component is more highly corrupted than during subsequent cycles. The noise is stationary in a statistical sense, but short segments have varied characteristics.

Figures 15 and 16 show that the high-pass filter becomes only marginally effective at .03 Hz. As shown by in Figures 17 and 18, the high-pass filter is totally ineffective at .01 Hz. Since the noise power is large below .03 Hz, noise near the signal frequency is the source of signal corruption at these low frequencies and something better than filtering and stacking is needed. Stacking 100 cycles of data requires an hour of recording at .03 Hz and three hours at .01 Hz. To remove noise near the signal frequency we need to subtract the noise waveform using a remote reference, as discussed later.

TIME DOMAIN DATA ACQUISITION

Some of the advantages of broad-band time domain data over frequency domain data have been discussed elsewhere (McCracken et al., 1980). Collection of broadband data without frequency switching is an obvious example. Because measurements are made during periods in which there is no primary field to obscure the scattered fields, large depth of exploration does not require large source-receiver separations, and orientation and location errors have only a second-order effect. Also, the response from a deep target separates in time from the response from shallow geologic

noise. However, the problems concerning time domain digital data acquisition in the presence of natural field noise must be addressed in order to anticipate problems and limitations of the technique. We are particularly interested in deep exploration requiring a low base frequency and late-time data.

In our simulation, data are sampled and recorded continuously during both on-times and off-times at a constant sampling rate after conditioning the signal with the two-pole anti-alias filter. This technique permits the application of the same digital high-pass filter used in the frequency domain, but measurements must be made with the primary field on. In order to maintain a large bandwidth it is essential to use as high a sampling rate as possible; we have used 512 points/cycle so that the off-time transient is sampled at 128 points. The cut-off frequency of the anti-alias filter is a decade below the sampling frequency; thus the higher harmonics are altered and phase shifted. Consider the three data channels shown in Figure 19 in which data are integrated digitally. The first (CH-1) is an early time example and only one point is used, namely the fifth point of the 128-point off-time. The mid-delay channel (CH-2) sums four points starting at the 17th, and the late time channel (CH-3) sums 16 points starting at the 65th point.

The half-space decay at 0.1 Hz base frequency 5 Km from the source is shown in Figure 19, along with the same signal after including the alias-filter response. The basic decay pattern is: a rapid falloff, an undershoot, and an asymptote. The instrument response essentially delays and broadens this pattern; the first channel even changes sign.

An important practical consideration when broad-band data are taken is

that removal of instrument response requires a deconvolution operation, which in turn requires obtaining the instrument transfer function at all harmonics. The deconvolution must be done before digital integration and requires a full cycle of data; we have omitted this step in our simulation examples. A field receiver requires the capability of performing an FFT to accomplisn this deconvolution.

A/D quantization errors are more pronounced with time domain data than with frequency domain data, especially at late times when signal levels are low. However, for such low signal levels, residual natural field noise after high-pass filtering and stacking will be greater than the signal. Hence, quantization errors will be a limitation only when a remote reference is used, which will be demonstrated in a later section.

Convergence of simulated time domain data stacking is shown in Figures 20, 21 and 22 for both unfiltered and high-pass filtered data at 0.3 Hz, 0.1 Hz, and .03 Hz base frequencies respectively. At 0.3 Hz with the aid of the filter we can get good data even at the late channel, which starts at about 420 ms delay. The improvement with the high-pass filter is similar to the improvement of the real component of the frequency domain results in which the erratic behavior, especially for small N, is dramatically reduced.

The ratio of signal to noise is much worse at 0.1 Hz base frequency. As shown in Figure 21 only the first channel converges to within 5% of the noise-free signal, and there is 30% error in the second channel. Note that because of the lower cutoff frequency of the anti-alias filter, the signal is nigher for the same delay but lower base frequency. Comparing these two cases indicates that the ratio of signal to noise is not determined

entirely by the signal level or delay time; channel 3 at 0.3 Hz at 420 ms delay is within about 10% but channel 2 at 0.1 Hz beginning at a delay of 330 ms is off by 30%. At first we might attribute this to the increased integration time for the late time channel, but the previous analysis of the pure noise response indicates that the base frequency determines the noise bandwidth center frequency and there is much more noise power at 0.1 Hz than at 0.3 Hz. To demonstrate that longer integration times do not improve late time signal/noise, we repeated the 0.1 Hz channel 3 simulation with the integration time extended to the end of the off time, quadrupling the number of points averaged. The results in Figure 23 demonstrate there is no improvement in the signal/noise ratio and the output pattern during stacking is nearly identical. This is because the noise is highly correlated over time intervals as long as our integration windows.

Unless the target response is substantial below 0.3 Hz, there is no motive to use later time channels requiring lower frequencies. However, if the target responds at times later than 420 ms, the data at later times would have reduced geologic noise.

Monitoring the number of times the signal plus noise drifts outside the range of the A/D converter indicates how much gain might be appropriate for a given data stacking time. With a range of 0.2γ the field typically drifts off scale between 0-10 times during 100 cycles of 0.3 Hz data or 5.6 minutes of recording time, indicating a somewnat lower gain should be used. Using half the gain (doubling the range) at 0.1 Hz also results in about 5 off-scale drifts corresponding to fluctuations of a fewγ in 15 minutes. This gives an idea of typical dynamic range requirements and the corrresponding resolution of the A/D converter.

We incorporated a simple one-pole analog prewhitener with a corner frequency that can be set to either .0016 Hz or .016 Hz to see if analog prewhitening would allow a higher gain. Using the high corner frequency for data above .03 Hz reduces the number of off-scale drifts by about 1/2, which will not allow for a significantly higher gain setting to increase the A/D converter resolution. For lower frequencies the corner frequency was set at .0016 Hz and simulations showed no reduction in the number of off-scale drifts.

REMOTE REFERENCE NOISE REMOVAL

Remote reference noise subtraction can extend the low frequency limit of EM data collection well below the practical limits discussed above. The concept is simple: natural magnetic field fluctuations are laterally coherent so that they can be measured at a remote site and subtracted from the noise-corrupted signal at the base receiver. The waveforms will not be identical at the two sites, but a relative amplitude scale factor and a bias can account for most of the discrepancy. Three-dimensional conductivity distributions and relative misalignment of the magnetometers result in a tensor relationship between orthogonal components of the natural magnetic fields at the two sites. The noise in a single component, $H_i^B(t)$, at the base site is approximately a linear combination of the two horizontal components of the fields at the remote site:

$$H_i^B(t) \cong a\, H_x^R(t) + b\, H_y^R(t) + c$$

One possible field technique records the natural field with the transmitter off and calculates least-square estimates of the coefficients a and b. We simulate this process by generating two independent synthetic noise streams corresponding to the horizontal field components at the remote site, and by specifying the transfer tensor and instrument bias to calculate the noise at the base site. We then incorporate A/D quantization errors to each data stream and use a least squares algorithm to calculate the transfer tensor coefficients from the data, as would be done in the field. The coherent signal is then included at each site, with the distance from the remote site to the source five times that of the base site to source. Noise subtraction using the calculated transfer tensor is simulated with both time and frequency domain processing.

The main limitation of this remote reference technique arises from the quantization errors. Since the signal/noise ratio of the raw data is low, only a fraction of the instrument dynamic range is used to resolve the signal. The quantization errors of the digitized data can lead to substantial residual numerical errors after noise removal. If the quantization errors are random and uncorrelated, they stack or average as white noise, and if they are a moderate fraction of the signal, stacking data would be effective in removing them and would not require an impractical amount of data. However, in our scheme the residual error is not totally random, since the remote site data and base site data are linearly dependent. For weak late-time signals, the quantization errors can be larger than the signal.

Remote reference telemetry resolution and dynamic range are simulated in the same fasnion as we simulate quantization for the A/D converter; this method of simulation is appropriate for digital telemetry but only approximate for analog telemetry. A typical F.M. telemetry system has a ratio of signal to noise equivalent to 8 bits of resolution; a good digital telemetry system nas 12-bit resolution. In order to minimize the required dynamic range, data should collected in short segments so that the instrument offset can be set to zero each time to account for natural field drifts. In our simulation examples we used 2 periods of calibration with the signal off and 10 periods of data with the transmitter on. The transfer tensor coefficients were 0.7 and 0.2, corresponding to highly coherent and weakly coherent fields.

Frequency Domain

We simulate results for a receiver at 10 Km and frequencies of .03 Hz and .01 Hz using a 12-bit base station receiver and 8-bit telemetry. Figures 24 and 25 show the running average output as data are stacked at .03 Hz and .01 Hz respectively.

Errors in calculating the transfer tensor coefficients from the calibration data with the signal off are not as important as errors in the subsequent noise subtraction. Quantization errors are a small percentage of the total noise utilized by the least squares algorithm but a large percentage of the signal. Using 12-bit telemetry substantially improves the results at .01 Hz, and a corresponding plot of the running average convergence has no scatter as shown in Figure 25. The remaining bias error arises from subtraction of the signal at the remote site.

Time Domain

We have seen that at 0.1 Hz base frequency without a remote reference it is difficult to acquire time domain data to within better than 30% for our second channel. With the remote reference we can get this channel to within 2%, and the late-time channel, shown in Figure 26, is now within 20% using 12-bit base site data and 8-bit telemetry. Comparing this to the results using 8-bit base site data and 8-bit telemetry indicates results just as good for the early and mid-time channels and somewhat worse at late times. Using 12-bit base site data and 12-bit telemetry improves the second channel convergence, leaving a 1.5% bias from the signal at the remote site. The third channel has improved as shown in Figure 26, although it varies over a 10% range in the 8 cycles of stacking because of

quantization errors and is biased by 10% due to the signal at the remote site.

The frequency domain results verify the approximate R^{-3} halfspace field attenuation prediction of a bias less than 1% for the fundamental frequency, with the remote site 5 times the distance of the base site from the source. The distance dependence of the signal in the time domain is not so simple: the attenuation for a particular integration window is much less than R^{-3} in these examples. Although the primary or on-time field level is reduced by approximately R^{-3}, the decay response during off-times from currents induced in the half-space is broadened or stretched in time as distance increases. In order to exploit the advantage of greater target sensitivity with time domain data, placing the remote reference at a greater distance may be required.

At .03 Hz base frequency the second channel varies over about 20% during stacking with 8-bit telemetry and converges quickly to within 1% with 12-bit telemetry as shown in Figure 27. The late time channel is not particularly useful at or below .03 Hz even with 12-bit telemetry. Noting that the second channel corresponds to nearly the same delay as the late channel at 0.1 Hz, the seemingly better results at .03 Hz can be attributed to the slower decay response of the anti-alias filter at the lower frequency resulting in a larger signal. If deconvolution to remove the instrument response is performed, this effect would be eliminated and the higher frequency results would be better because of the higher instrument gain.

CONCLUSIONS

By simulating on a computer the essential aspects of digital LFEM data acquisition and processing, we have analyzed the capability of the measuring system in estimating a coherent signal corrupted by natural field noise.

The system output for colored noise is different from that for white noise. For example, the real component of frequency domain output is corrupted more than the imaginary component. The rate of noise rejection with data stacking is not $\sqrt{N}$ for moderate N above 0.3 Hz, where N is the number of cycles stacked.

A digital high-pass filter reduces the low-frequency noise and substantially improves convergence at frequencies above 0.1 Hz. At frequencies below 0.3 Hz in the time domain and 0.1 in the frequency domain, an impractical amount of data acquisition time would be required to obtain an adequate signal to noise ratio. The high-pass filter is ineffective below 0.1 Hz because noise near the base frequency is large; subtraction of the noise waveform is necessary.

Remote reference noise removal is possible since natural magnetic fields are coherent over distances in which the LFEM signal attenuates. The lateral changes in the noise waveform can be described approximately by a transfer tensor relating horizontal components of the magnetic field at the remote site to the components at the base site. The tensor coefficients can be found with a least squares algorithm utilizing data acquired with the transmitter off.

Application of the remote reference scheme is limited by the resolution and dynamic range of the instrumentation. To ensure that the signal level is higher than instrument noise, the highest practical gain should be used at the magnetometer output. Natural field drift will then require more frequent re-zeroing of the instrument offset.

The analysis we have presented can be used to assess qualitatively any problems with induced polarization data acquisition in mining and oil exploration. Although the ratio of signal to telluric noise would be better for typical field configurations, more stringent demands on data accuracy would also be required. The desire to obtain data at low frequencies in order to minimize elecromagnetic (EM) coupling motivates consideration of telluric noise corruption and instrument resolution problems.

ACKNOWLEDGEMENTS

We wisn to thank John Stodt and Bill Sill for valuable discussions, and Francis Bostick for providing the natural field amplitude density spectrum.

We gratefully acknowledge the financial support provided under U.S. Department of Energy, contract number DE-AC07-80 ID/12079.

REFERENCES

Bostick, F. X. Jr., and Smith, H. W., 1979, Development of real-time, on-site methods for analysis and inversion of tensor magnetotelluric data: University of Texas at Austin, Final Technical Report No. 206.

Kraichman, M. B., 1976, Handbook of electromagnetic propagation in conducting media: U.S. Government Printing Office, 76 p.

Kulhanek, O., 1976, Introduction to digital filtering in geophysics: Amsterdam, Elsevier, 168 p.

McCracken, K. G., Hohmann, G. W., and Oristaglio, M. L., 1980, Why time domain?: The Geophysics of the Elura Orebody, Cobar, NSW: Aust. Soc. of Explor. Geophysicists, p. 176-179.

Oppenheim, A. V., and Schafer, R. W., 1975, Digital signal processing: Englewood Cliffs, New Jersey, Prentice Hall, 585 p.

Papoulis, A., 1977, Signal analysis: New York, McGraw Hill, 431 p.

APPENDIX A

NOISE REDUCTION

Frequency Domain

In frequency domain processing, data are multiplied by $\sin\omega_0 t$ and $\cos\omega_0 t$; and integrated for N periods T, where $T=2\pi/\omega_0$. Input x(t) and output y(t), are related by:

$$Y(t) = \frac{i}{NT}\int_{t-NT}^{t} X(\tau)\, e^{-i\omega_0[\tau-(t-NT)]}\, d\tau, \qquad (A\text{-}1)$$

with real and imaginary parts given by:

$$Y_r(t) = \frac{1}{NT}\int_{t-NT}^{t} X(\tau)\, \sin[\omega_0(\tau - t + NT)]\, d\tau, \qquad (A\text{-}2)$$

and

$$Y_i(t) = \frac{1}{NT}\int_{t-NT}^{t} X(\tau)\, \cos[\omega_0(\tau - t + NT)]\, d\tau, \qquad (A\text{-}3)$$

respectively.

Noting that

$$e^{-i\omega_0 NT} = e^{-i2\pi N} = 1,$$

we have

$$Y(t) = \frac{i}{NT}\int_{t-NT}^{t} X(\tau)\, e^{i\omega_0(t-\tau)}\, d\tau. \qquad (A\text{-}4)$$

In terms tne system impulse response h(t), the output is given by

$$Y(t) = \int_{-\infty}^{\infty} X(\tau)\, h(t-\tau)\, d\tau, \qquad (A\text{-}5)$$

Comparing (A-4) and (A-5) we see that

$$h(t-\tau) = \frac{i}{NT} P_{NT}\left(\tau - t + \frac{NT}{2}\right) e^{i\omega_0 (t-\tau)},$$

where the pulse function $P_\Delta(t)$, controlling the integration length, is given by

$$P_\Delta(t) = \begin{cases} 1 : & -\Delta/2 \le t \le \Delta/2 \\ 0 & \text{otherwise} \end{cases}.$$

Thus

$$h(-\tau) = \frac{i}{NT} P_{NT}\left(\tau + \frac{NT}{2}\right) e^{-i\omega_0 \tau},$$

and

$$h(\tau) = \frac{i}{NT} P_{NT}\left(\tau - \frac{NT}{2}\right) e^{i\omega_0 \tau}, \qquad (A-6)$$

since

$$P_\Delta(-t) = P_\Delta(t).$$

Now we can find the system function by Fourier transforming each term in (A-6) and using the convolution theorem:

$$H(\omega) = \frac{i}{2\pi} e^{-i\omega \frac{NT}{2}} \operatorname{sinc}\left(\frac{\omega NT}{2}\right) * 2\pi\,\delta(\omega - \omega_0),$$

or

$$H(\omega) = i e^{-i(\omega-\omega_0)\frac{NT}{2}} \operatorname{sinc}\left[\frac{NT}{2}(\omega - \omega_0)\right], \qquad (A-7)$$

since convolution with a delta function shifts the function to the position of the delta function.

In the case of digital processing, the system function consists of (A-7) and repetitions of it at integral multiples of the sampling frequency. Within the Nyquist-frequency band the discrete system function is not significantly different from (A-7).

The output variance for zero-mean stationary input noise with power spectrum $S_{xx}(W)$ is (Papoulis, 1977):

$$\sigma^2 = R_{yy}(0) = \frac{1}{2\pi}\int_{-\infty}^{\infty} S_{xx}(\omega)\,|H(\omega)|^2\,d\omega$$

where

$$R_{yy}(\tau) = \mathcal{F}^{-1}\{S_{yy}(\omega)\}$$

is the autocorrelation of the output noise, with $S_{yy}(\omega)$ its power spectrum. If the input noise is white, with $S_{xx}(\omega) = P_o$, then

$$\sigma^2 = \frac{P_o}{2\pi}\int_{-\infty}^{\infty} \mathrm{sinc}^2\left[\frac{NT}{2}(\omega-\omega_o)\right]d\omega = \frac{P_o}{NT}. \qquad (A\text{-}9)$$

Thus if the noise power spectrum is a slowly varying function of frequency, so that for N large enough it is approximately constant and equal to $S_{xx}(\omega_i)$ within the important lobes of the sinc function, the output variance is approximately $S_{xx}(\omega_o)/NT$.

Time Domain

The time domain processing consisting of stacked integrations over a window of width S at a base frequency 1/T with alternating polarity relates input x(t) and output y(t) at t = NT by

$$Y(NT) = \frac{1}{N_S}\sum_{n=0}^{N-1}\int_{(N-n)T-S/2}^{(N-n)T+S/2}\frac{1}{2}\left[X(\tau) - X(\tau+T/2)\right]d\tau \qquad (A\text{-}10)$$

Comparing (A-10), (A-5) and Fig. A.1, we see that we can express h(t) as a convolution of the integration pulse window $P_S(t)$ with the dirac comb defined by

$$D_\Delta(t) = \sum_{n=-\infty}^{\infty}\delta(t-n\Delta)$$

and multiplied by the stacking-time pulse function $P_{NT}\left(t-\frac{NT}{2}+s/2\right)$:

$$h(t)=P_s(t)*\tfrac{1}{2}\left[D_T(t)+D_T(t+T/2)\right]\cdot P_{NT}\left(t-\tfrac{NT}{2}+s/2\right). \qquad (A\text{-}11)$$

The system function H(ω) is found using the convolution theorem and the shifting property of the Fourier transform for the negative dirac comb. First we Fourier transform each term:

$$\mathcal{F}\left\{P_{NT}\left(t-\tfrac{NT}{2}+s/2\right)\right\}=e^{-i\omega\left(\frac{NT-s}{2}\right)}\,\mathcal{F}\left\{P_{NT}(t)\right\}$$

$$=e^{-i\omega\left(\frac{NT-s}{2}\right)}(NT)\,\mathrm{sinc}\left(\tfrac{\omega NT}{2}\right)$$

$$\mathcal{F}\left\{P_s(t)\right\}=s\cdot\mathrm{sinc}\left(\tfrac{\omega s}{2}\right)$$

$$\mathcal{F}\left\{D_T(t)-D_T(t+T/2)\right\}=\tfrac{2\pi}{T}\left\{1-e^{i\omega T/2}\right\}D_{\frac{2\pi}{T}}(\omega)$$

Then the convolution theorem is applied:

$$H(\omega)=\tfrac{1}{4\pi Ns}\,e^{-i\omega\left(\frac{NT-s}{2}\right)}\cdot(NT)\cdot\mathrm{sinc}\left(\tfrac{\omega NT}{2}\right)*$$

$$(s)\cdot\mathrm{sinc}\left(\tfrac{\omega s}{2}\right)\cdot\left(\tfrac{2\pi}{T}\right)\cdot D_{\frac{2\pi}{T}}(\omega)\left\{1-e^{i\omega T/2}\right\}$$

$$=\tfrac{1}{2}e^{-i\omega\left(\frac{NT-s}{2}\right)}\,\mathrm{sinc}\left(\tfrac{\omega NT}{2}\right)*$$

$$\sum_{n=-\infty}^{\infty}\mathrm{sinc}\left(\tfrac{n\pi s}{T}\right)\delta\left(\omega-\tfrac{2\pi n}{T}\right)\left[1-e^{-i\omega T/2}\right]$$

$$H(\omega)=\tfrac{1}{2}\left[1-e^{-i\omega T/2}\right]\sum_{n=-\infty}^{\infty}\mathrm{sinc}\left(\tfrac{n\pi s}{2}\right)\mathrm{sinc}\left[\tfrac{NT}{2}\left(\omega-\tfrac{2\pi n}{T}\right)\right]\cdot$$

$$e^{-i\left(\frac{NT-s}{2}\right)\left(\omega-\frac{2\pi n}{T}\right)} \qquad (A\text{-}12)$$

The magnitude of this transfer function using five terms in the sum is shown in Figure 6 in the text. Stacking without alternating polarity would result in an additional, deleterious pass-band centered at zero frequency.

To determine the output variance for time domain processing we use discrete data with $S = M\Delta t$. Then

$$Y(NT) = \frac{1}{N}\sum_{n=0}^{N-1}\frac{1}{M}\sum_{m=0}^{M-1}\frac{1}{2}\left[X(nT+m\Delta t) - X((n+\tfrac{1}{2})T + m\Delta t)\right].$$

The input is the sum of a deterministic signal and stationary white noise. Denoting the input variance $V\{X(n\Delta t)\}$ by σ_x^2 and the output variance $V\{Y(NT)\}$ by σ_y^2, we have

$$\sigma_y^2 = \frac{1}{4N^2M^2}\sum_{n=0}^{N-1}\sum_{m=0}^{M-1}\left[V\{X(nT+m\Delta t)\} + V\{X((n+\tfrac{1}{2})T+m\Delta t)\}\right]$$

$$= \frac{1}{4N^2M^2}\left[2NM\sigma_x^2\right] = \frac{\sigma_x^2}{2NM},$$

where we have used the relation

$$V\left\{\sum_{i=1}^{L} a_i X_i\right\} = \sum_{i=1}^{L} a_i^2 V\{X_i\},$$

since the noise samples are assumed uncorrelated.

If the input noise is band-limited at the Nyquist frequency, $\omega_N = 2\pi/2\Delta t = \pi M/S$, and has a constant power spectral density $S_{xx}(\omega) = P_o$, then the input variance is given by (Papoulis, 1977):

$$\sigma_x^2 = R_{xx}(0) = \frac{1}{2\pi}\int_{-\omega_N}^{\omega_N} P_o\, d\omega = \frac{P_o}{\pi}\omega_N = \frac{P_o M}{S},$$

where $R_{xx}(\tau)$ is the autocorrelation at lag τ. Hence the output variance is

$$\sigma_y^2 = \frac{P_o}{2NS}.$$

Thus for white noise input, the output standard error is reduced by the square root of the total integration time as in frequency domain processing, and it is independent of the sampling rate.

For the special case s = T/2 (square wave correlation) the output variance is the same as the frequency domain output variance.

In the continuous limit the output variance increases as S decreases because the input noise is no longer band-limited by the Nyquist frequency (the autocorrelation function becomes a Dirac delta function). Digital processing implies a lower limit on S equal to the sampling interval.

FIGURE CAPTIONS

Fig. 1 Field configuration of LFEM source and receiver and block diagram of data acquisition system showing simulated components.

Fig. 2 Amplitude spectral density of geomagnetic noise and matching amplitude spectral density of synthetic noise.

Fig. 3 Frequency response of the sin/cos correlation used in frequency domain processing with correlation frequency f_0 after 4 and 16 cycles of data have been stacked.

Fig. 4 The digital high-pass filter transfer function for data collected at a base frequency f_0.

Fig. 5 Frequency domain output noise at 0.1 Hz for colored synthetic input noise at various numbers of cycles stacked. The filtered data demonstrates noise reduction after digital high-pass filtering.

Fig. 6 Frequency domain output noise at .03 Hz and 0.3 Hz for colored syntnetic input noise at various numbers of cycles stacked. Tne filtered data demonstrates noise reduction after digital high-pass filtering.

Fig. 7 Frequency response of time domain processing at a base frequency $f_0=1/T$ after 4 cycles of data have been stacked for integration windows $S = .16T$ and $.04T$.

Fig. 8 Time domain output noise at base frequencies 0.1 Hz and 0.3 Hz for colored synthetic input noise at various numbers of cycles stacked. The filtered data demonstrates noise reduction after digital high-pass filtering.

Fig. 9 A simulation of the running average real (a) and imaginary (b) components of frequency domain LFEM data acquisition at 0.3 Hz in the presence of natural field noise. The filtered data convergence has improved considerably at this frequency.

Fig. 10 The corresponding running average amplitude (a) and phase (b) for the data used in Figure 9.

Fig. 11 A simulation of the running average real (a) and imaginary (b) components of frequency domain LFEM data acquisition at 0.1 Hz in the presence of natural field noise. The filtered data convergence has improved at this frequency.

Fig. 12 The corresponding running average amplitude (a) and phase (b) for the data used in Figure 11.

Fig. 13 A simulation of the running average real (a) and imaginary (b) components of frequency domain LFEM data acquisition at 0.1 Hz in the presence of natural field noise. The character of the output is dominated by large noise drift during the first cycle.

Fig. 14 The corresponding running average amplitude (a) and phase (b) for the data used in Figure 13.

Fig. 15 A simulation of the running average real (a) and imaginary (b) components of frequency domain LFEM data acquisition at .03 Hz in the presence of natural field noise. The filtered data convergence has not significantly improved.

Fig. 16 The corresponding running average amplitude (a) and phase (b) for the data used in Figure 15.

Fig. 17 A simulation of the running average real (a) and imaginary (b) components of frequency domain LFEM data acquisition at .01 Hz in the presence of natural field noise. The high-pass filter is ineffective at this frequency.

Fig. 18 The corresponding running average amplitude (a) and phase (b) for the data used in Figure 17.

Fig. 19 Time domain LFEM decay response for a source-receiver separation of 5 km over .01 Sm^{-1} half space. The signal distorted by the anti-alias filter is sampled and digitally integrated over the three data channels shown.

Fig. 20 A simulation of the running average output for the three channels (a, b, and c) of time domain data acquisition at a base frequency of 0.3 Hz in the presence of natural field noise. The filtered data convergence has dramatically improved.

Fig. 21 A simulation of the running average output for the three channels (a, b, and c) of time domain data acquisition at a base frequency of 0.1 Hz in the presence of natural field noise. The filtered data convergence has improved.

Fig. 22 A simulation of the running average output for the three channels (a, b, and c) of time domain data acquisition at a base frequency of .03 Hz in the presence of natural field noise. The filtered data convergence has not significantly improved.

Fig. 23 A repeat of the channel 3 simulation at 0.1 Hz (Figure 21) with the integration window quadrupled by extending it to the end of the off time decay response. No improvement in signal/noise results and even the details of the convergence pattern are preserved.

Fig. 24 A simulation of the running average real (a) and imaginary (b) components of frequency domain LFEM data acquisition at .03 Hz using remote reference natural field noise removal.

Fig. 25 A simulation of the running average real (a) and imaginary (b) components of frequency domain LFEM data acquisition at .01 Hz using-remote reference natural field noise removal. Residual error is sensitive to instrument resolution indicated by increasing the remote reference data word from 8 bits to 12 bits.

Fig. 26 A simulation of the running average output for channel 3 of time domain LFEM data acquisition using remote reference noise removal at a base frequency of 0.1 Hz. Residual error is sensitive to instrument resolution indicated by increasing the remote reference data word from 8 bits to 12 bits.

Fig. 27 A simulation of the running average output for channel 2 of time domain LFEM data acquisition using remote reference noise removal at a base frequency of .03 Hz. Residual error is sensitive to instrument resolution indicated by increasing the remote reference data word from 8 bits to 12 bits.

Fig. A.1 Time domain system impulse response for time domain LFEM data acquisition. The base frequency is 1/T, data is stacked with alternating polarity N times each, with each stacked sample integrated over the time window S.

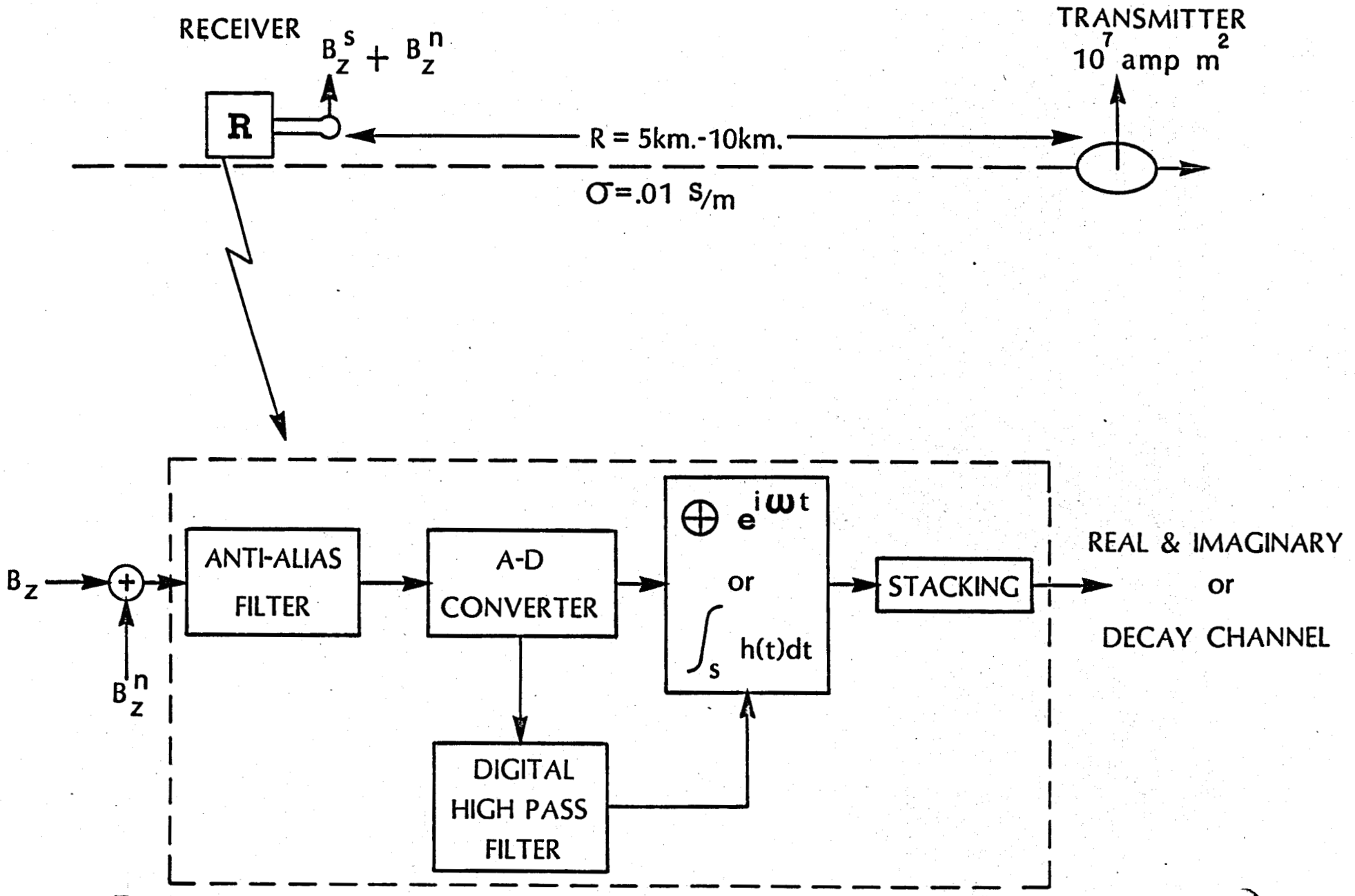
RECEIVER
$B_z^s + B_z^n$
R
TRANSMITTER
10^7 amp m^2
R = 5km.-10km.
σ=.01 s/m
B_z
B_z^n
ANTI-ALIAS FILTER
A-D CONVERTER
$\oplus$ $e^{i\omega t}$
or
$\int_s h(t)dt$
STACKING
REAL & IMAGINARY
or
DECAY CHANNEL
DIGITAL HIGH PASS FILTER

FIGURE 1

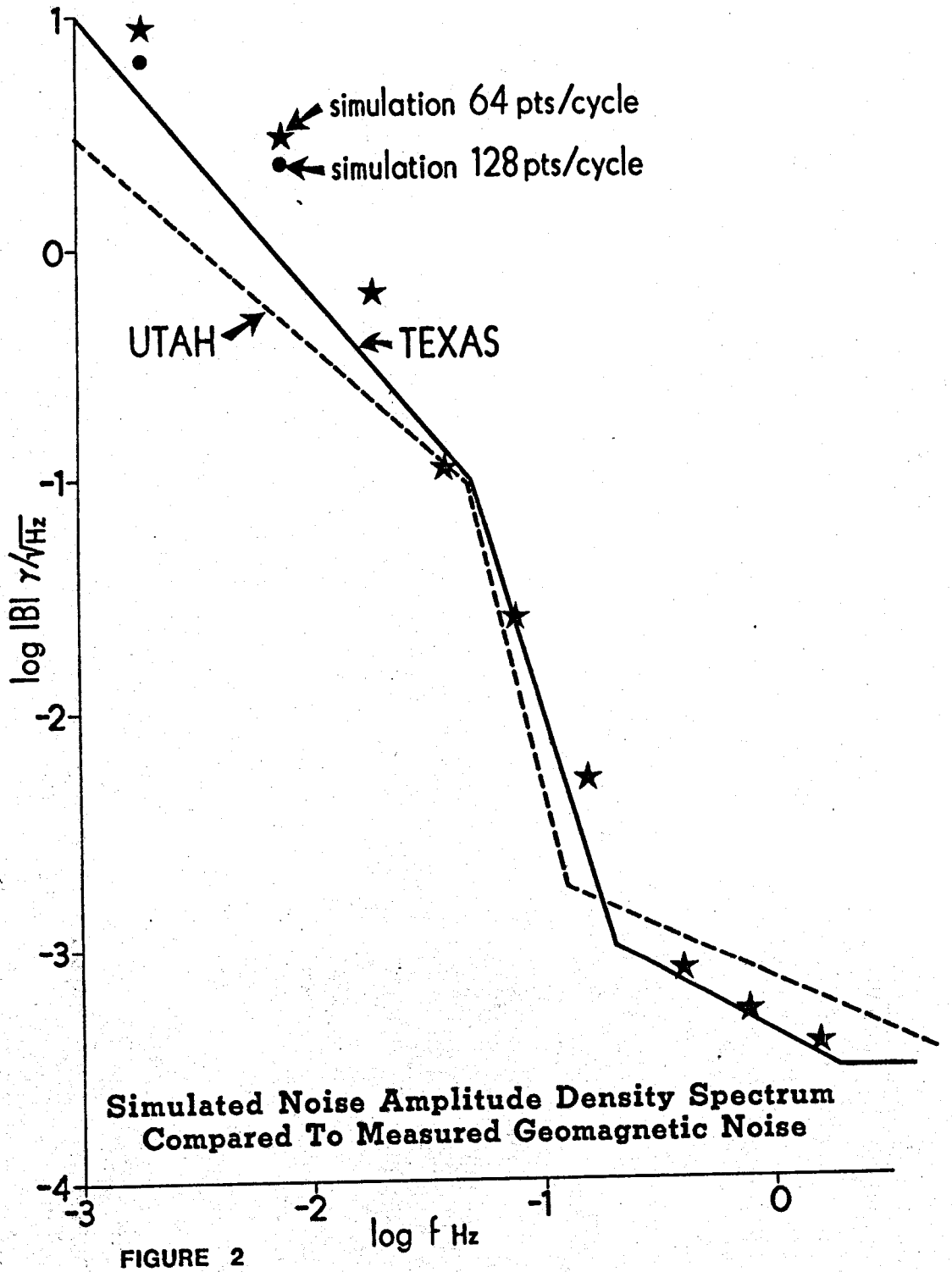

Simulated Noise Amplitude Density Spectrum Compared To Measured Geomagnetic Noise

FIGURE 2

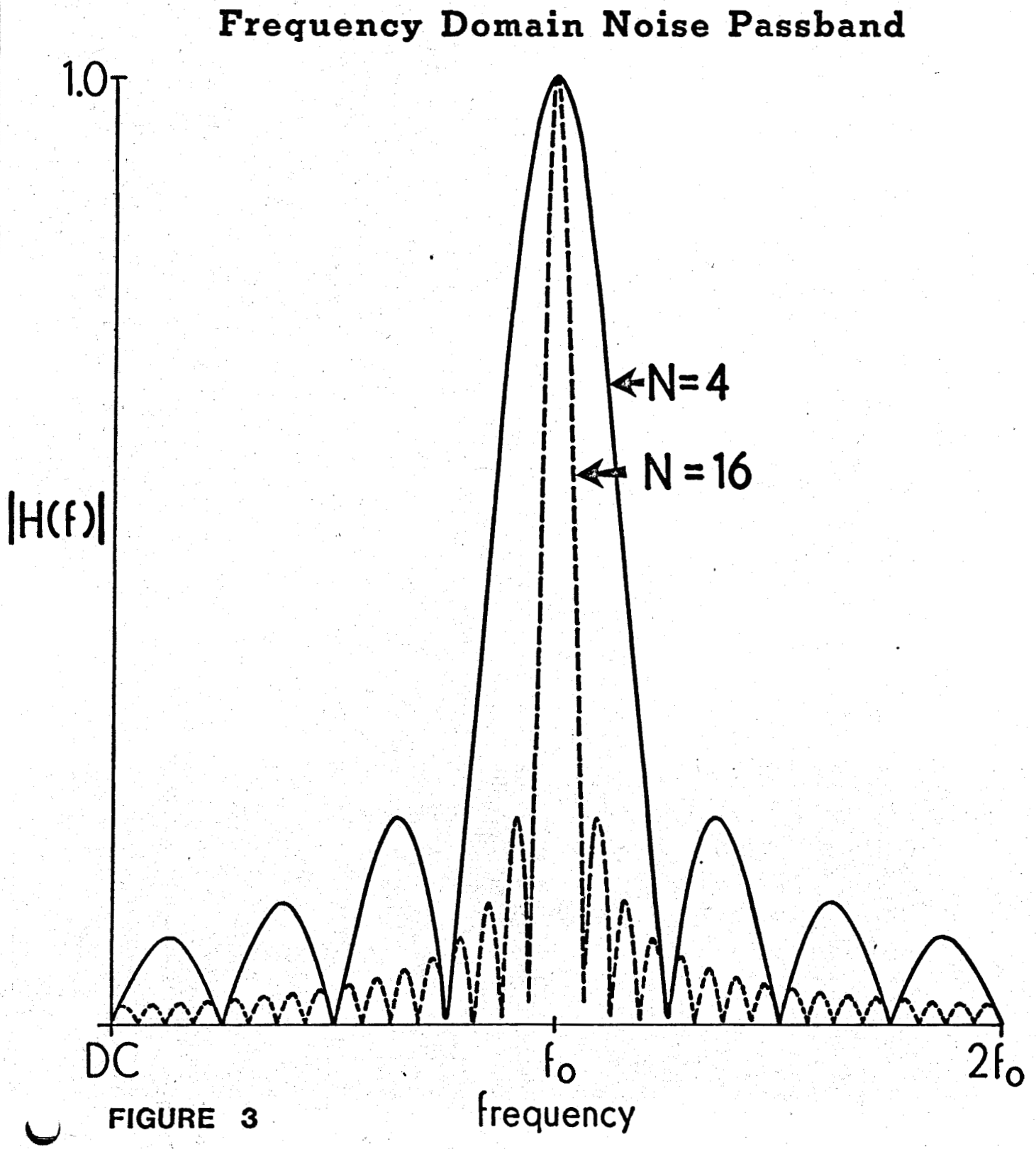
Frequency Domain Noise Passband
1.0
|H(f)|
N=4
N=16
DC
fo
2fo
frequency

FIGURE 3

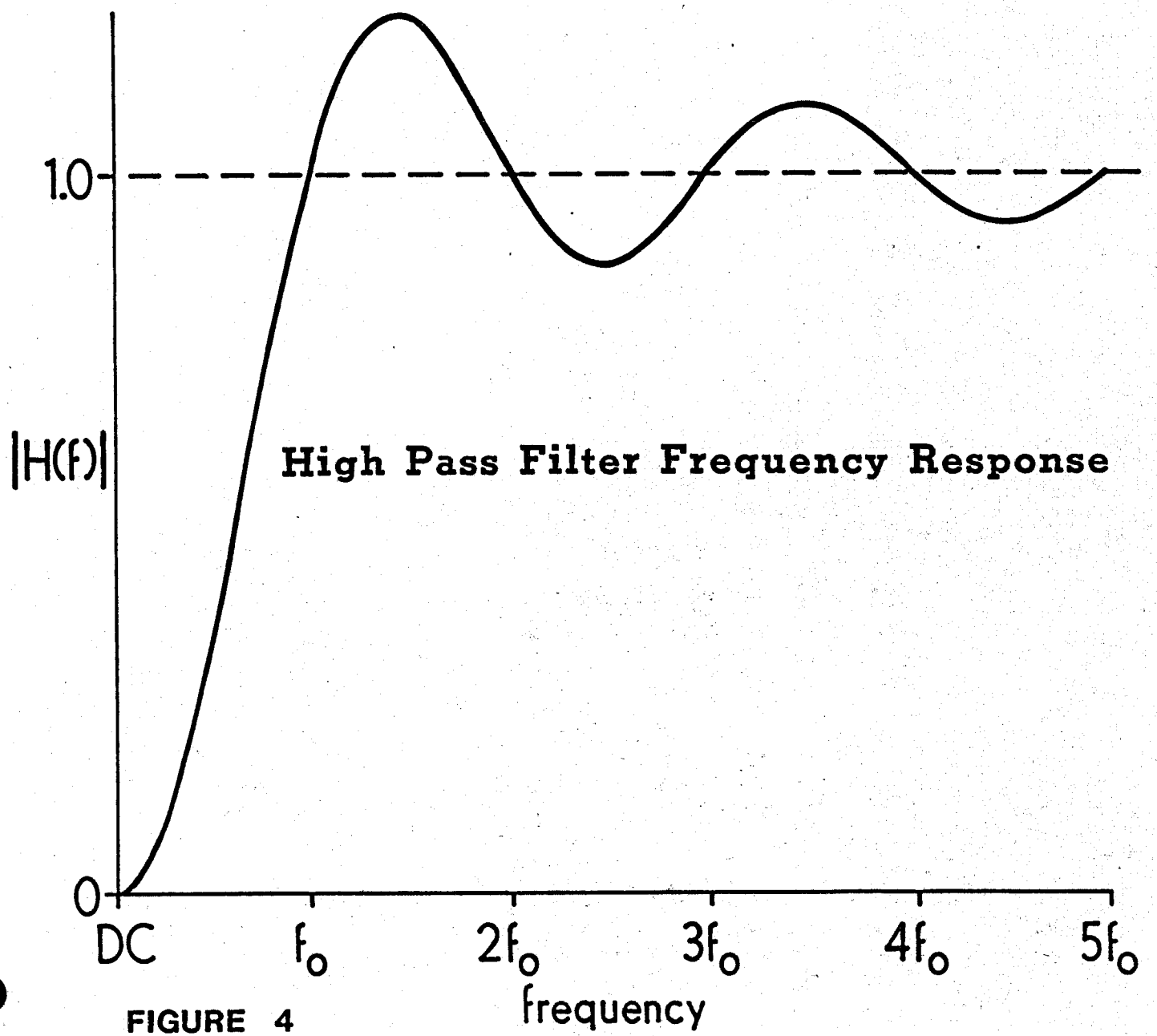

High Pass Filter Frequency Response

FIGURE 4

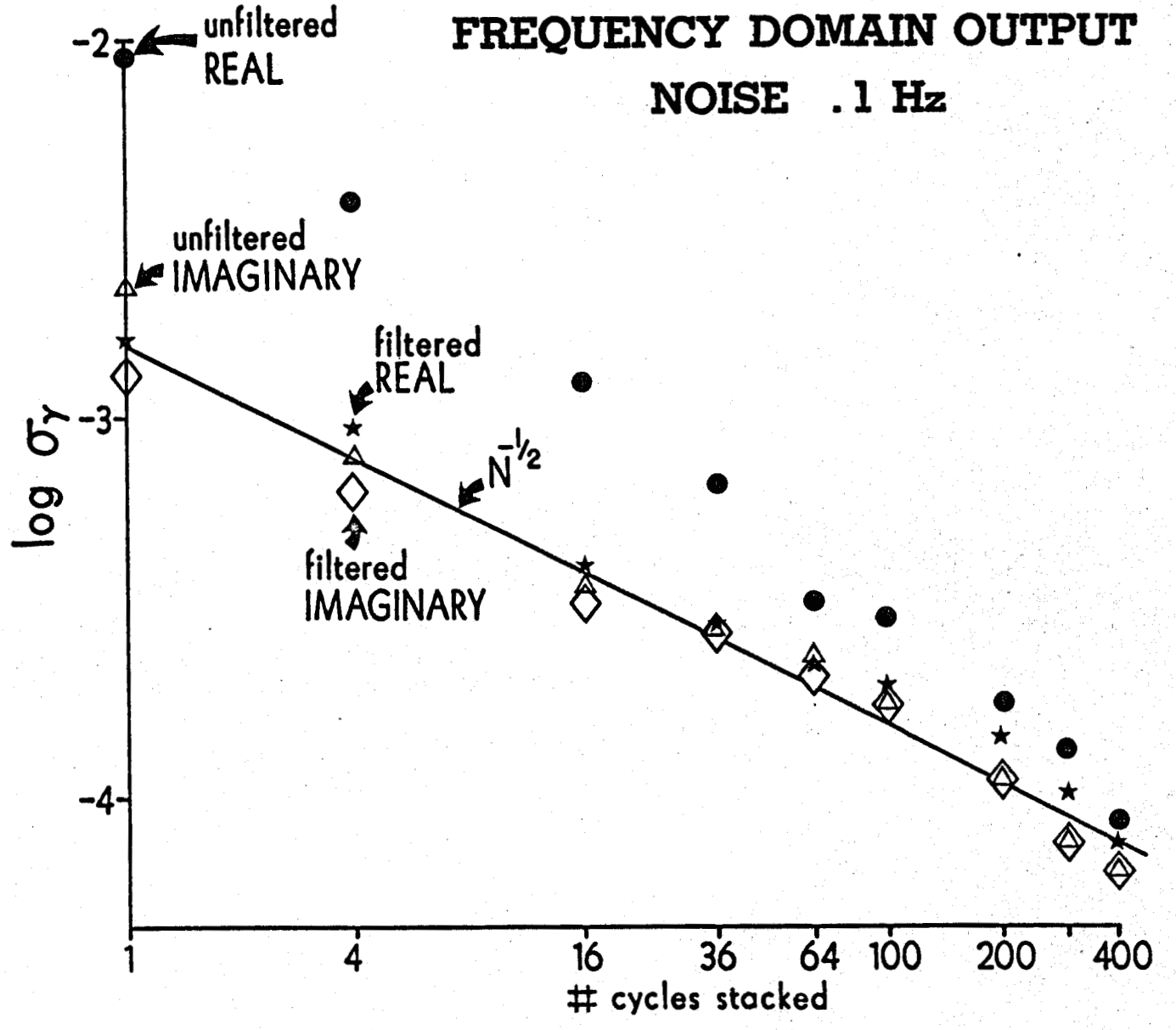
FREQUENCY DOMAIN OUTPUT
NOISE .1 Hz
unfiltered
REAL
unfiltered
IMAGINARY
filtered
REAL
filtered
IMAGINARY
$N^{-1/2}$
log σ_Y
-2
-3
-4
1
4
16
36
64
100
200
400
cycles stacked

FIGURE 5

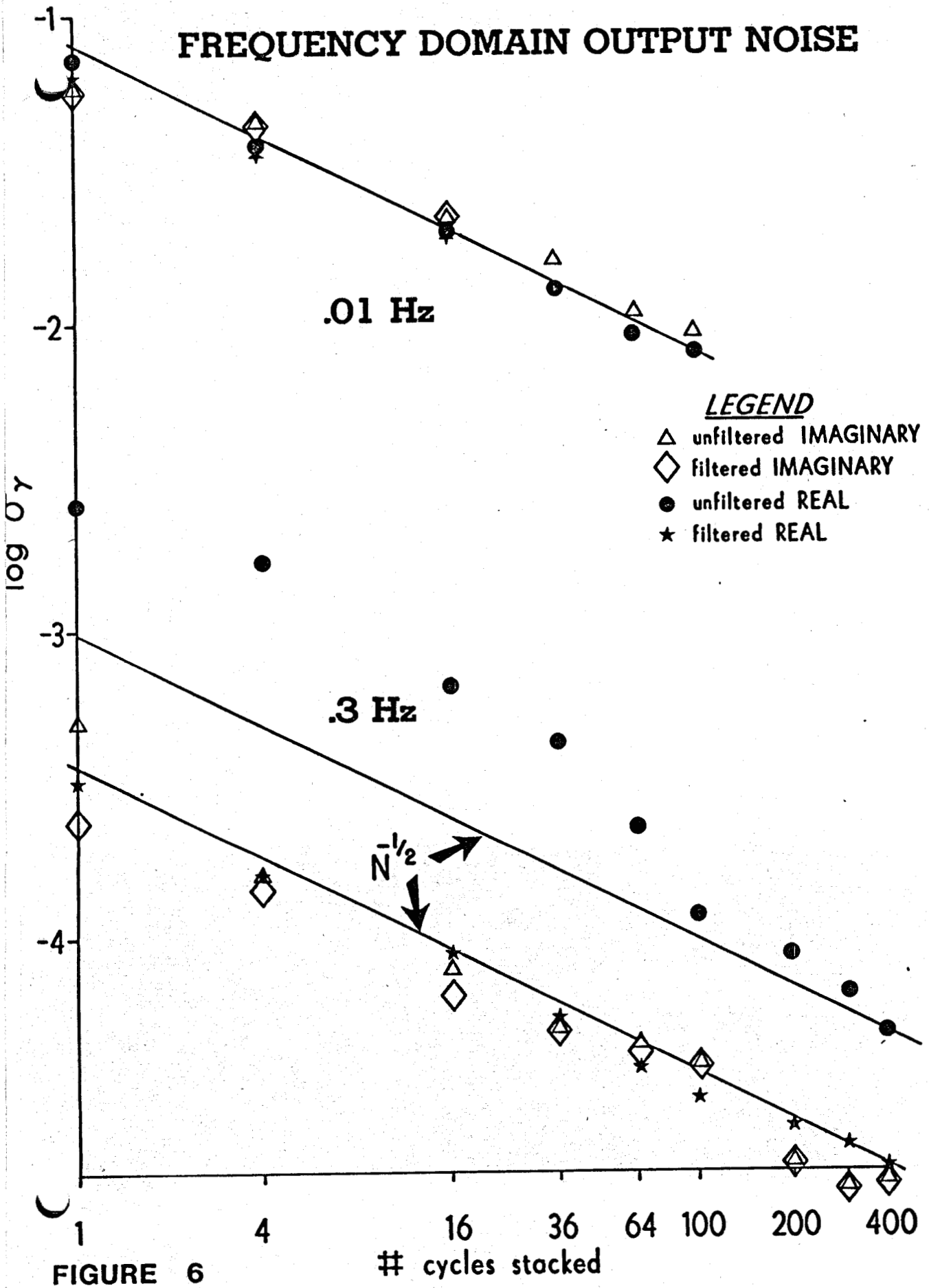
FREQUENCY DOMAIN OUTPUT NOISE
-1
-2
-3
-4
log σγ
.01 Hz
.3 Hz
LEGEND
unfiltered IMAGINARY
filtered IMAGINARY
unfiltered REAL
filtered REAL
N^-1/2
1
4
16
36
64
100
200
400
cycles stacked

FIGURE 6

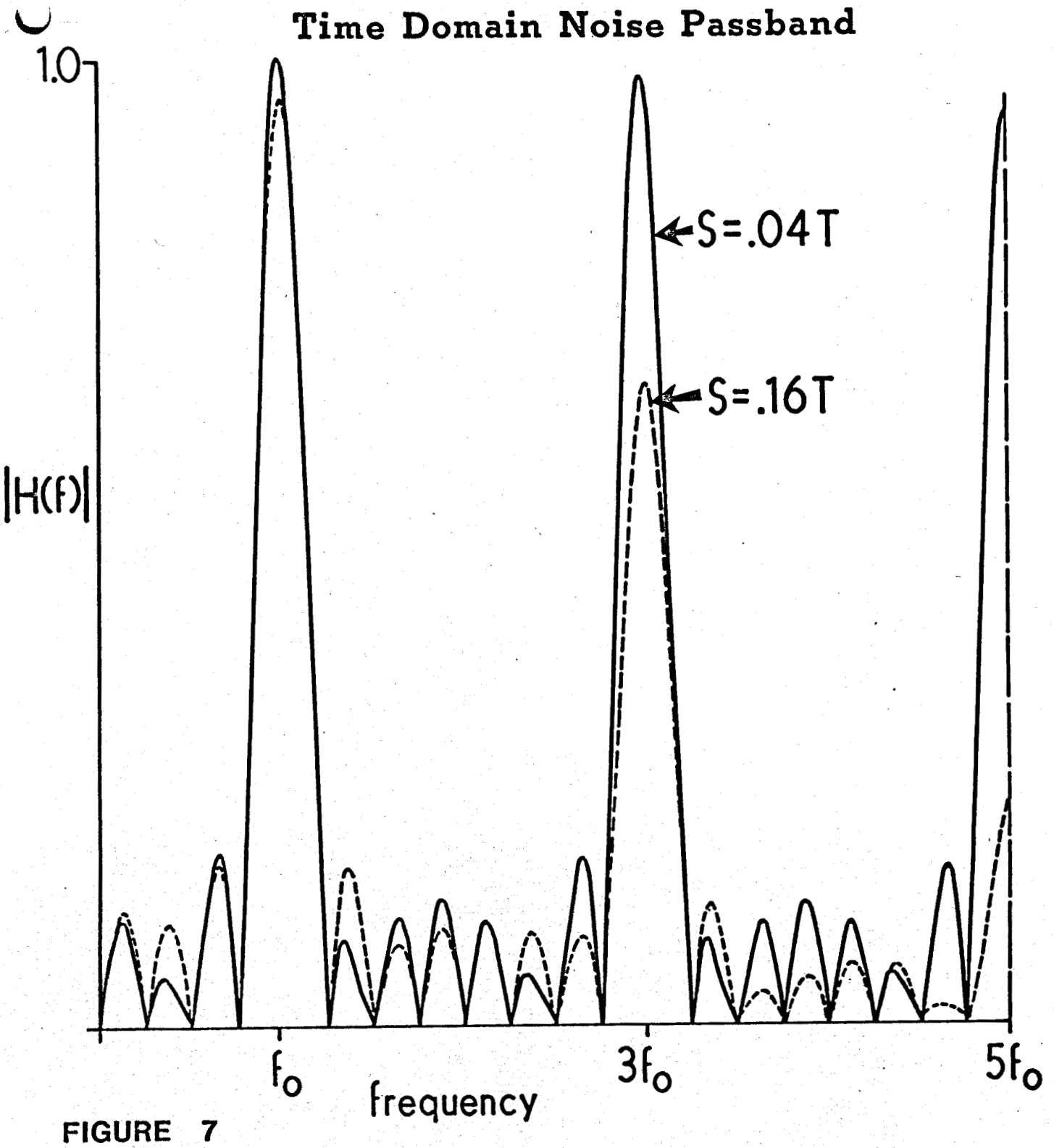
Time Domain Noise Passband
1.0
|H(f)|
S=.04T
S=.16T
f_o
$3f_o$
$5f_o$
frequency

FIGURE 7

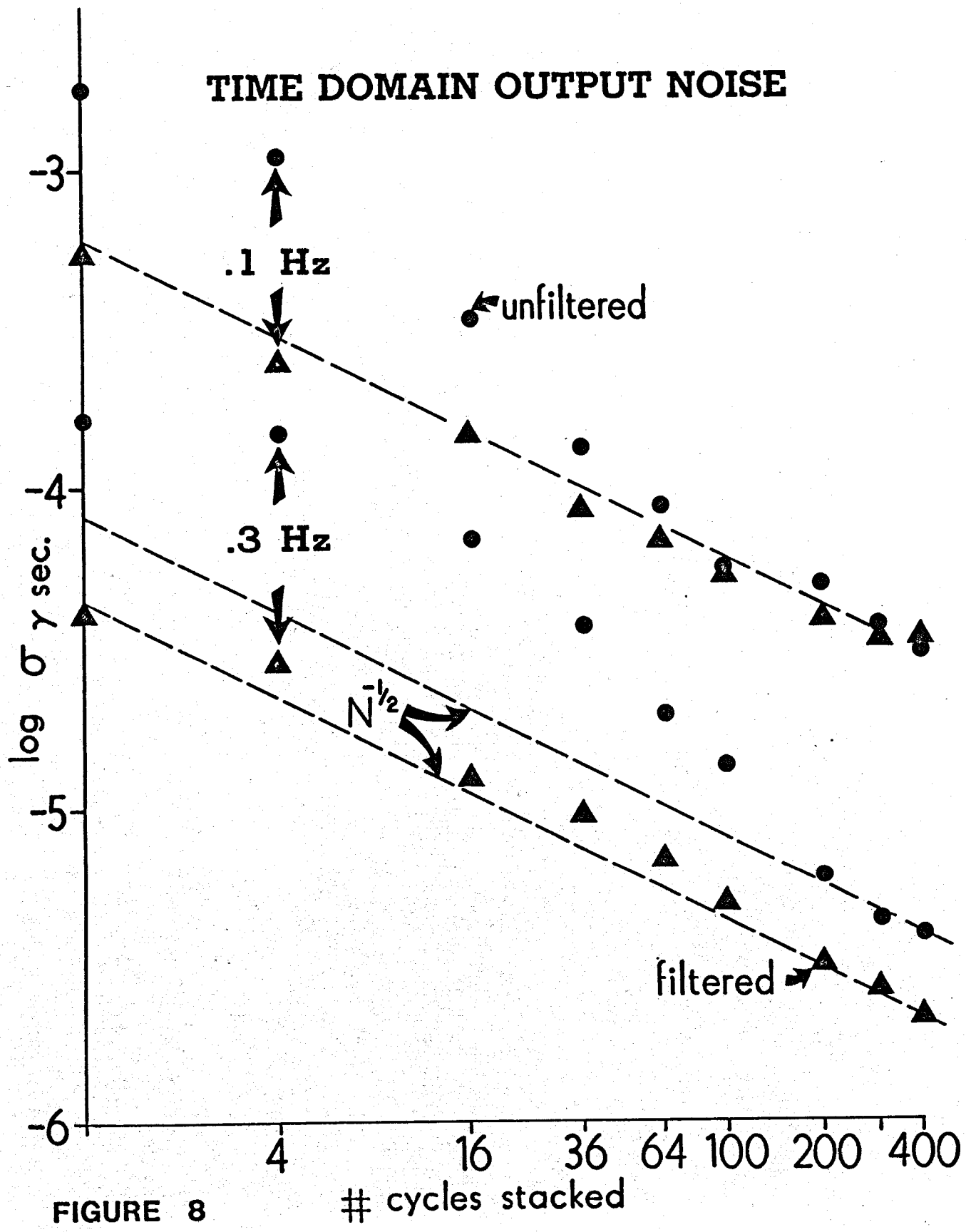
TIME DOMAIN OUTPUT NOISE
-3
-4
-5
-6
.1 Hz
.3 Hz
unfiltered
filtered
$N^{-1/2}$
log σ γ sec.
4
16
36
64
100
200
400
cycles stacked

FIGURE 8

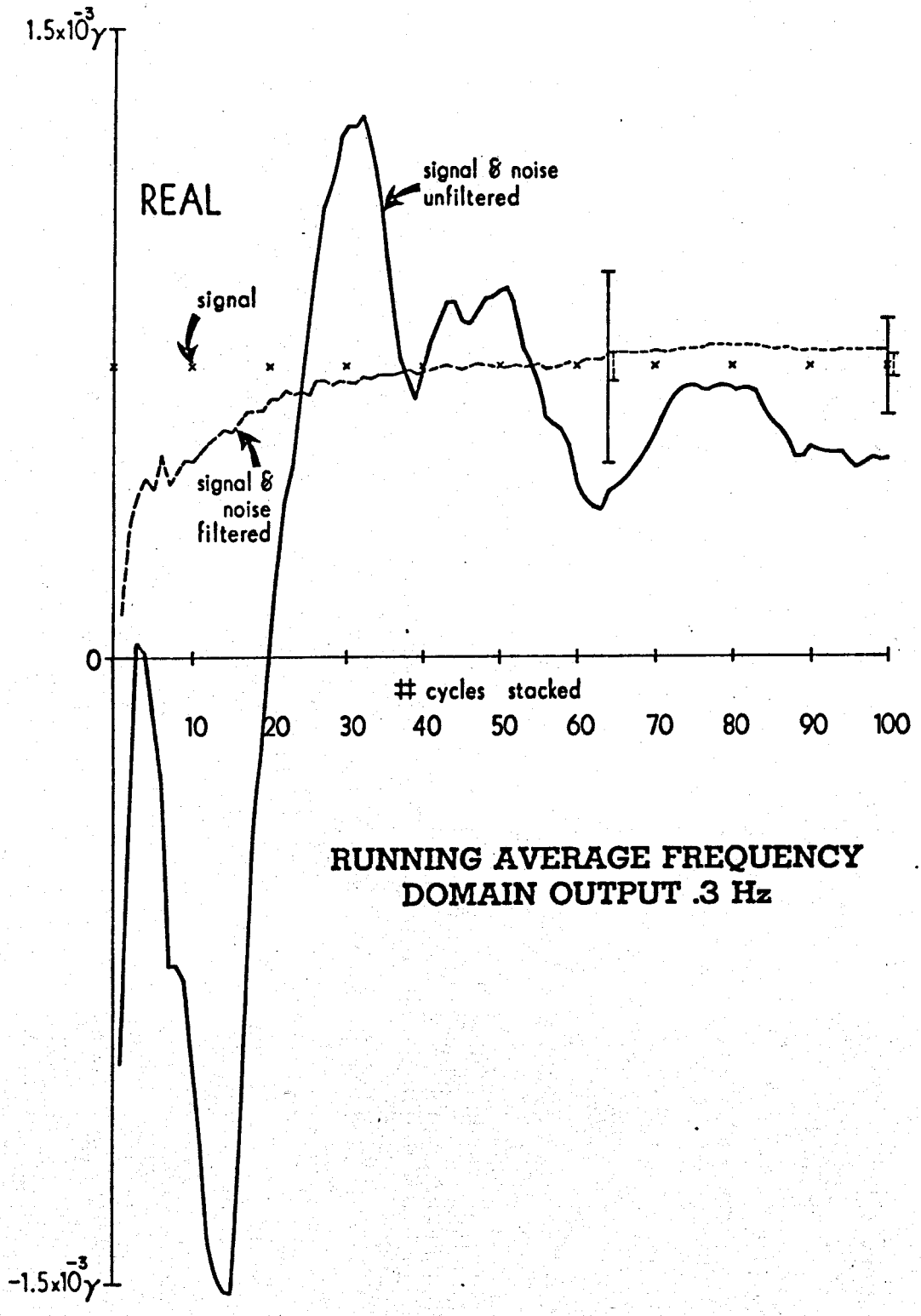

RUNNING AVERAGE FREQUENCY DOMAIN OUTPUT .3 Hz

FIGURE 9a

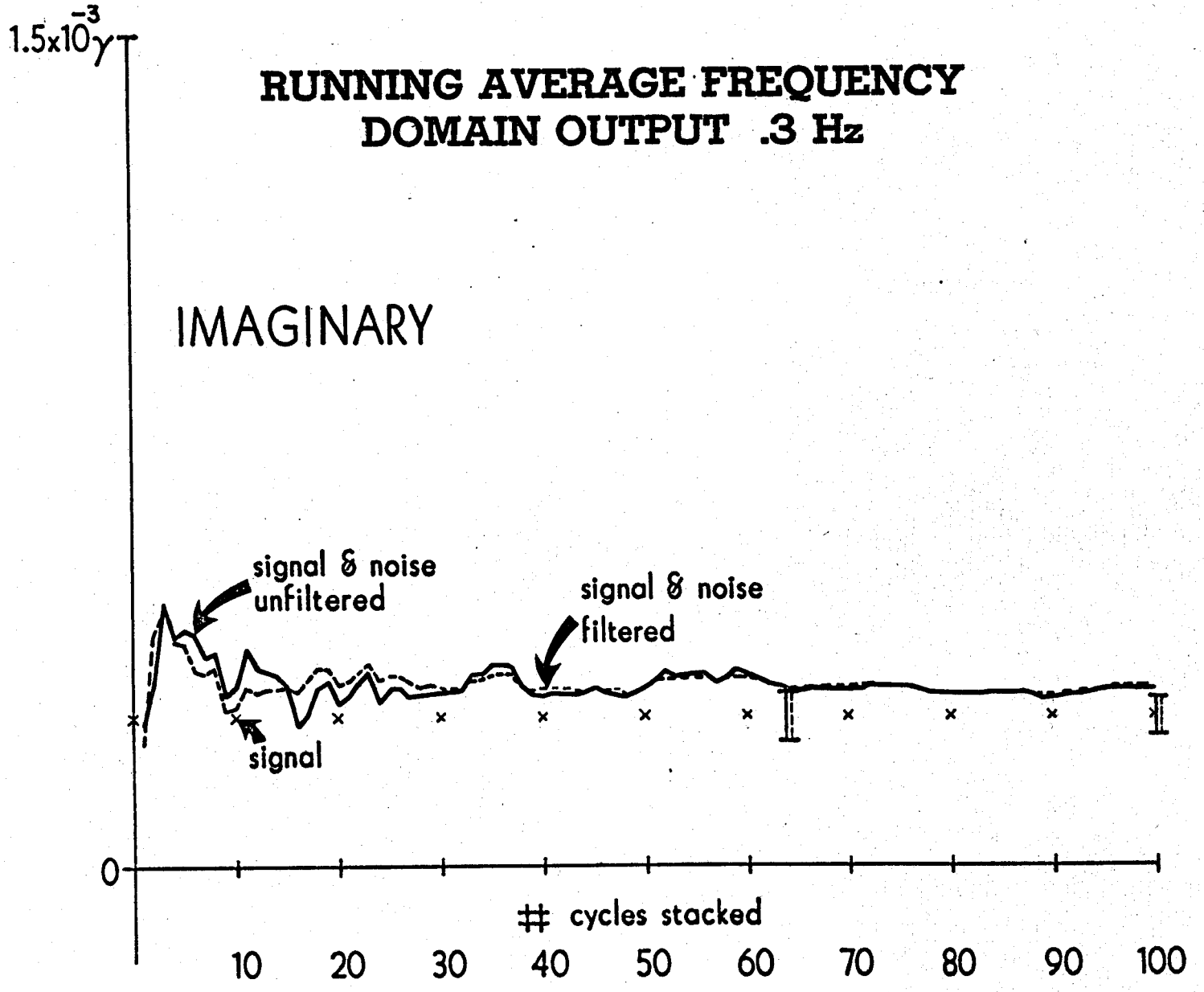
1.5x10⁻³γ
RUNNING AVERAGE FREQUENCY
DOMAIN OUTPUT .3 Hz
IMAGINARY
signal & noise
unfiltered
signal & noise
filtered
signal
0
cycles stacked
10
20
30
40
50
60
70
80
90
100

FIGURE 9b

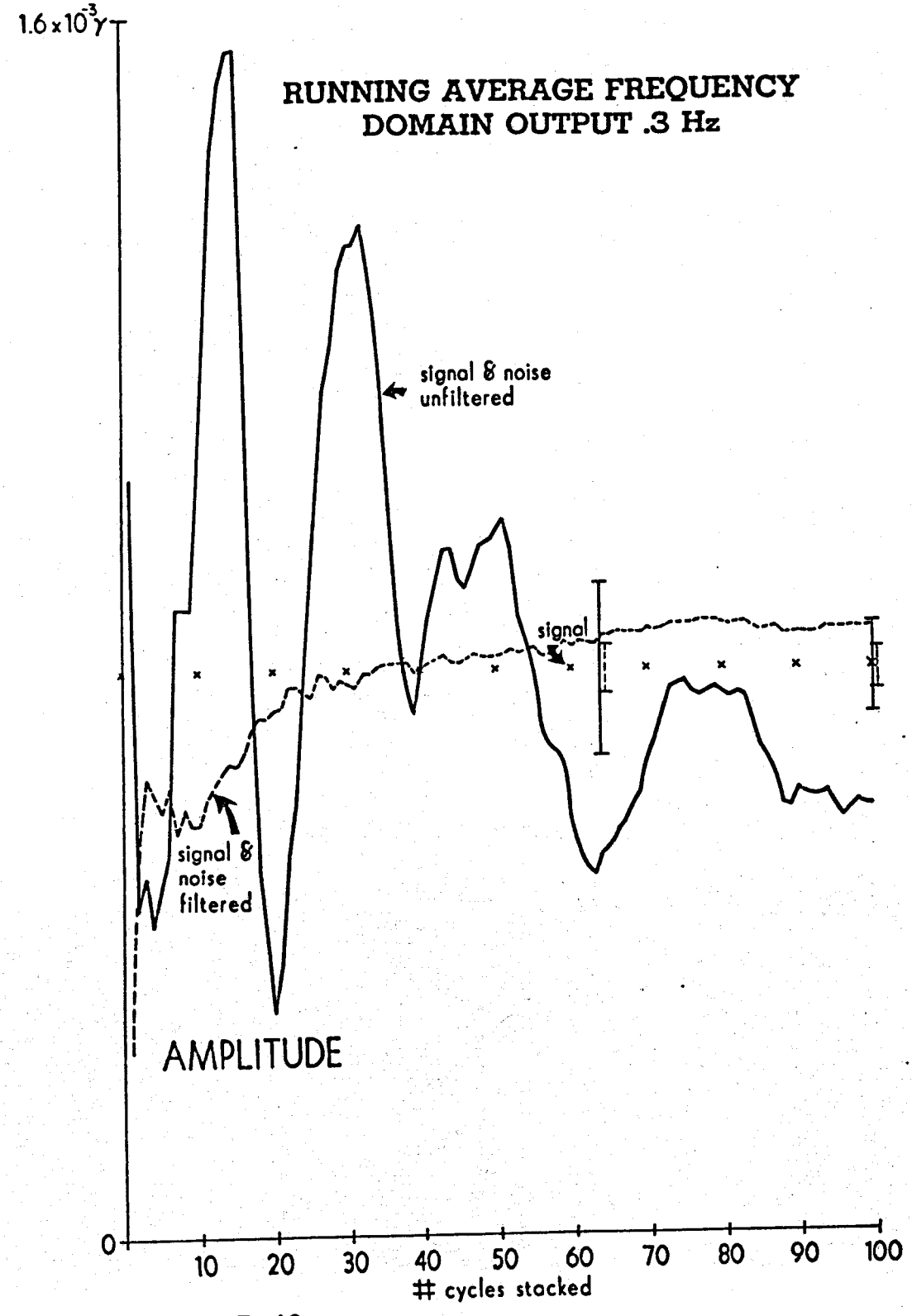
1.6 x 10⁻³ γ
RUNNING AVERAGE FREQUENCY
DOMAIN OUTPUT .3 Hz
signal & noise
unfiltered
signal
signal &
noise
filtered
AMPLITUDE
0
10
20
30
40
50
60
70
80
90
100
cycles stacked

FIGURE 10a

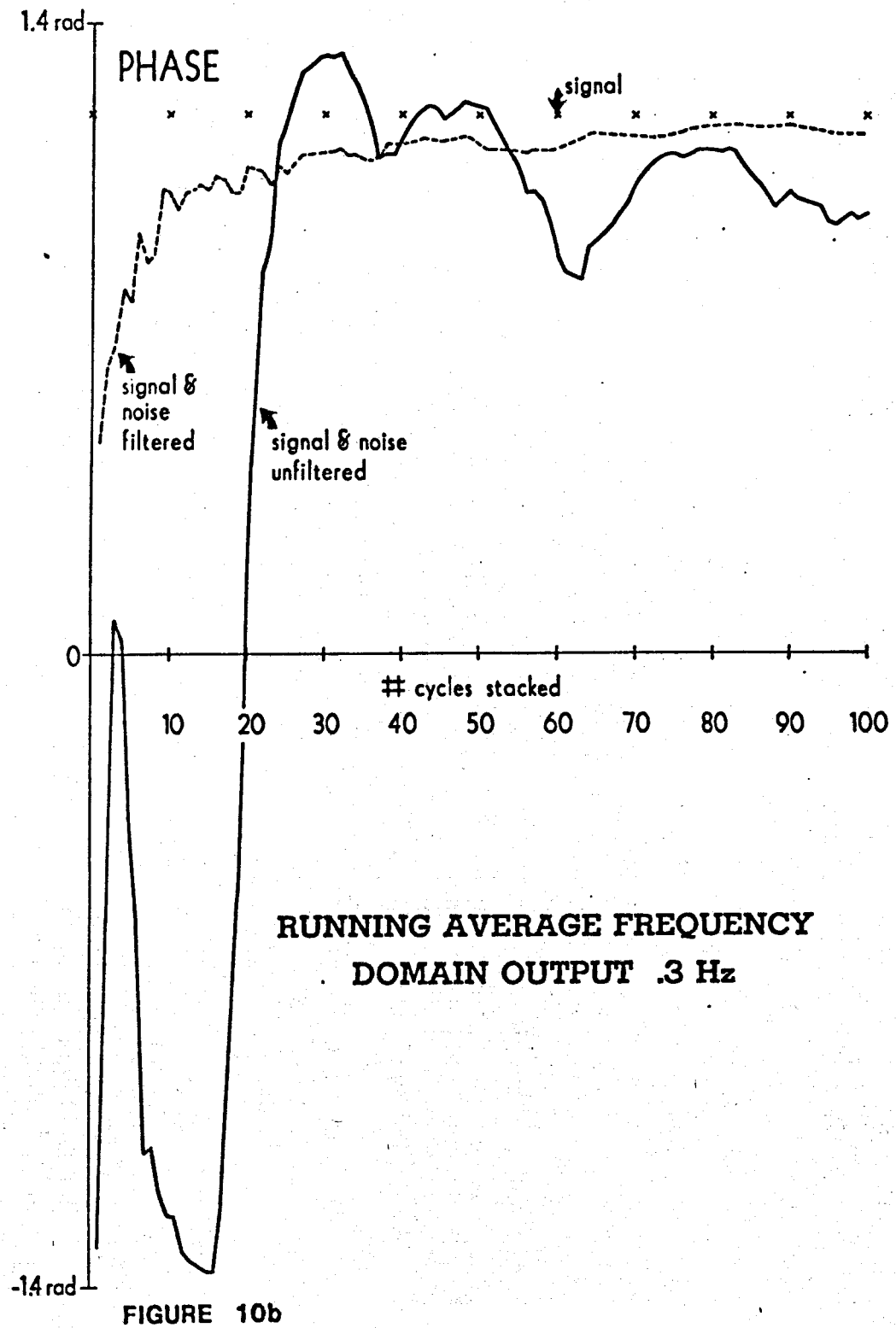

RUNNING AVERAGE FREQUENCY DOMAIN OUTPUT .3 Hz

FIGURE 10b

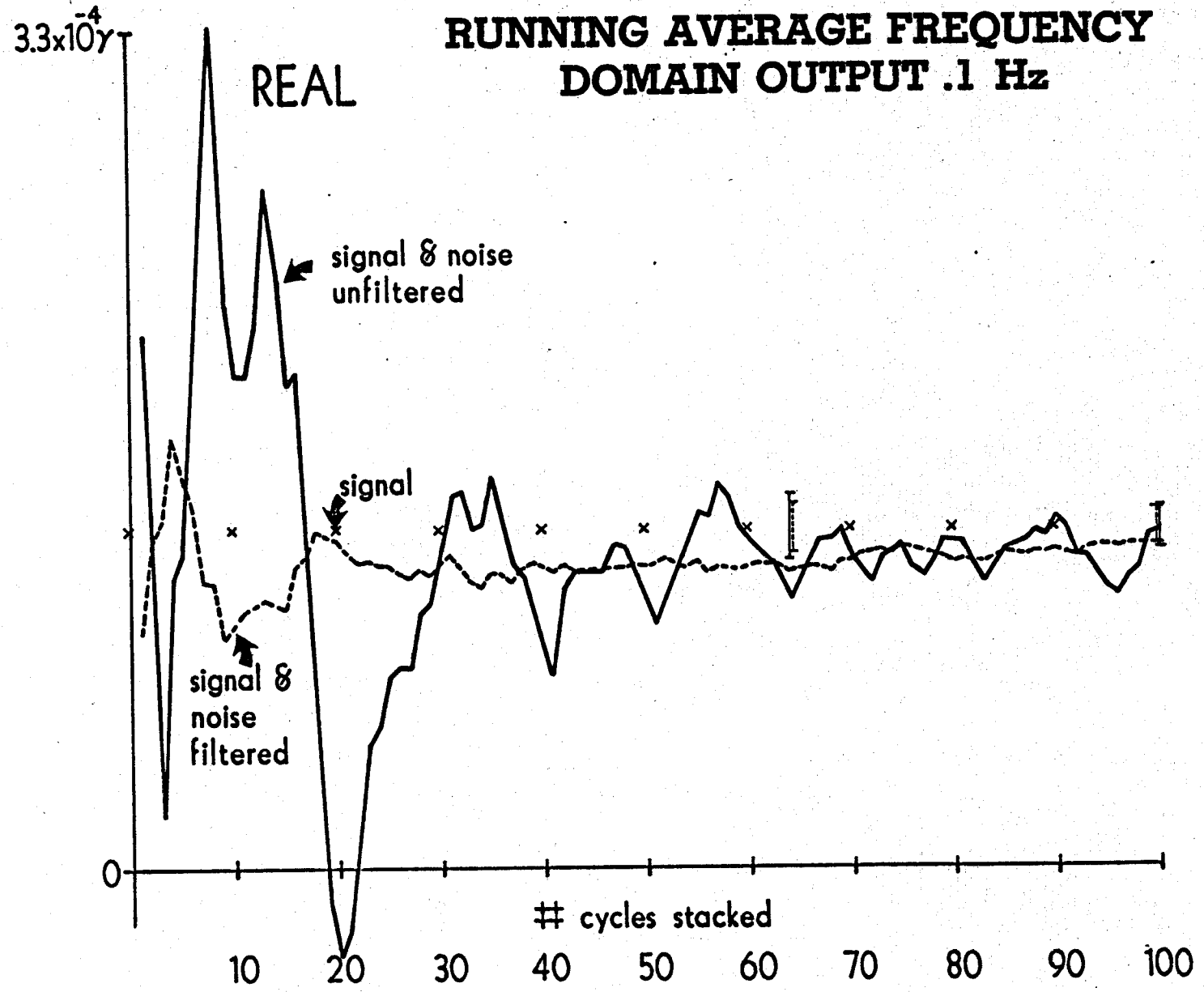
RUNNING AVERAGE FREQUENCY
DOMAIN OUTPUT .1 Hz
3.3x10⁻⁴Y
REAL
signal & noise
unfiltered
signal
signal &
noise
filtered
0
cycles stacked
10
20
30
40
50
60
70
80
90
100

FIGURE 11a

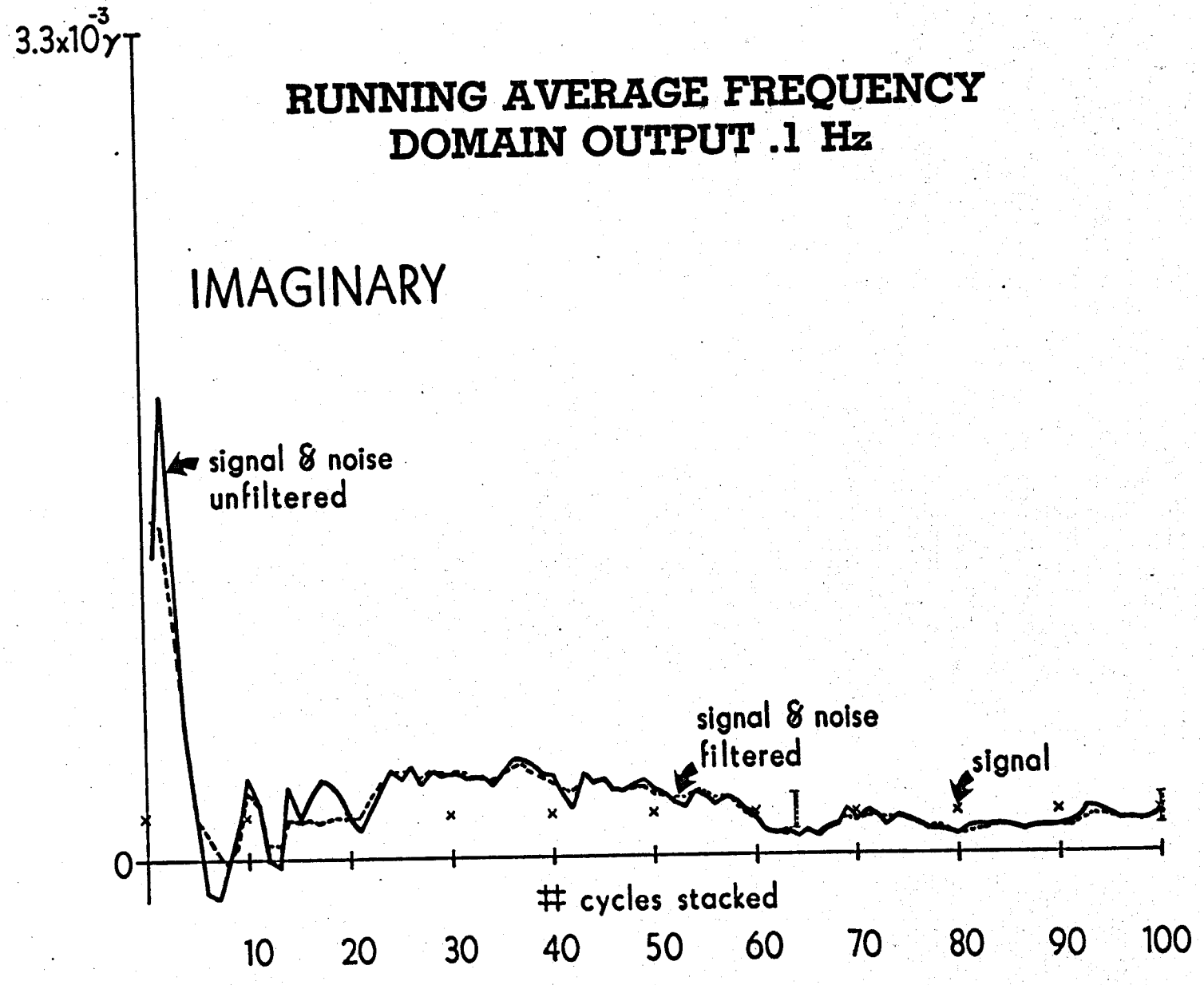
3.3x10⁻³γ
RUNNING AVERAGE FREQUENCY
DOMAIN OUTPUT .1 Hz
IMAGINARY
signal & noise
unfiltered
signal & noise
filtered
signal
0
cycles stacked
10
20
30
40
50
60
70
80
90
100

FIGURE 11b

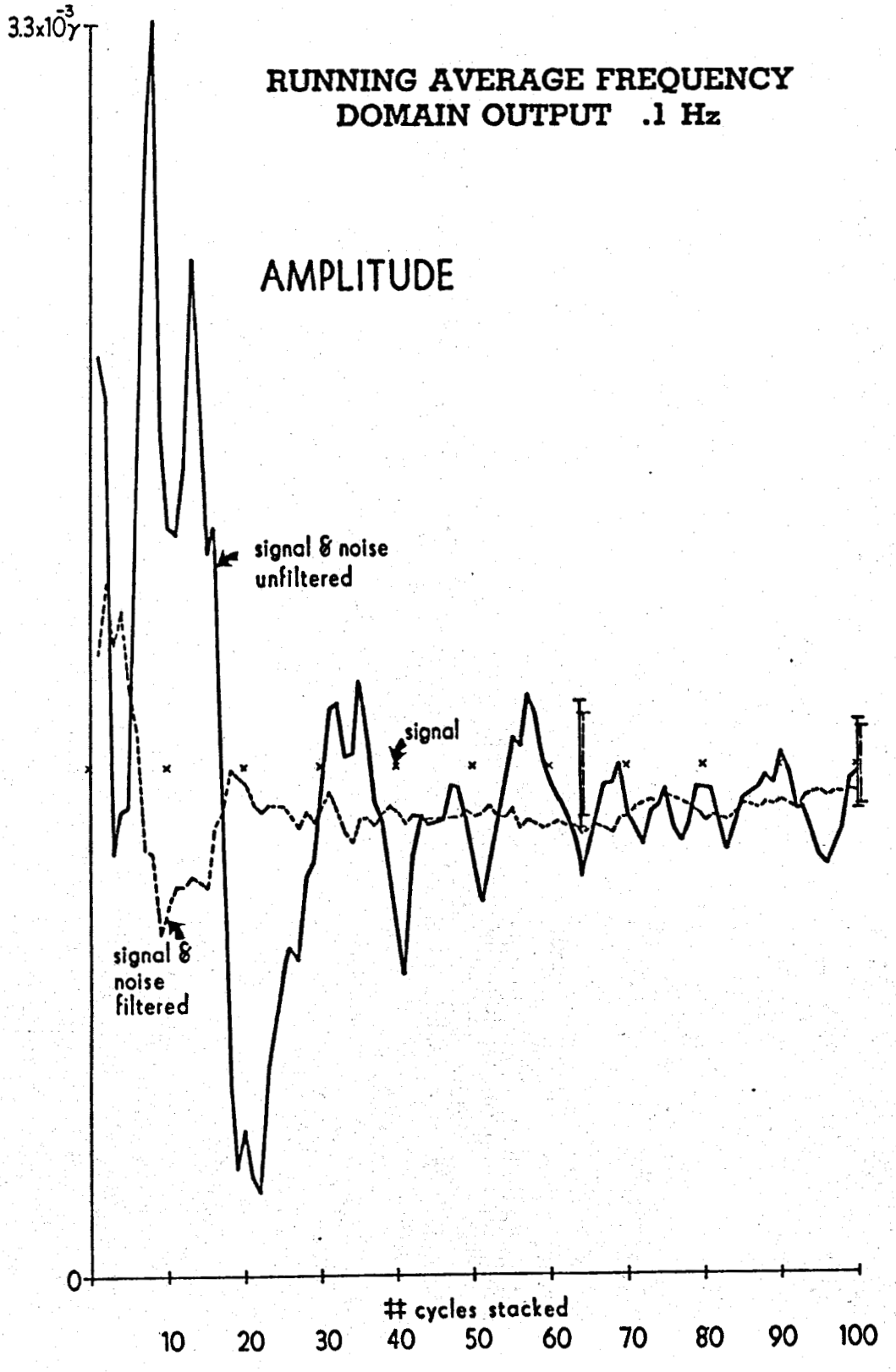
3.3x10⁻³γ
RUNNING AVERAGE FREQUENCY
DOMAIN OUTPUT .1 Hz
AMPLITUDE
signal & noise
unfiltered
signal
signal &
noise
filtered
0
cycles stacked
10
20
30
40
50
60
70
80
90
100

FIGURE 12 a

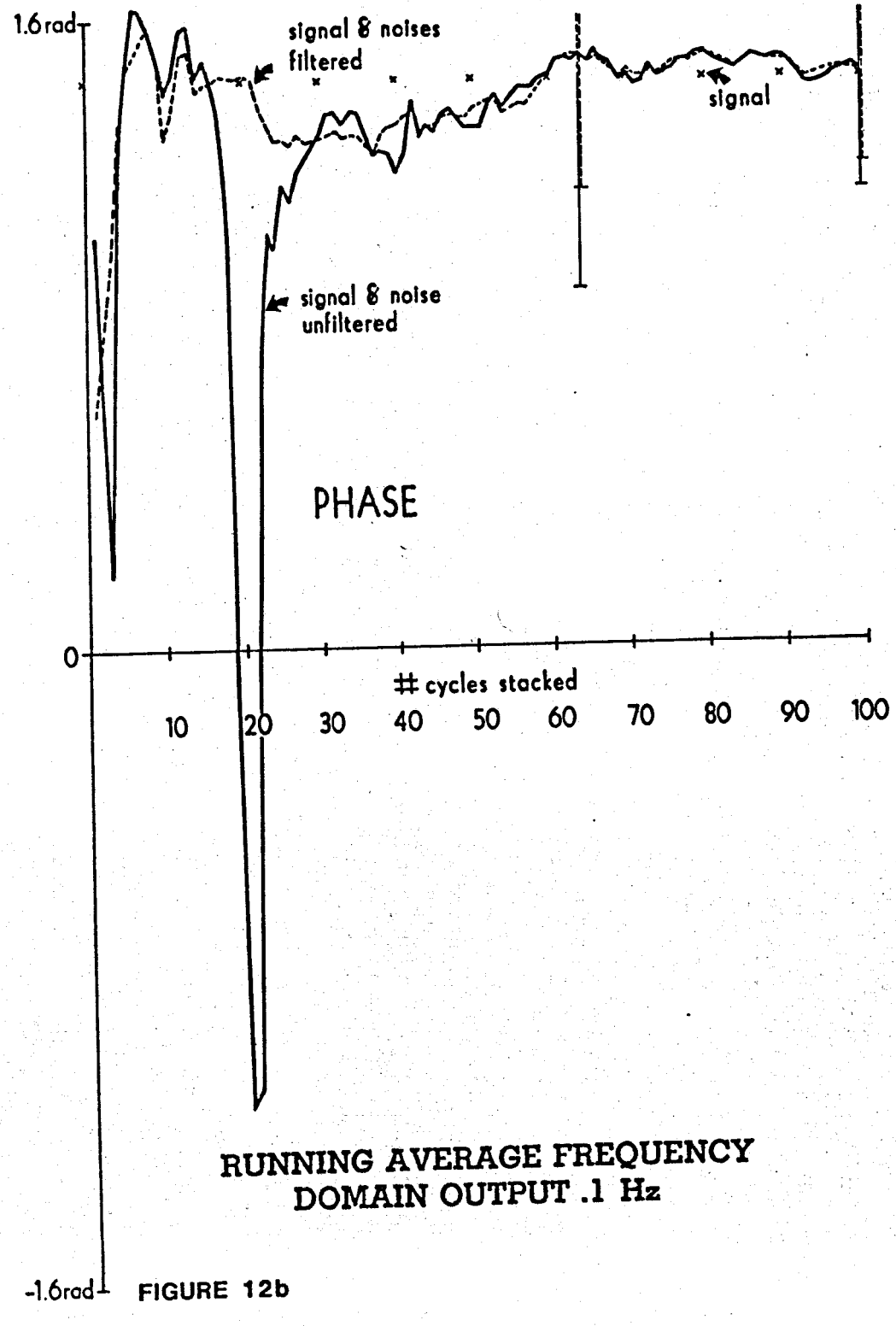

RUNNING AVERAGE FREQUENCY DOMAIN OUTPUT .1 Hz

FIGURE 12b

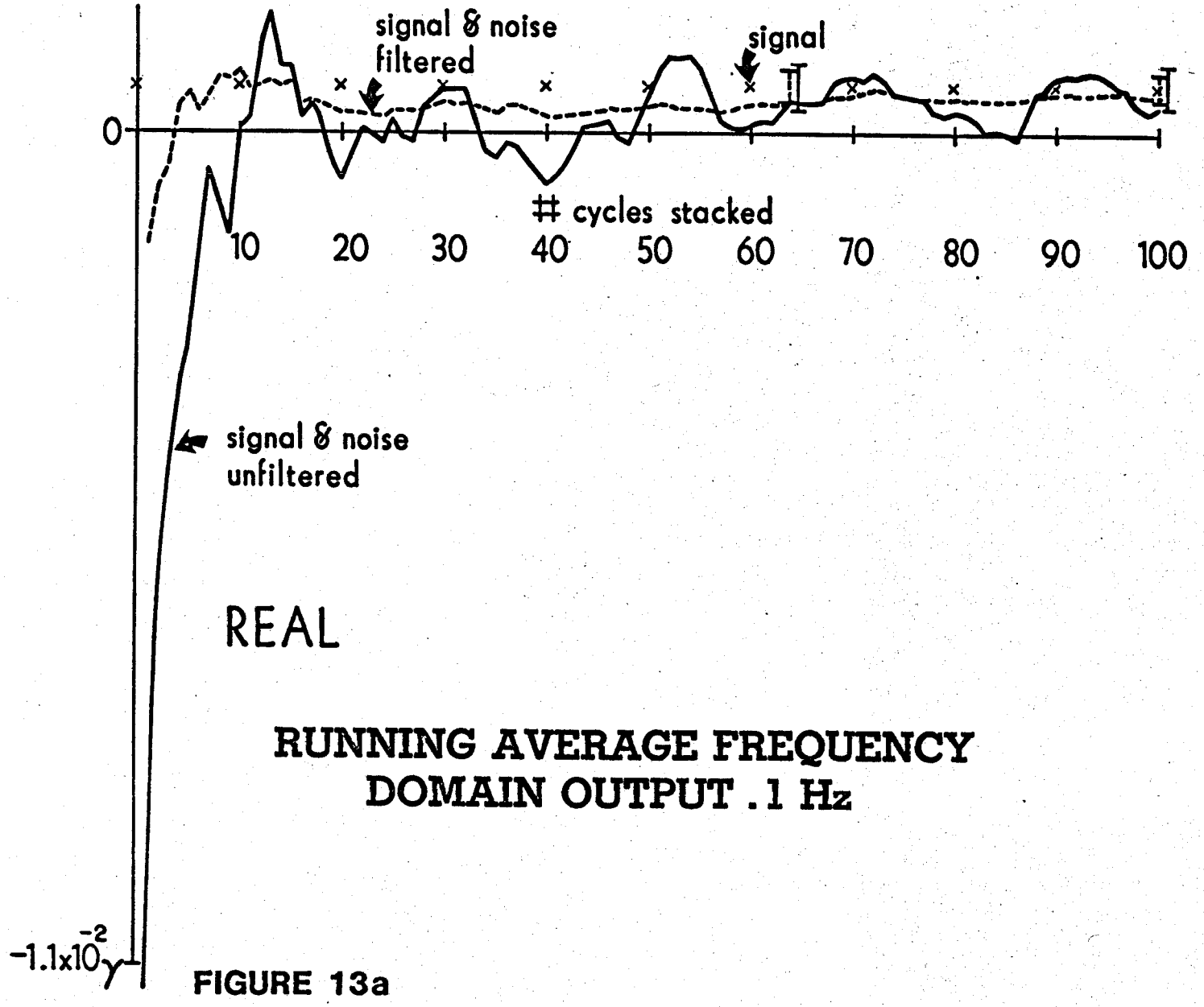
signal & noise
filtered
signal
0
cycles stacked
10
20
30
40
50
60
70
80
90
100
signal & noise
unfiltered
REAL
RUNNING AVERAGE FREQUENCY
DOMAIN OUTPUT .1 Hz
-1.1x10^-2 γ

FIGURE 13a

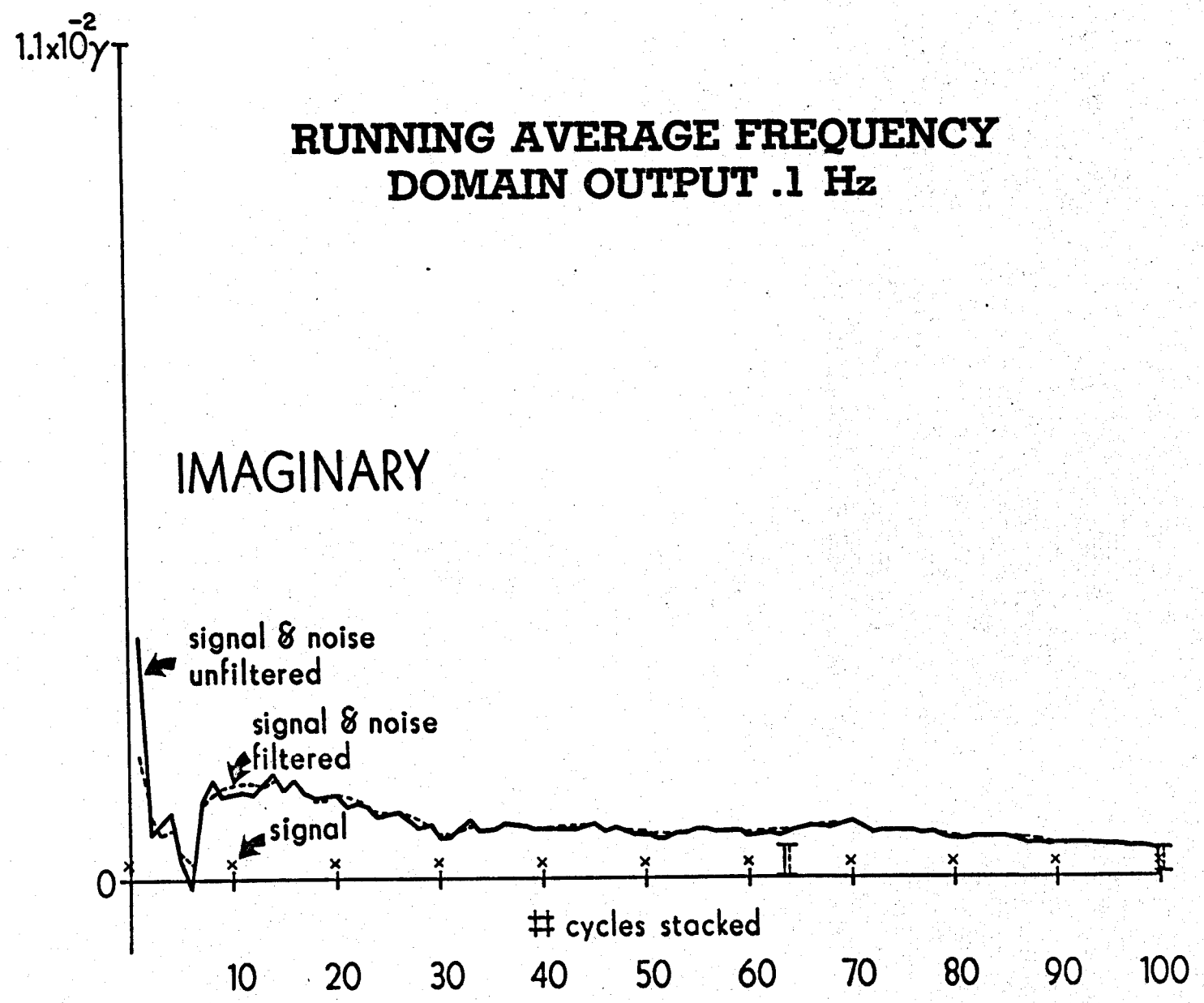
1.1x10^-2 γ
RUNNING AVERAGE FREQUENCY
DOMAIN OUTPUT .1 Hz
IMAGINARY
signal & noise
unfiltered
signal & noise
filtered
signal
0
cycles stacked
10
20
30
40
50
60
70
80
90
100

FIGURE 13b

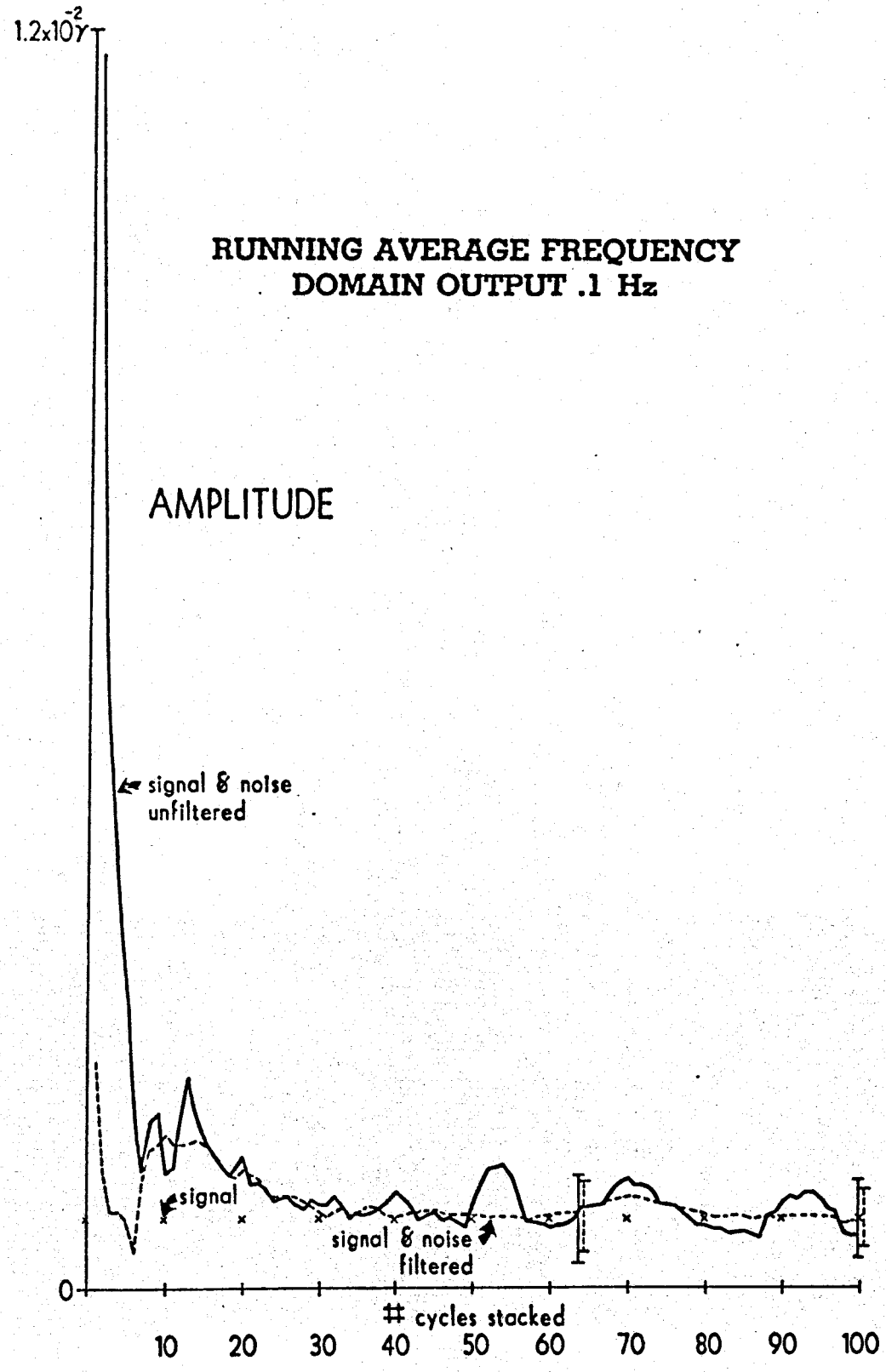
1.2x10⁻²
RUNNING AVERAGE FREQUENCY
DOMAIN OUTPUT .1 Hz
AMPLITUDE
signal & noise
unfiltered
signal
signal & noise
filtered
0
cycles stacked
10
20
30
40
50
60
70
80
90
100

FIGURE 14a

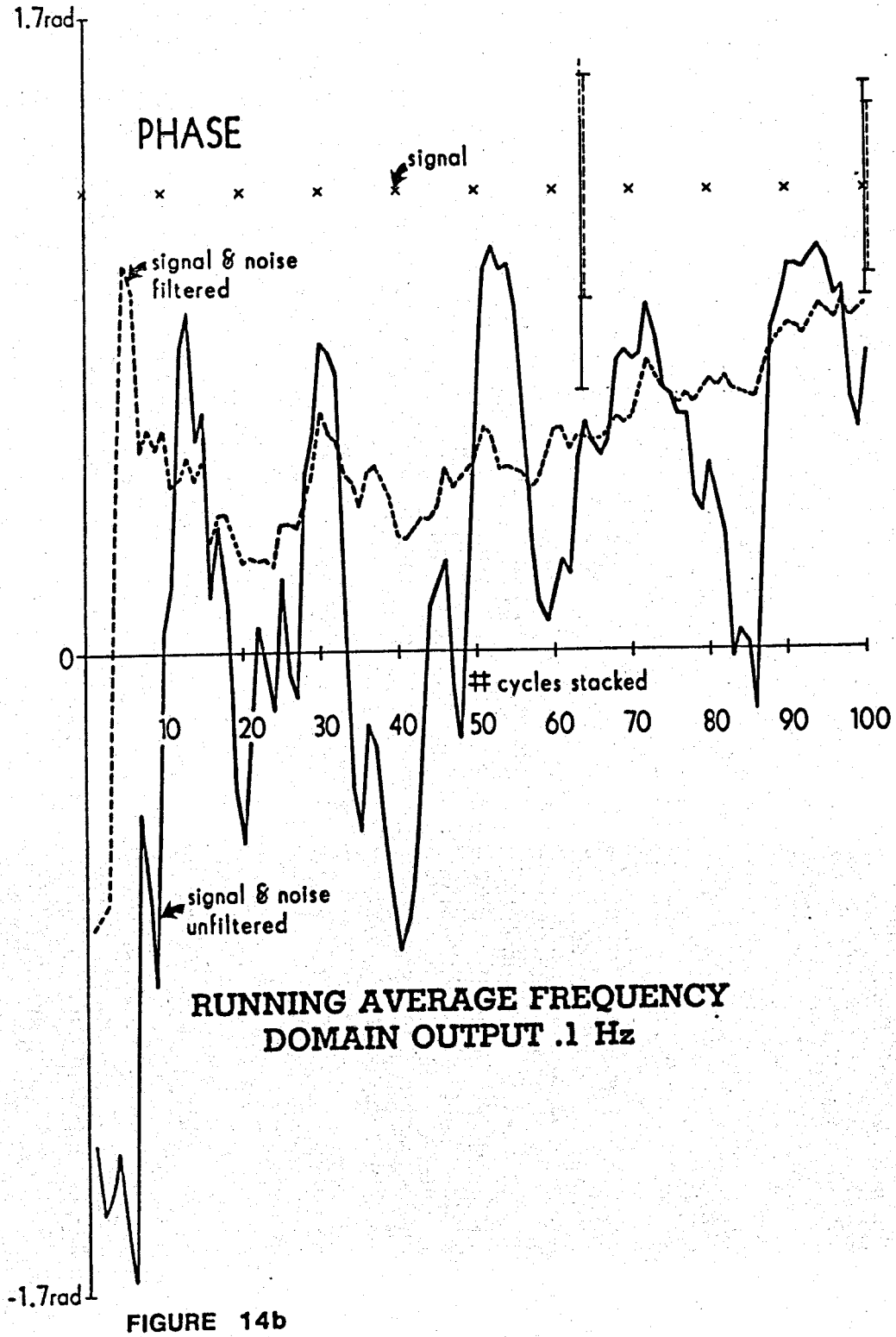

RUNNING AVERAGE FREQUENCY DOMAIN OUTPUT .1 Hz

FIGURE 14b

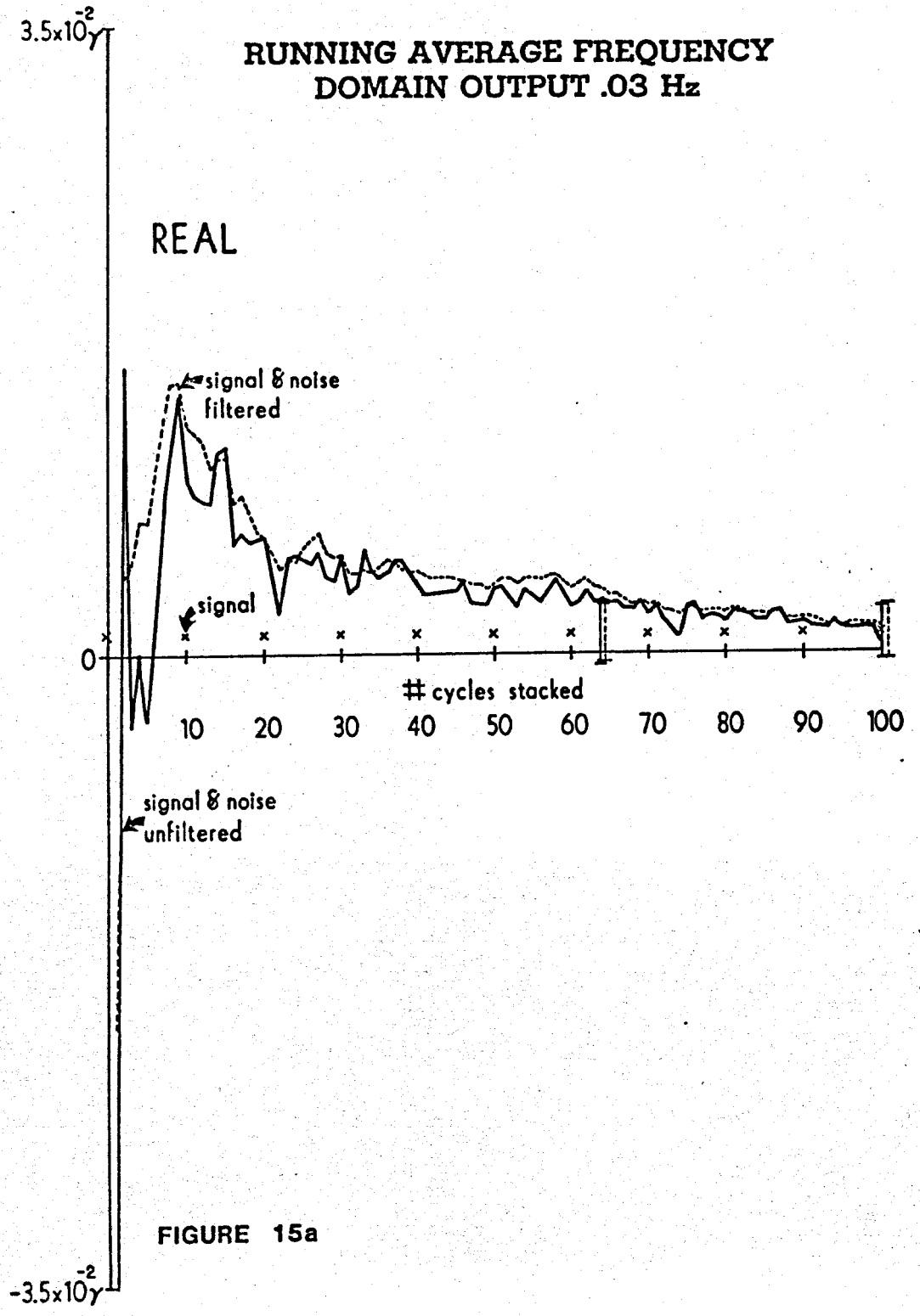
RUNNING AVERAGE FREQUENCY
DOMAIN OUTPUT .03 Hz
REAL
3.5x10^-2 γ
signal & noise
filtered
signal
0
cycles stacked
10
20
30
40
50
60
70
80
90
100
signal & noise
unfiltered
-3.5x10^-2 γ

FIGURE 15a

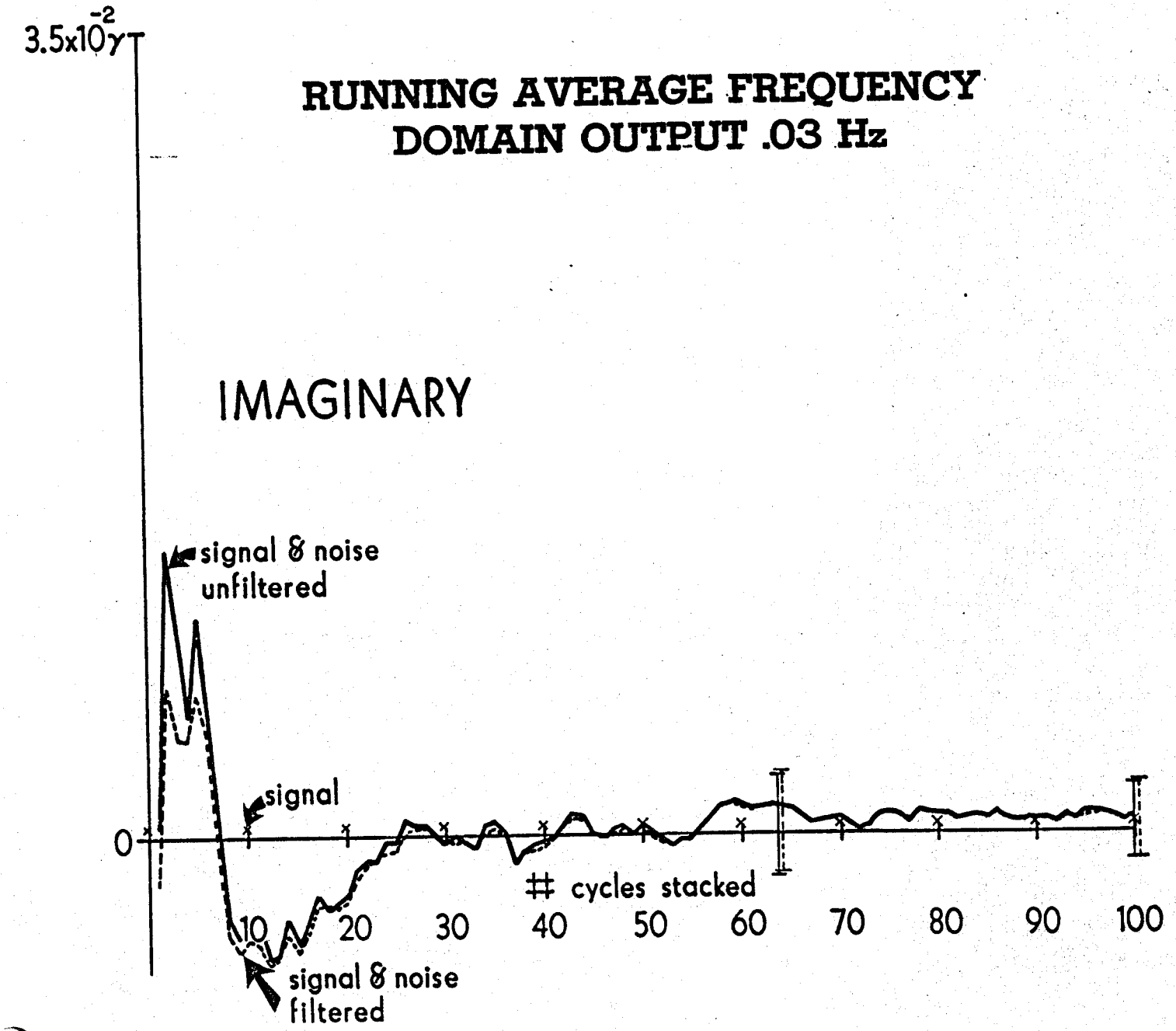
3.5x10⁻²γ
RUNNING AVERAGE FREQUENCY
DOMAIN OUTPUT .03 Hz
IMAGINARY
signal & noise
unfiltered
signal
0
cycles stacked
10
20
30
40
50
60
70
80
90
100
signal & noise
filtered

FIGURE 15b

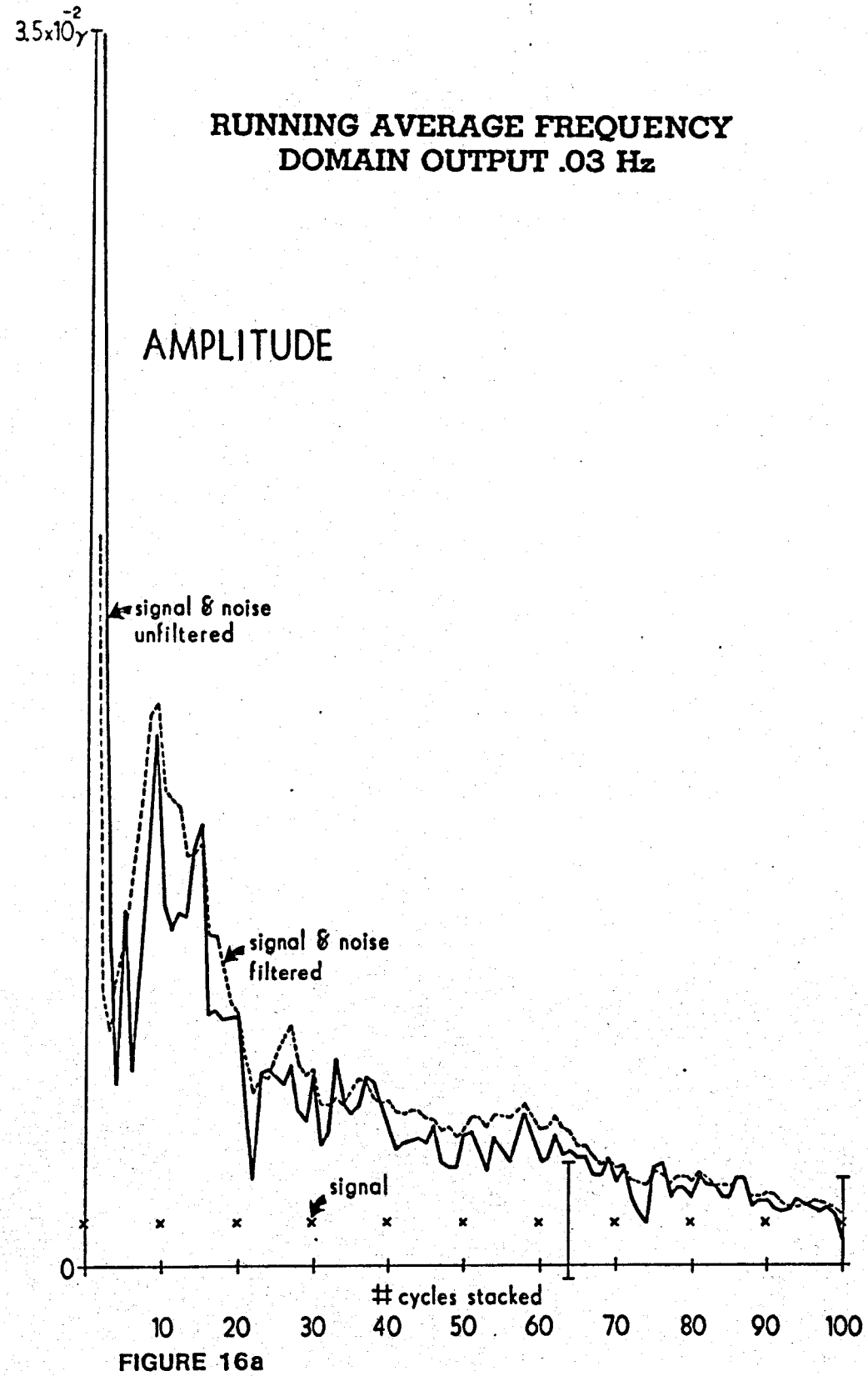
3.5x10^-2 γ
RUNNING AVERAGE FREQUENCY DOMAIN OUTPUT .03 Hz
AMPLITUDE
signal & noise unfiltered
signal & noise filtered
signal
0
cycles stacked
10 20 30 40 50 60 70 80 90 100

FIGURE 16a

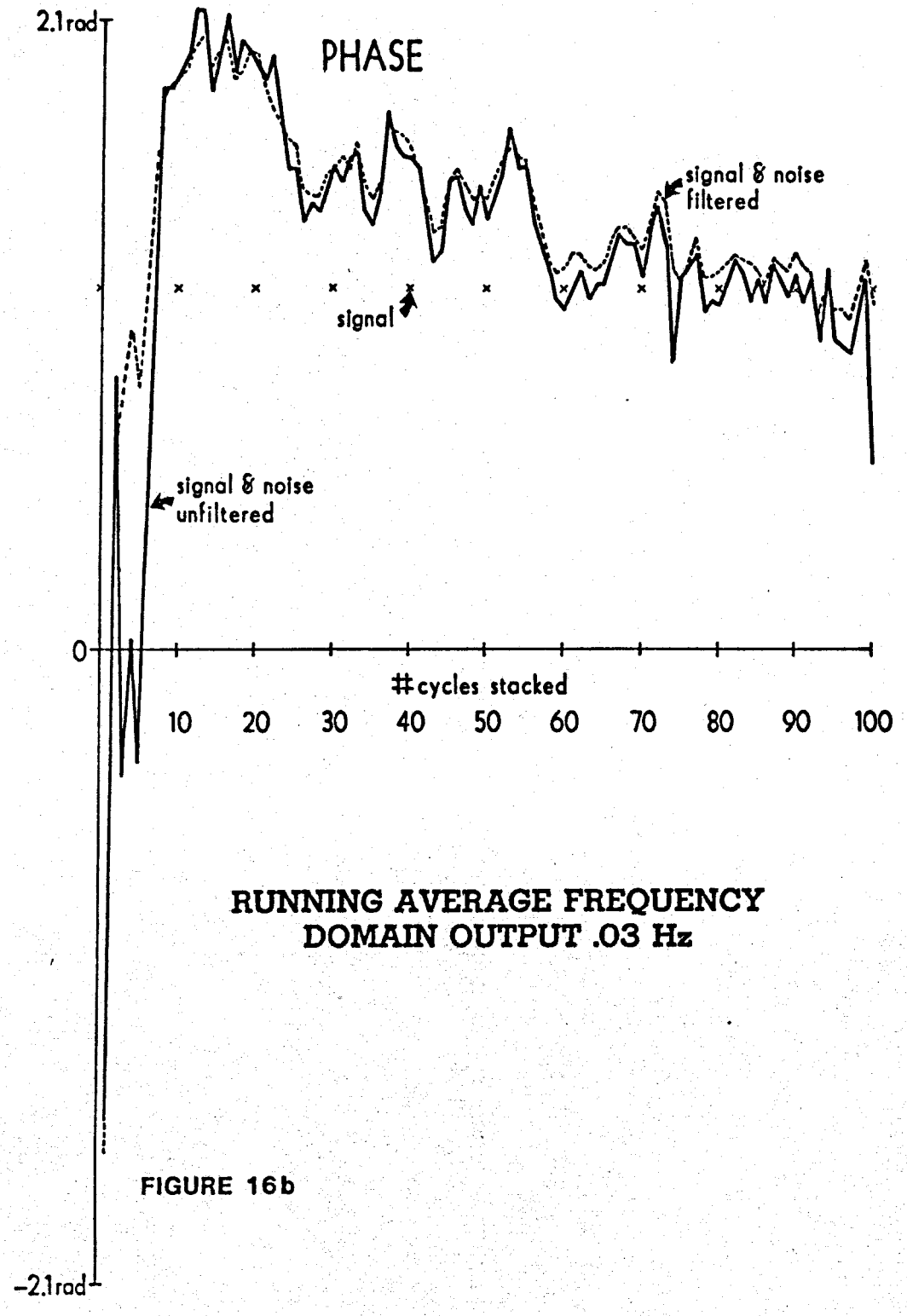

RUNNING AVERAGE FREQUENCY DOMAIN OUTPUT .03 Hz

FIGURE 16b

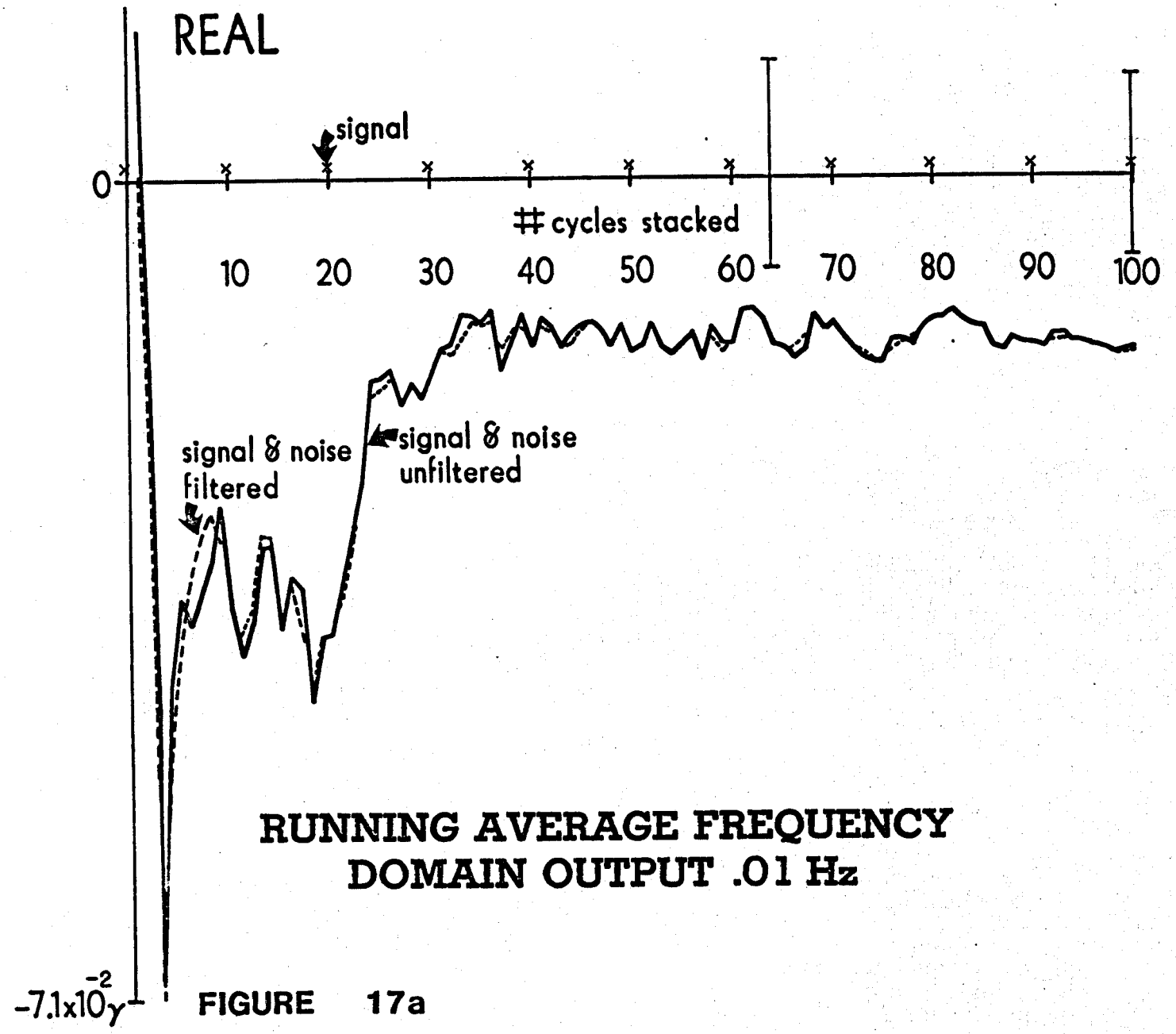

RUNNING AVERAGE FREQUENCY DOMAIN OUTPUT .01 Hz

FIGURE 17a

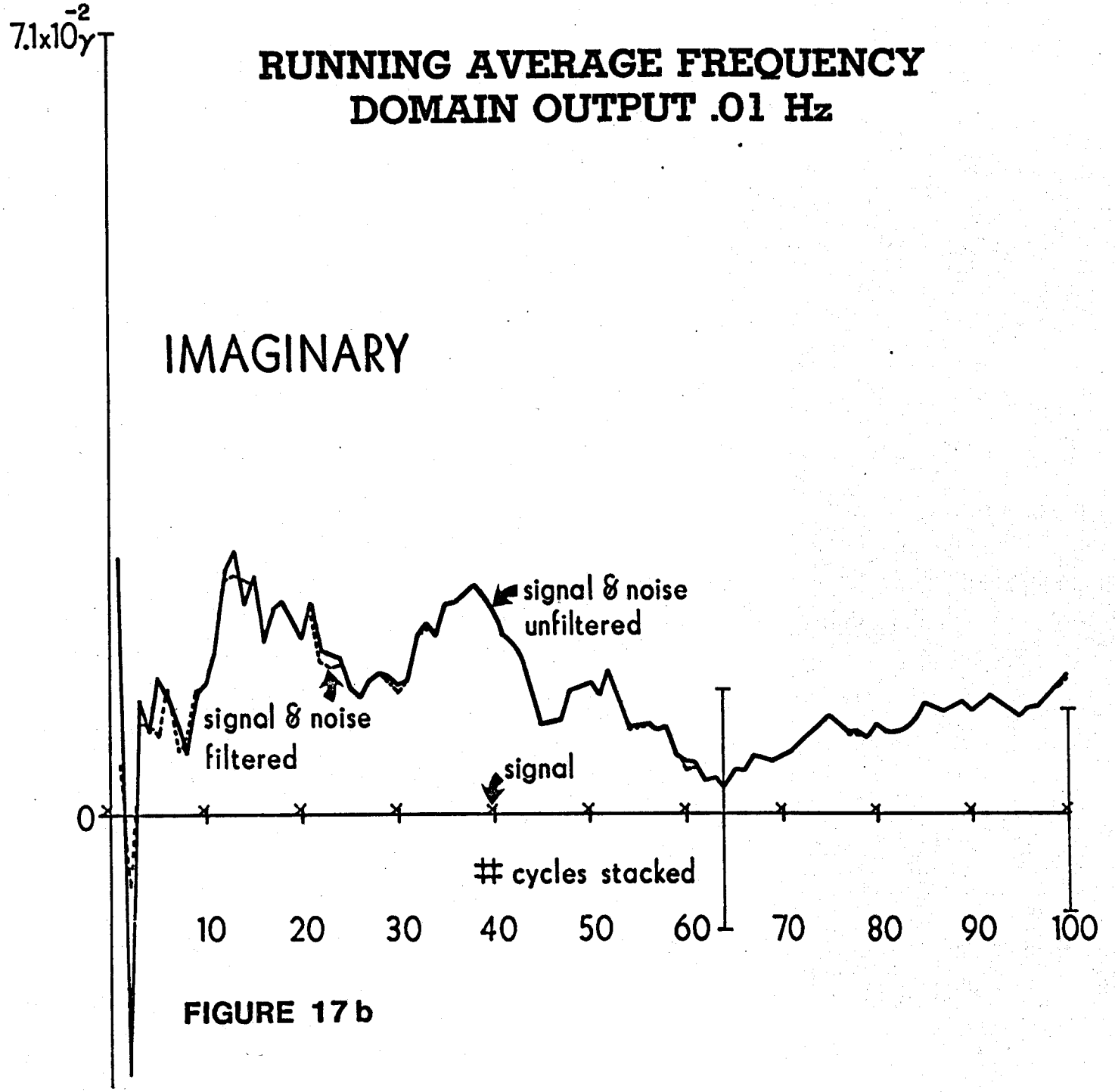
7.1x10^-2 γ
RUNNING AVERAGE FREQUENCY
DOMAIN OUTPUT .01 Hz
IMAGINARY
signal & noise
unfiltered
signal & noise
filtered
signal
0
cycles stacked
10
20
30
40
50
60
70
80
90
100

FIGURE 17 b

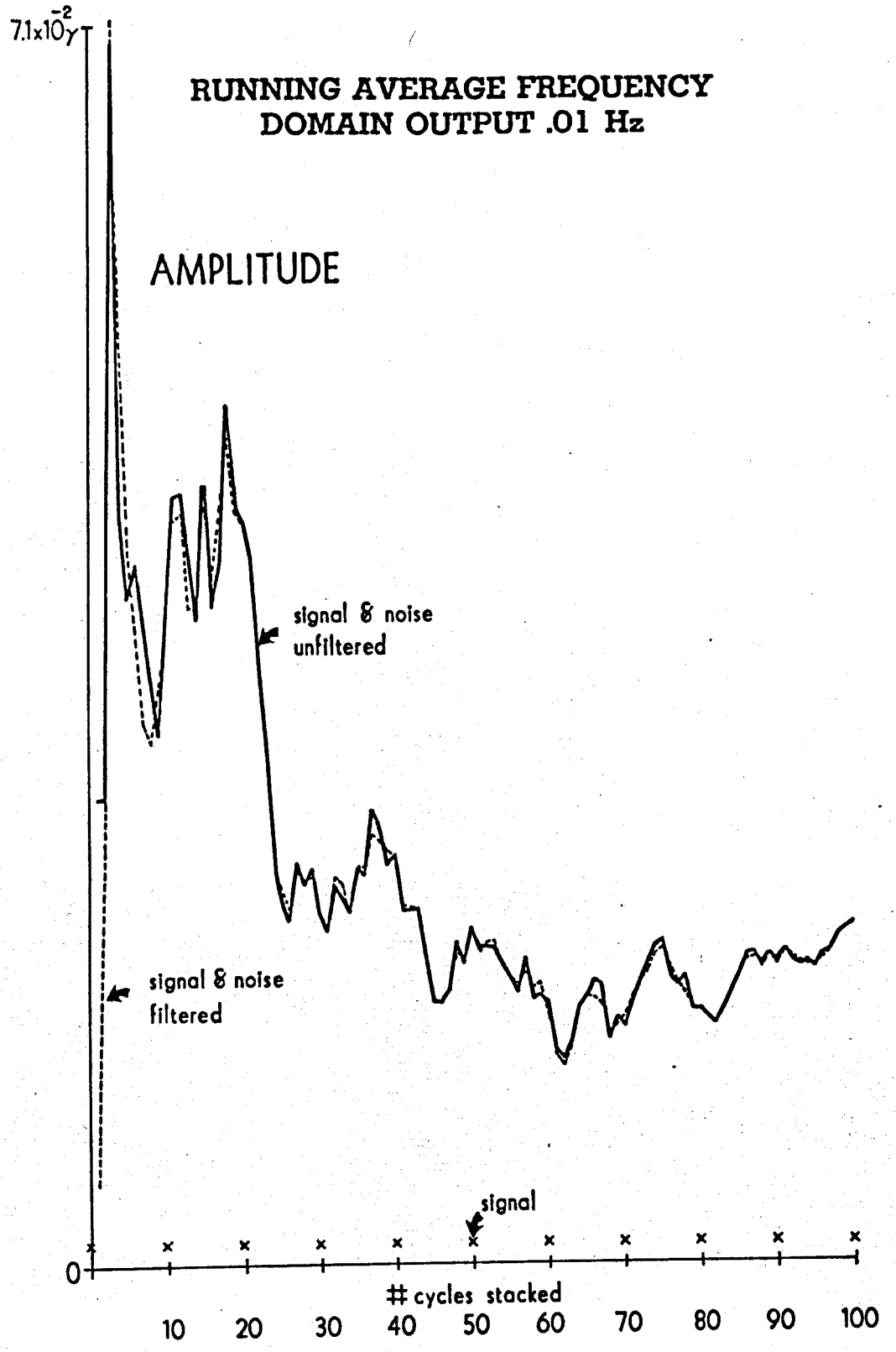
7.1x10⁻²γ
RUNNING AVERAGE FREQUENCY
DOMAIN OUTPUT .01 Hz
AMPLITUDE
signal & noise
unfiltered
signal & noise
filtered
signal
0
cycles stacked
10
20
30
40
50
60
70
80
90
100

FIGURE 18a

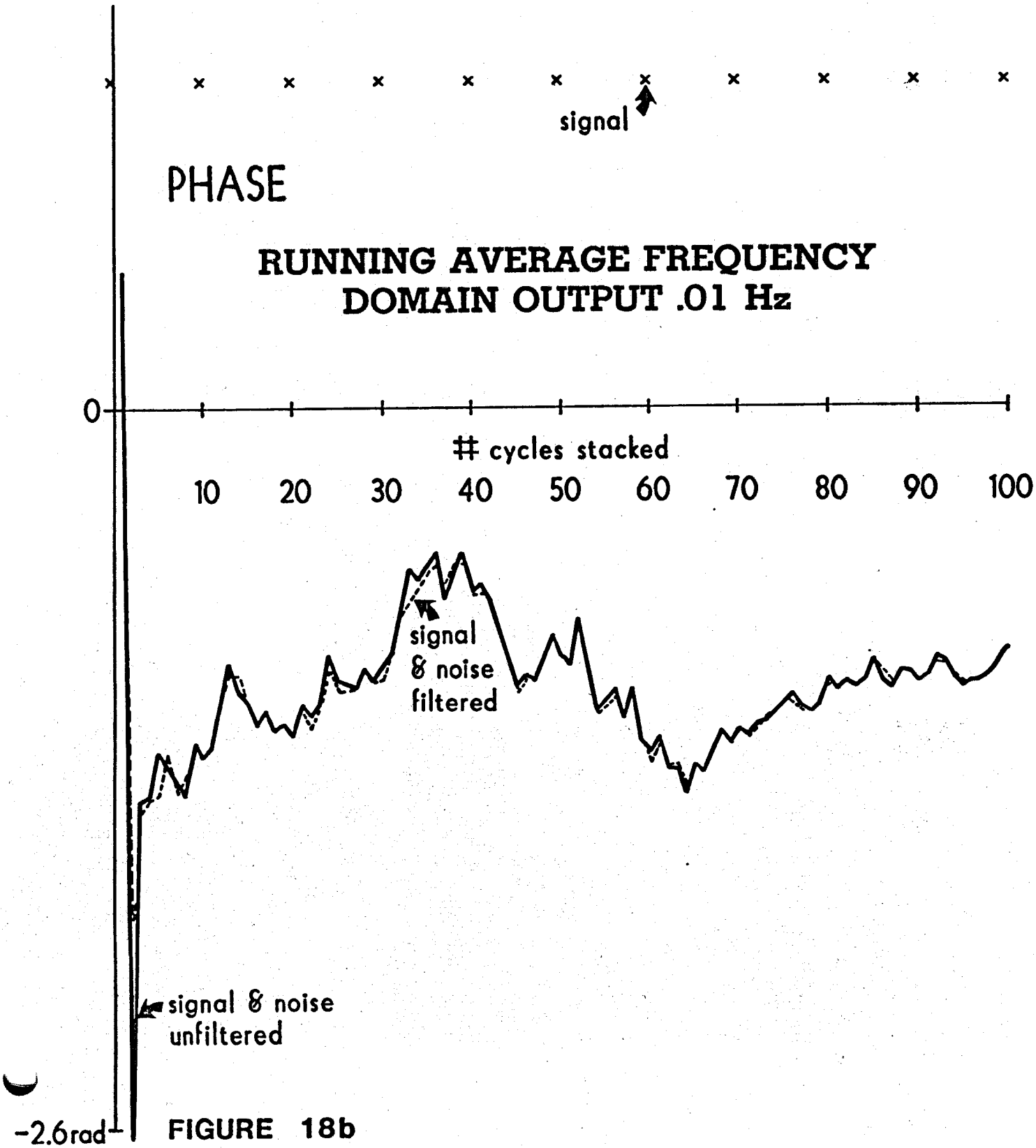
signal
PHASE
RUNNING AVERAGE FREQUENCY
DOMAIN OUTPUT .01 Hz
0
cycles stacked
10 20 30 40 50 60 70 80 90 100
signal
& noise
filtered
signal & noise
unfiltered
-2.6rad

FIGURE 18b

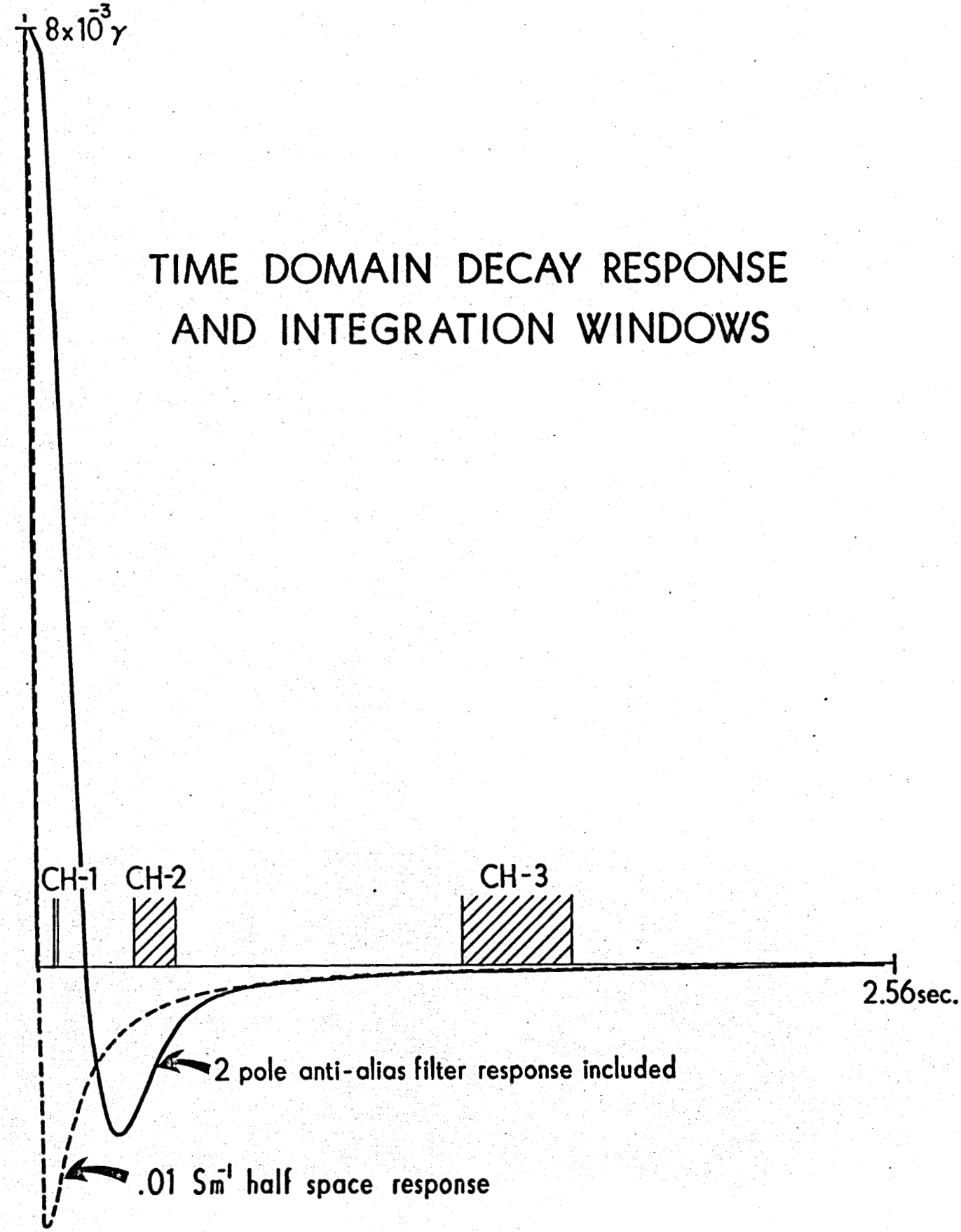
8x10⁻³γ
TIME DOMAIN DECAY RESPONSE
AND INTEGRATION WINDOWS
CH-1
CH-2
CH-3
2.56sec.
2 pole anti-alias filter response included
.01 Sm⁻¹ half space response

FIGURE 19

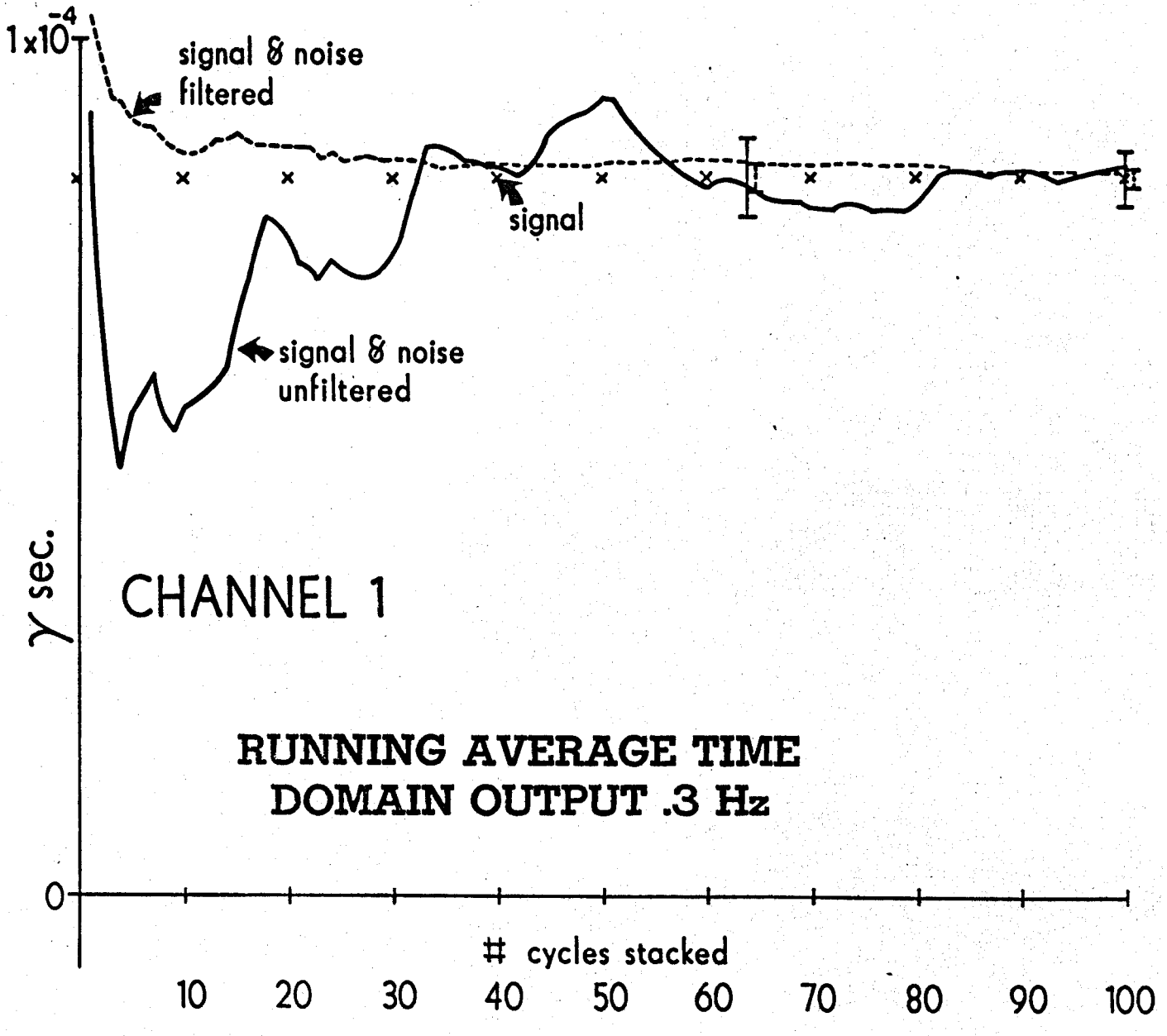
1x10⁻⁴
signal & noise
filtered
signal
signal & noise
unfiltered
γ sec.
CHANNEL 1
RUNNING AVERAGE TIME
DOMAIN OUTPUT .3 Hz
0
cycles stacked
10
20
30
40
50
60
70
80
90
100

FIGURE 20a

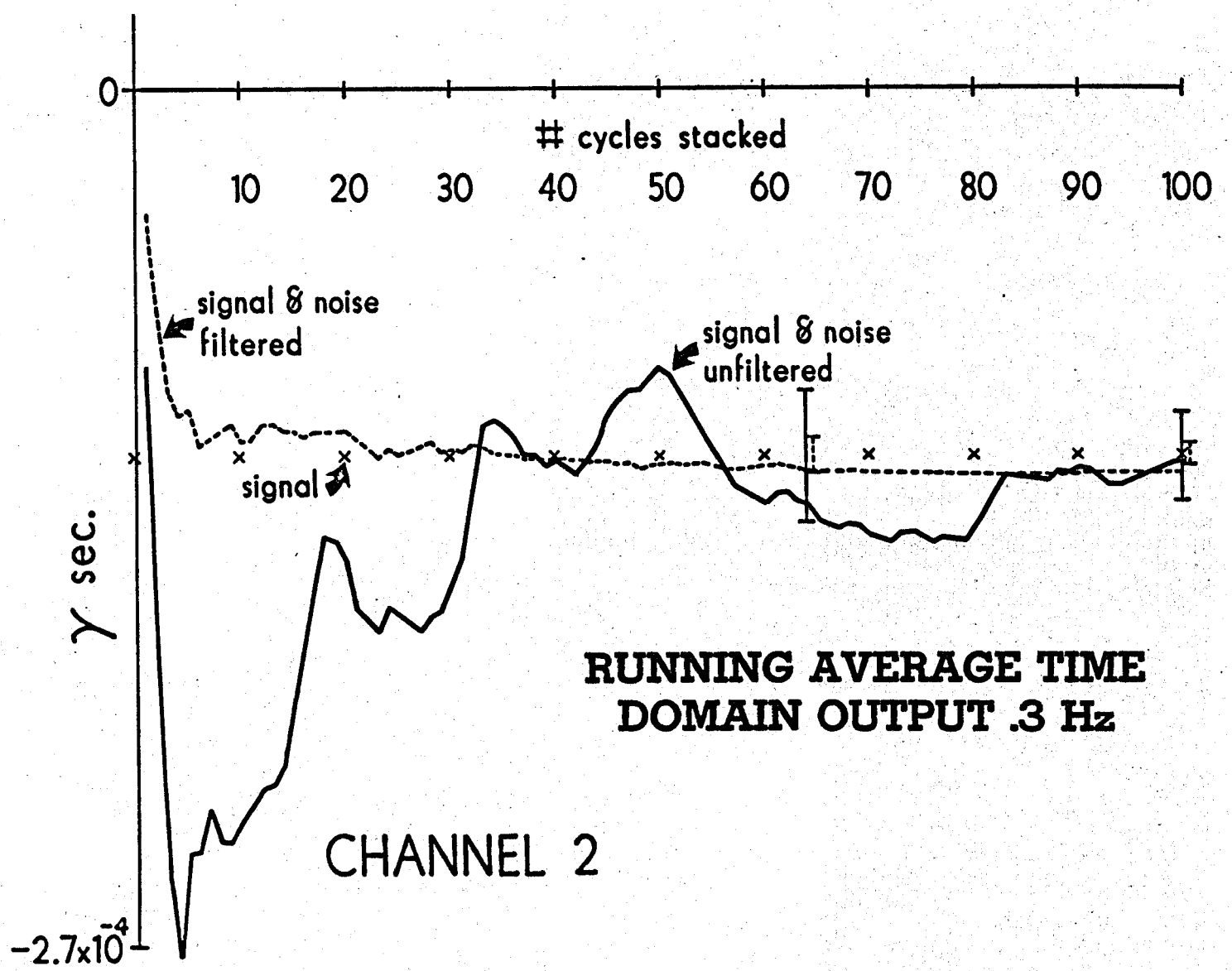
0
cycles stacked
10
20
30
40
50
60
70
80
90
100
signal & noise
filtered
signal & noise
unfiltered
signal
γ sec.
RUNNING AVERAGE TIME
DOMAIN OUTPUT .3 Hz
CHANNEL 2
-2.7x10^-4

FIGURE 20b

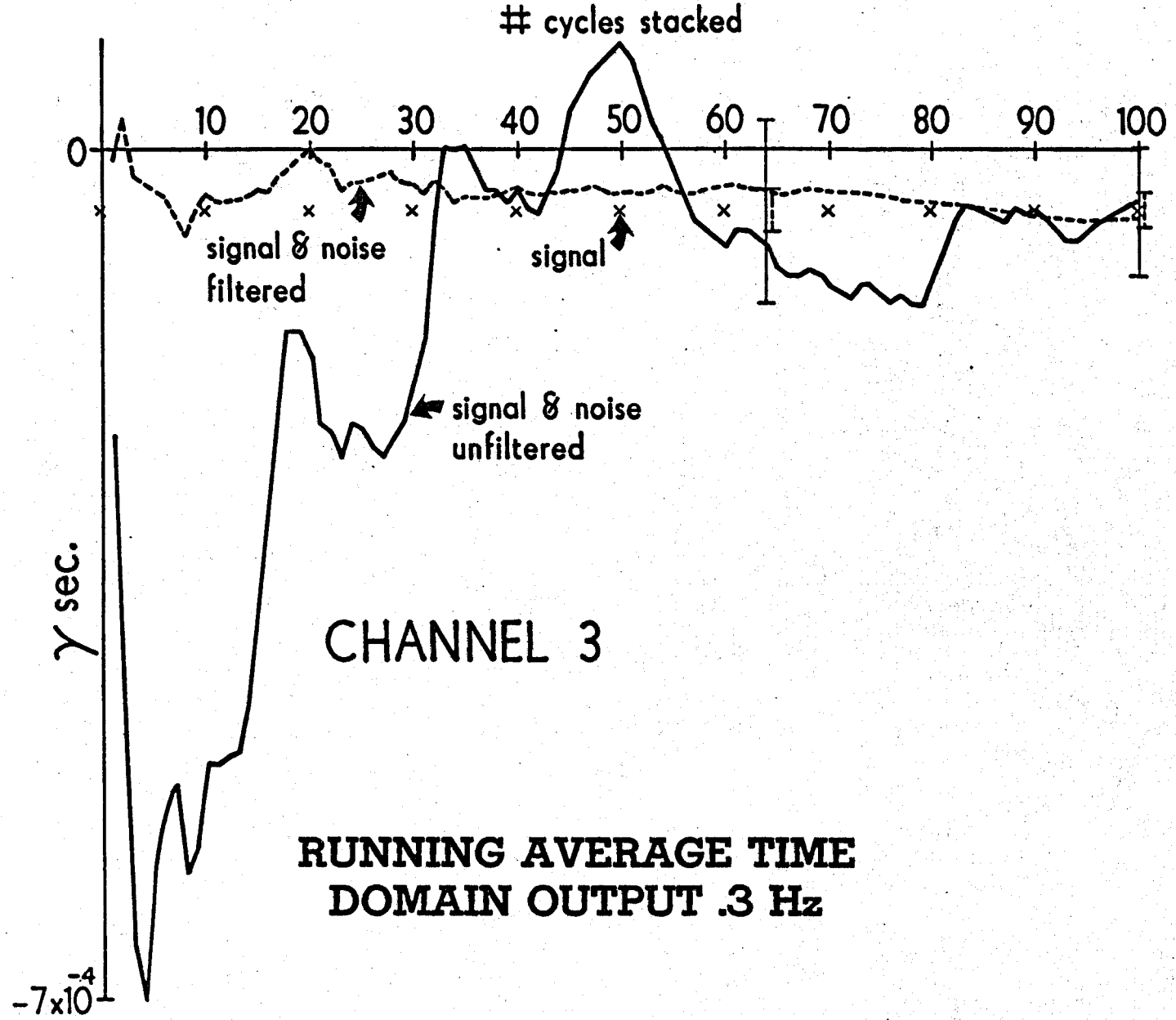
cycles stacked
10
20
30
40
50
60
70
80
90
100
0
signal & noise
filtered
signal
signal & noise
unfiltered
γ sec.
CHANNEL 3
RUNNING AVERAGE TIME
DOMAIN OUTPUT .3 Hz
-7x10^-4

FIGURE 20c

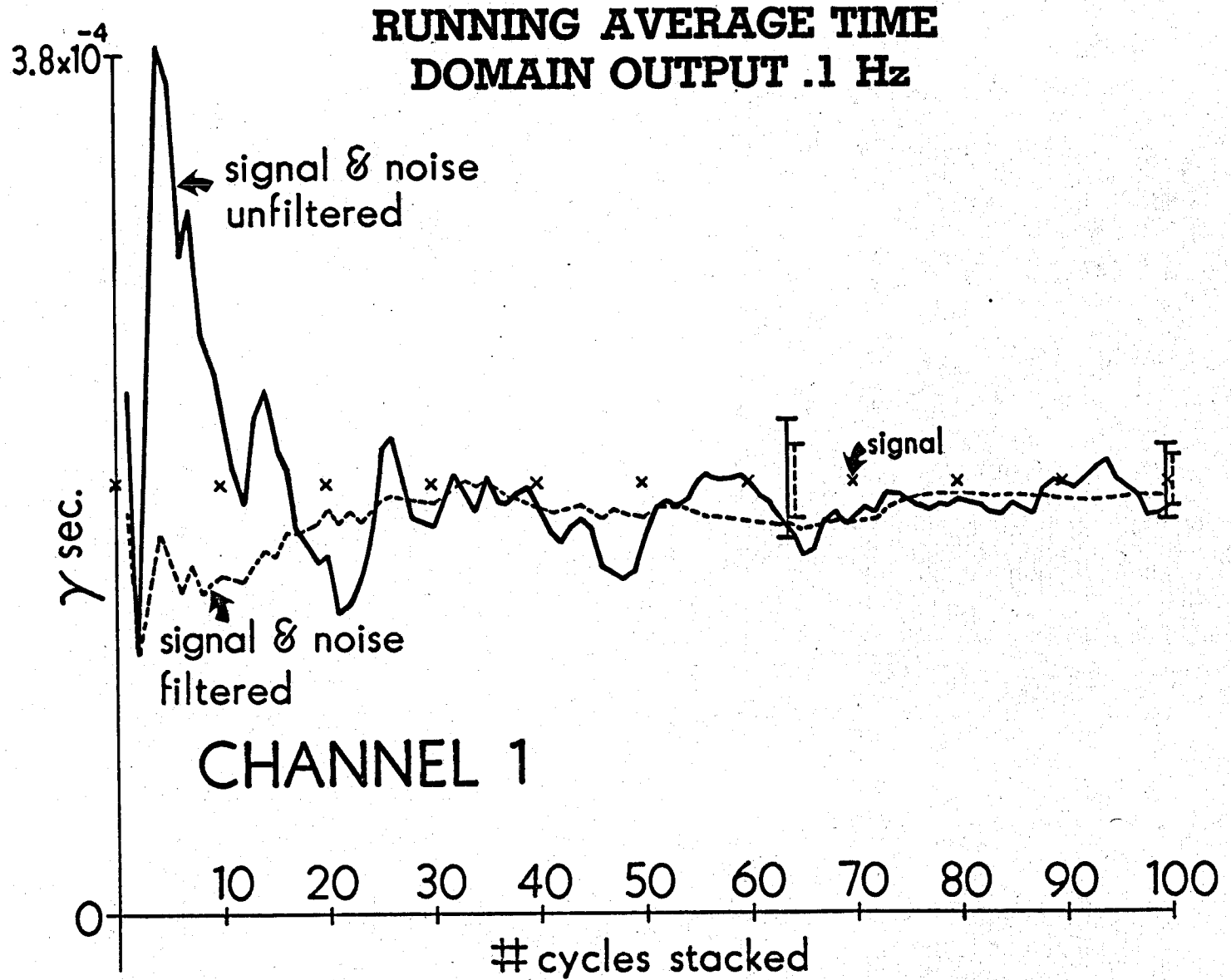
RUNNING AVERAGE TIME
DOMAIN OUTPUT .1 Hz
3.8x10^-4
signal & noise
unfiltered
signal
signal & noise
filtered
γ sec.
CHANNEL 1
0
10 20 30 40 50 60 70 80 90 100
cycles stacked

FIGURE 21a

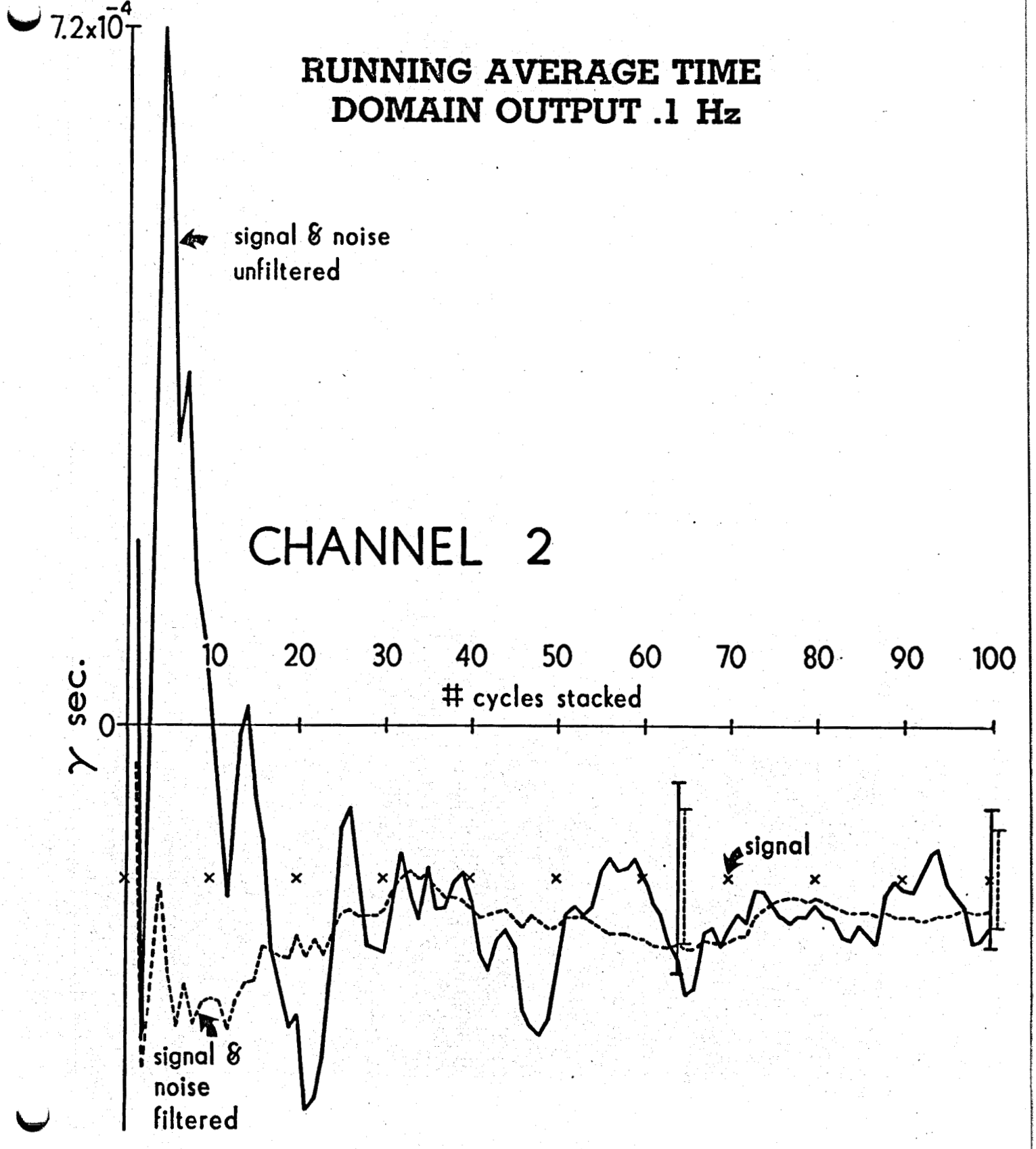
7.2x10⁻⁴
RUNNING AVERAGE TIME
DOMAIN OUTPUT .1 Hz
signal & noise
unfiltered
CHANNEL 2
10
20
30
40
50
60
70
80
90
100
cycles stacked
γ sec.
0
signal
signal &
noise
filtered

FIGURE 21b

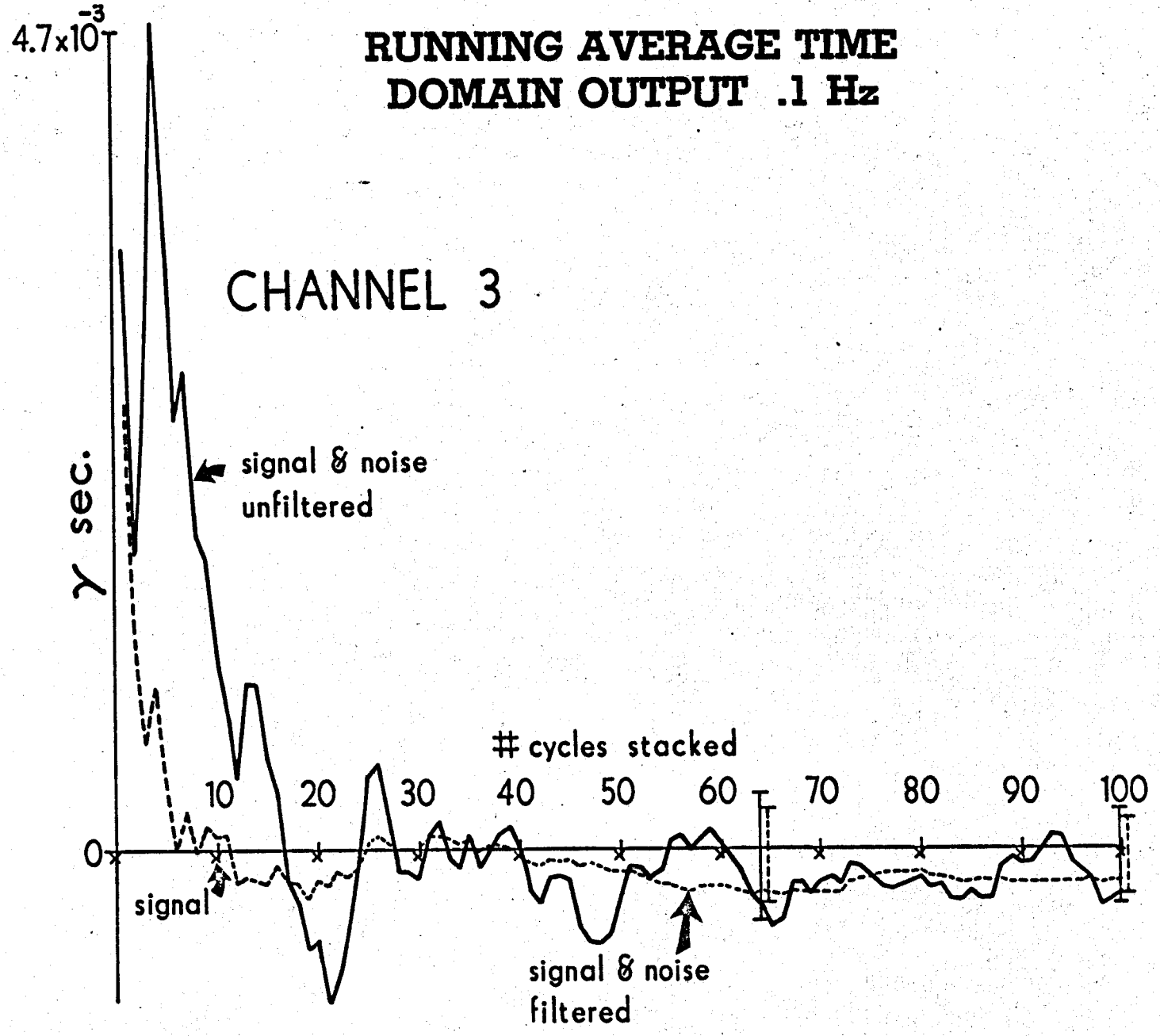
RUNNING AVERAGE TIME DOMAIN OUTPUT .1 Hz
4.7x10⁻³
CHANNEL 3
γ sec.
signal & noise unfiltered
cycles stacked
10
20
30
40
50
60
70
80
90
100
0
signal
signal & noise filtered

FIGURE 21c

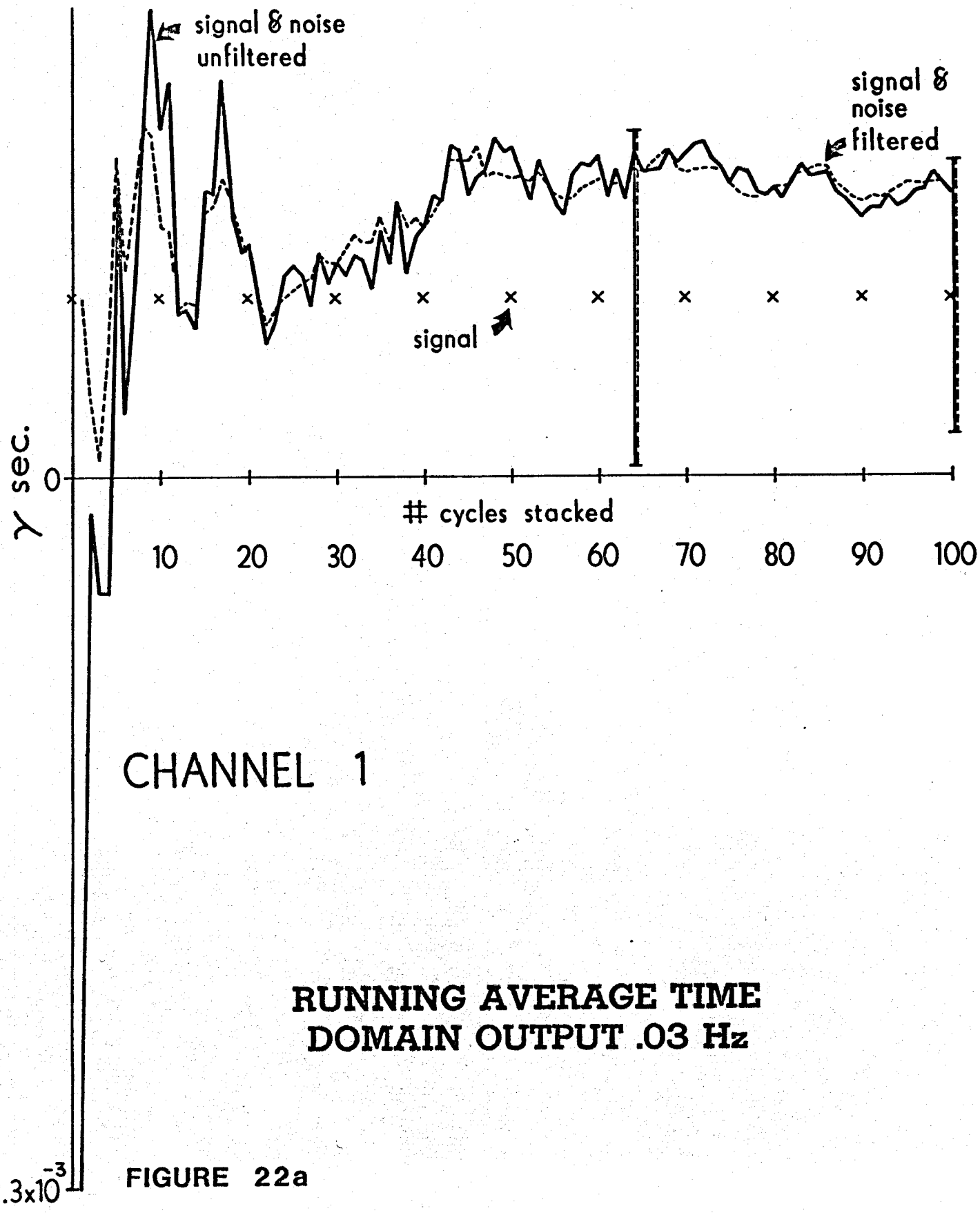

RUNNING AVERAGE TIME DOMAIN OUTPUT .03 Hz

FIGURE 22a

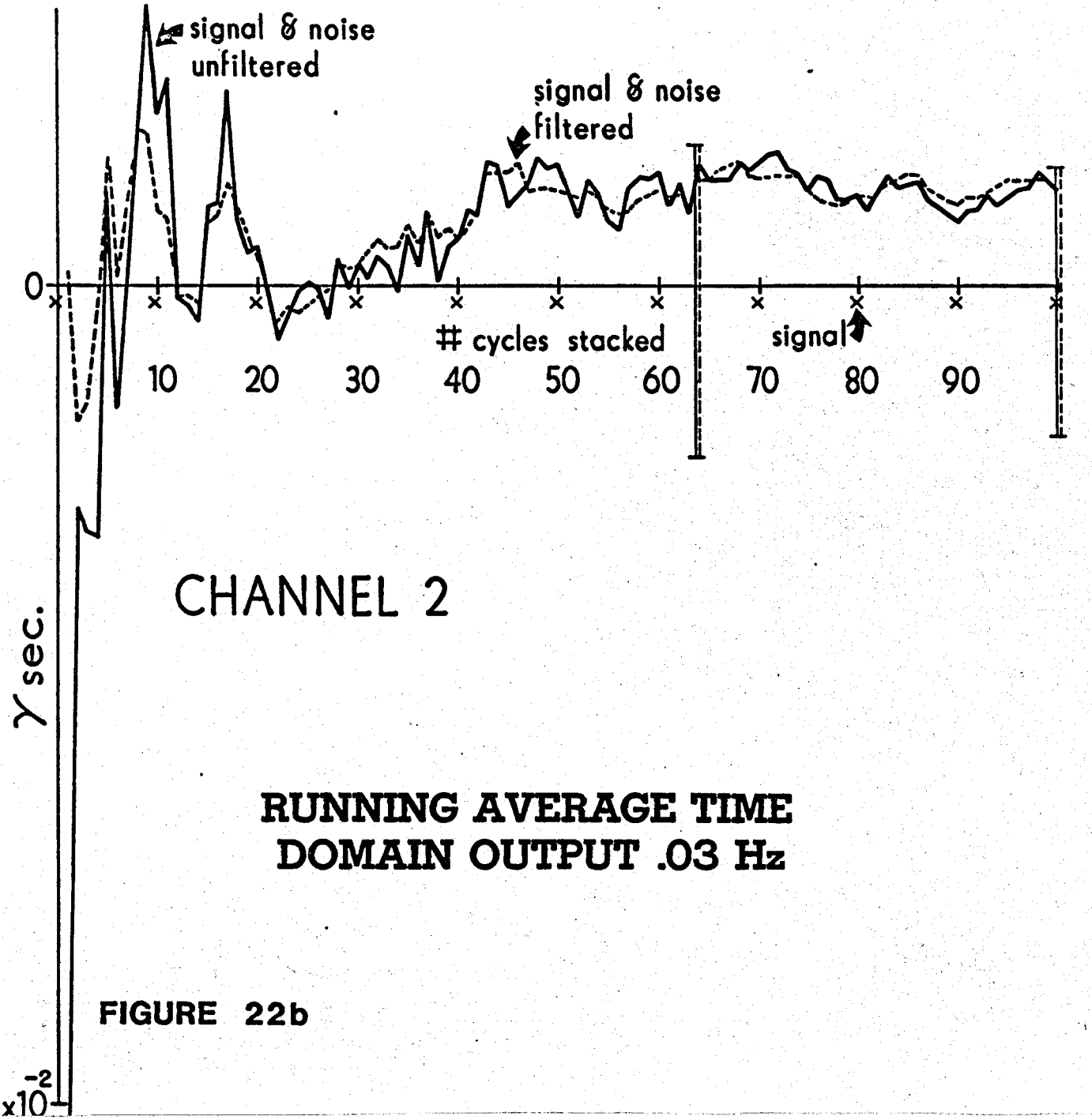

RUNNING AVERAGE TIME DOMAIN OUTPUT .03 Hz

FIGURE 22b

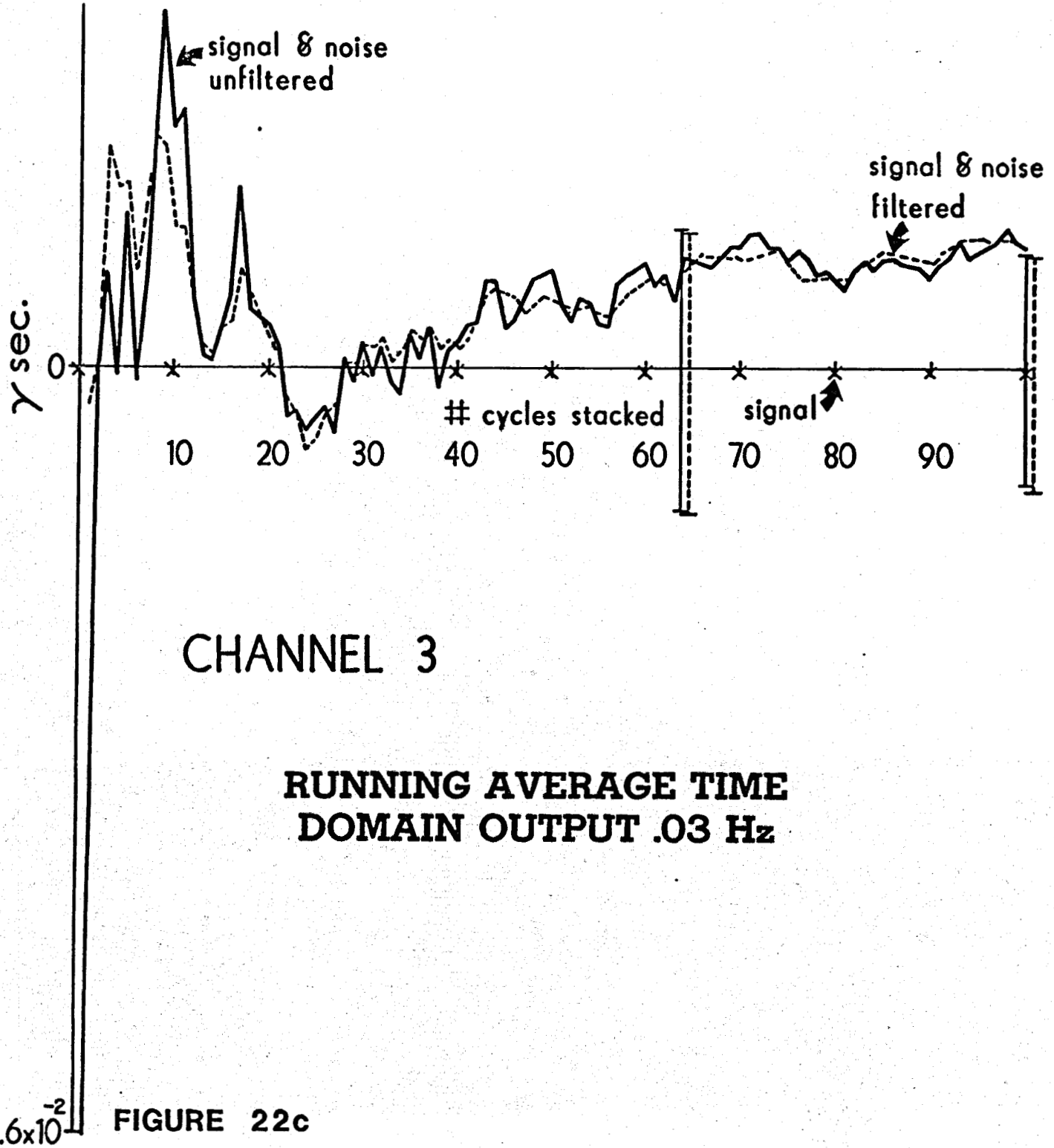

CHANNEL 3

RUNNING AVERAGE TIME DOMAIN OUTPUT .03 Hz

FIGURE 22c

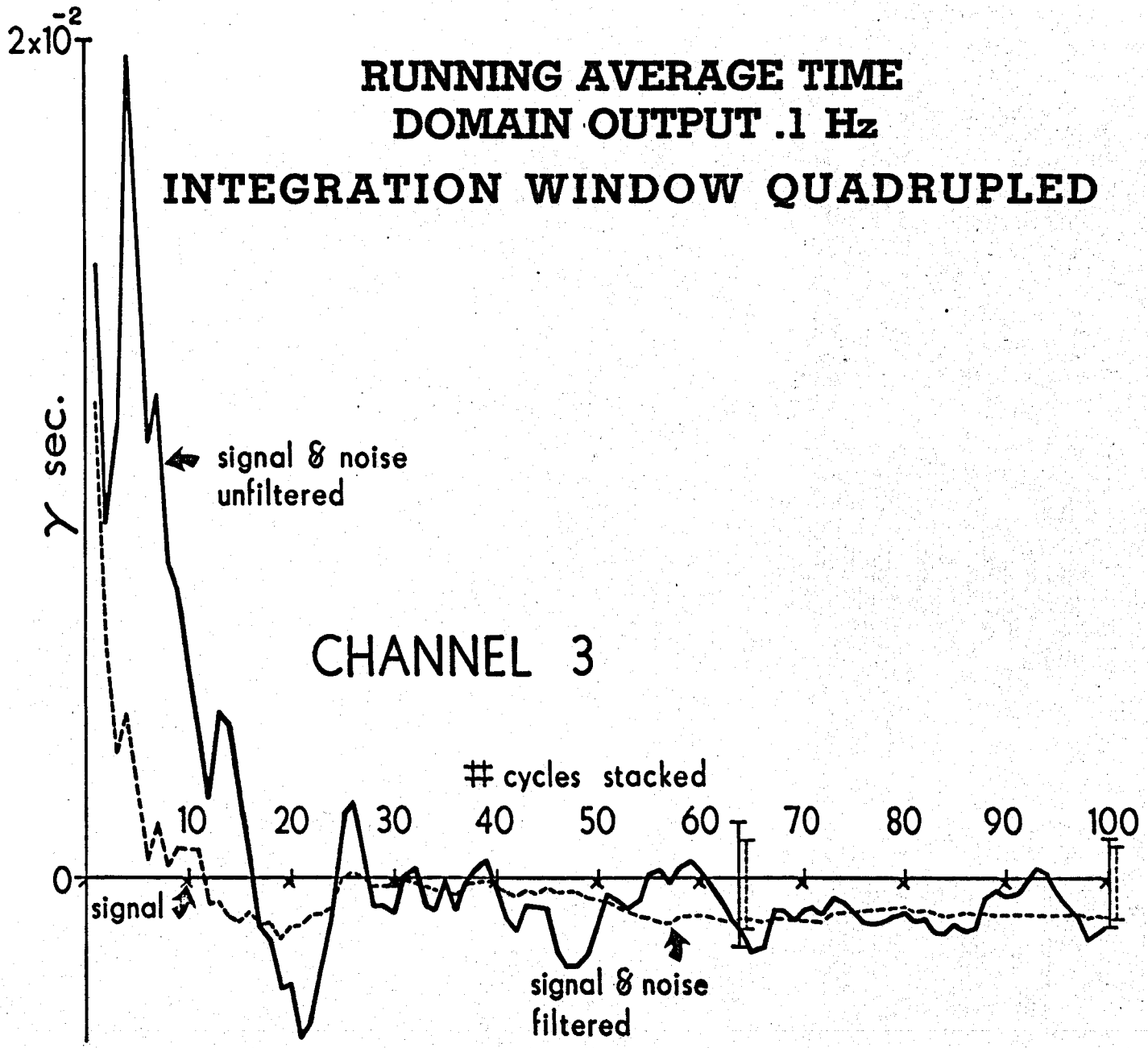
RUNNING AVERAGE TIME
DOMAIN OUTPUT .1 Hz
INTEGRATION WINDOW QUADRUPLED
2x10⁻²
γ sec.
signal & noise
unfiltered
CHANNEL 3
cycles stacked
10
20
30
40
50
60
70
80
90
100
0
signal
signal & noise
filtered

FIGURE 23

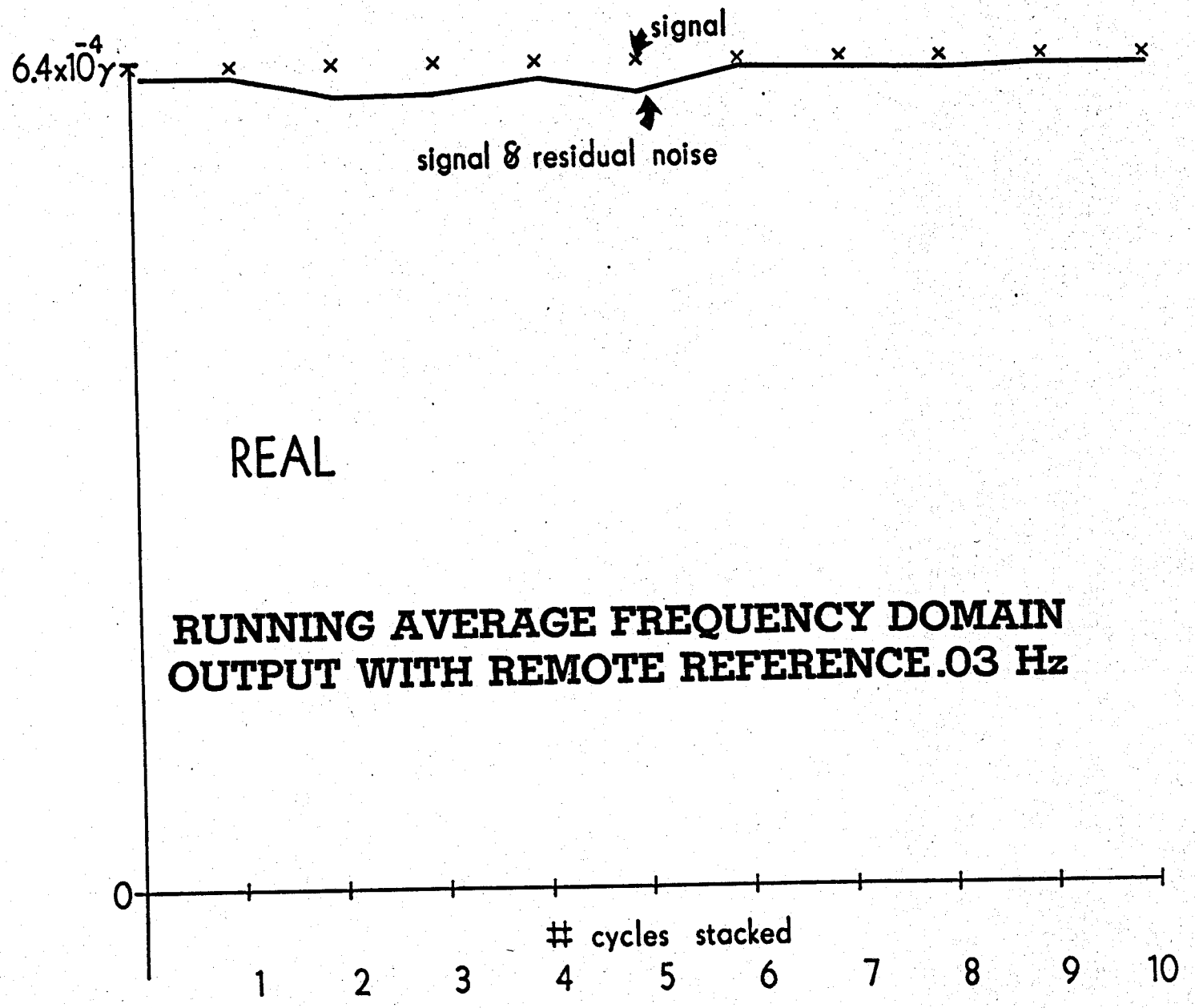
signal
6.4x10⁻⁴γ
signal & residual noise
REAL
RUNNING AVERAGE FREQUENCY DOMAIN
OUTPUT WITH REMOTE REFERENCE.03 Hz
0
cycles stacked
1 2 3 4 5 6 7 8 9 10

FIGURE 24a

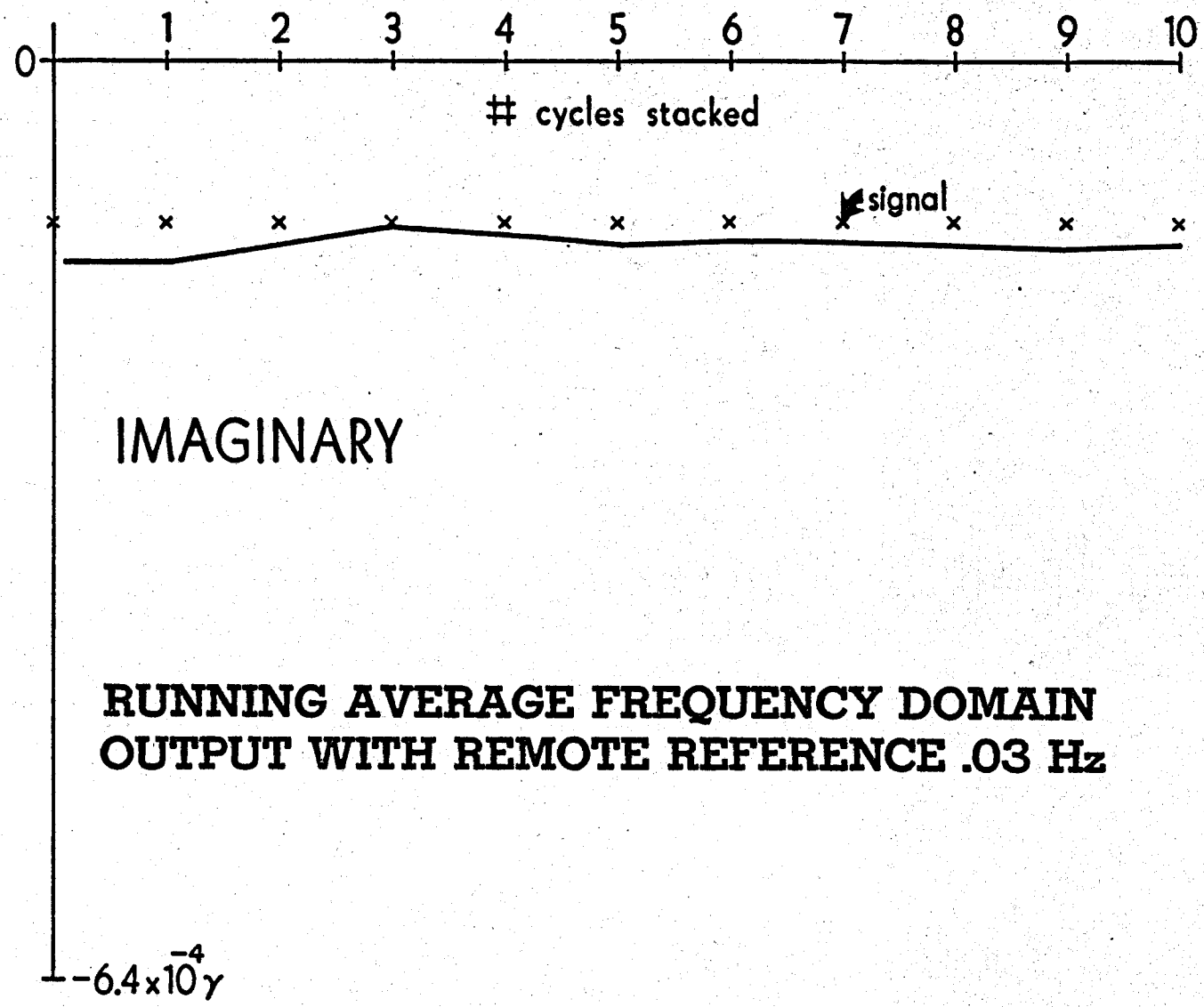
0
1
2
3
4
5
6
7
8
9
10
cycles stacked
signal
IMAGINARY
RUNNING AVERAGE FREQUENCY DOMAIN
OUTPUT WITH REMOTE REFERENCE .03 Hz
$-6.4 \times 10^{-4}\gamma$

FIGURE 24b

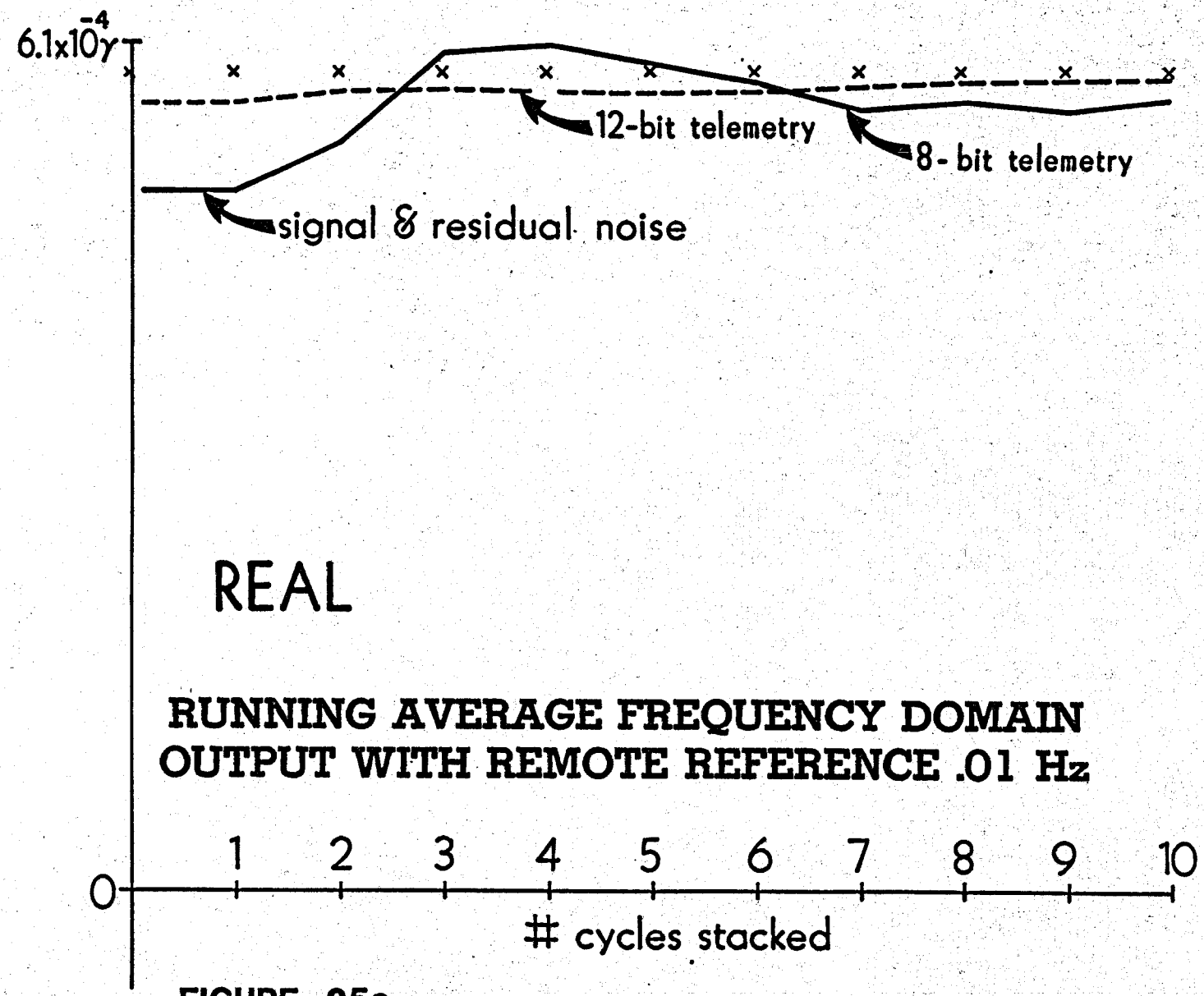
6.1x10⁻⁴γ
12-bit telemetry
8-bit telemetry
signal & residual noise
REAL
RUNNING AVERAGE FREQUENCY DOMAIN
OUTPUT WITH REMOTE REFERENCE .01 Hz
0
1
2
3
4
5
6
7
8
9
10
cycles stacked

FIGURE 25a

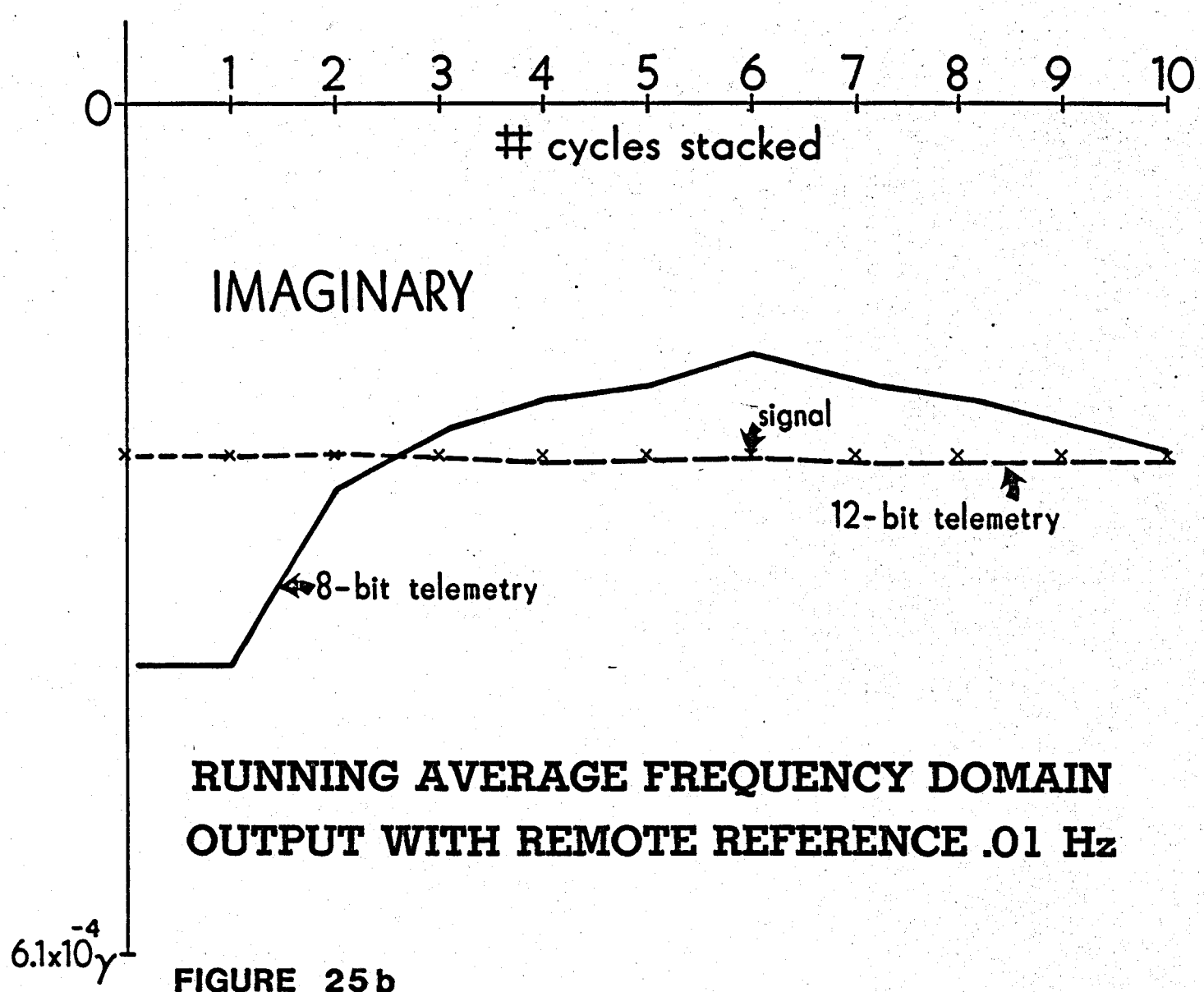

RUNNING AVERAGE FREQUENCY DOMAIN OUTPUT WITH REMOTE REFERENCE .01 Hz

FIGURE 25b

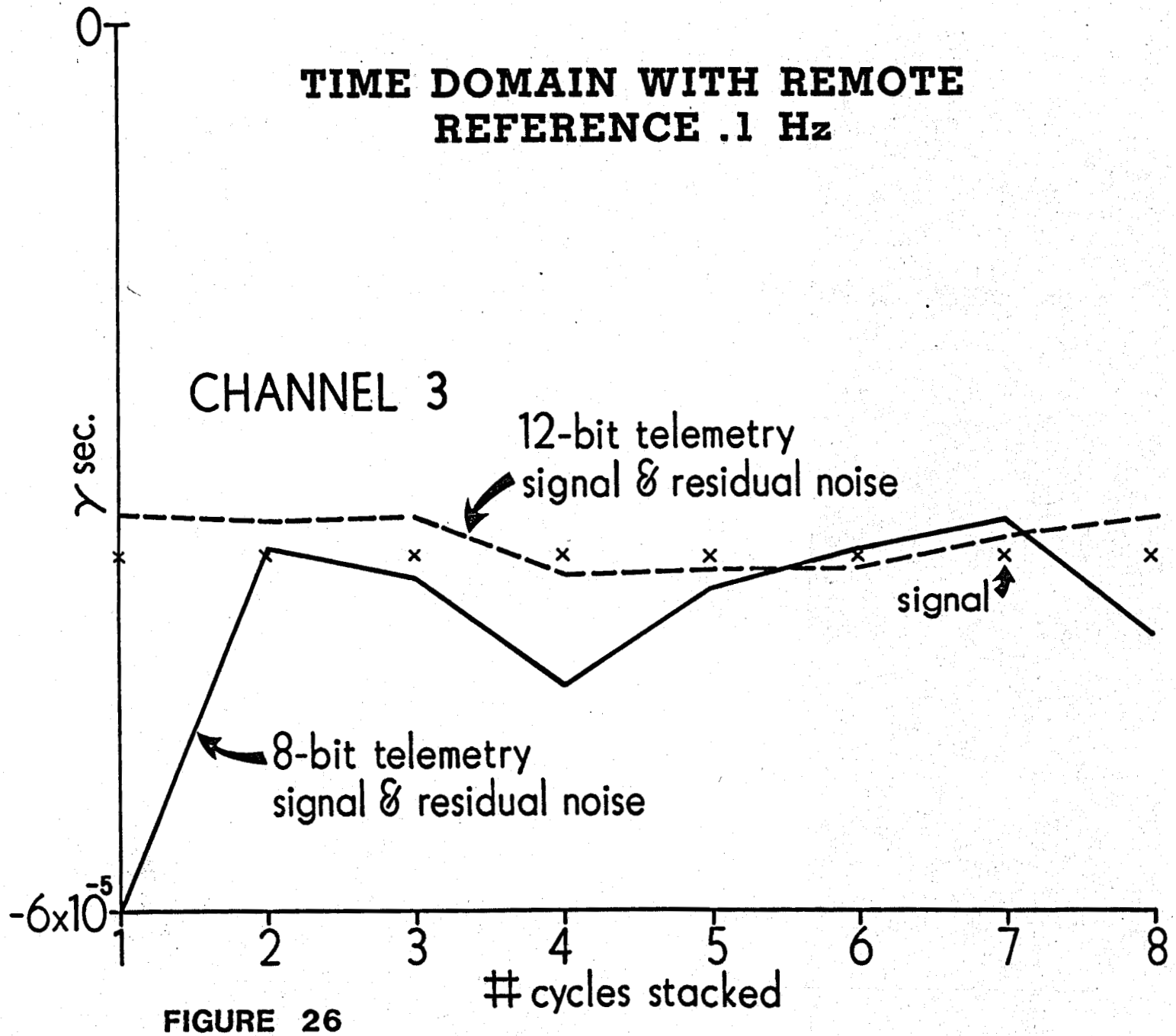
TIME DOMAIN WITH REMOTE REFERENCE .1 Hz
0
CHANNEL 3
γ sec.
12-bit telemetry signal & residual noise
signal
8-bit telemetry signal & residual noise
-6x10⁻⁵
1
2
3
4
5
6
7
8
cycles stacked

FIGURE 26

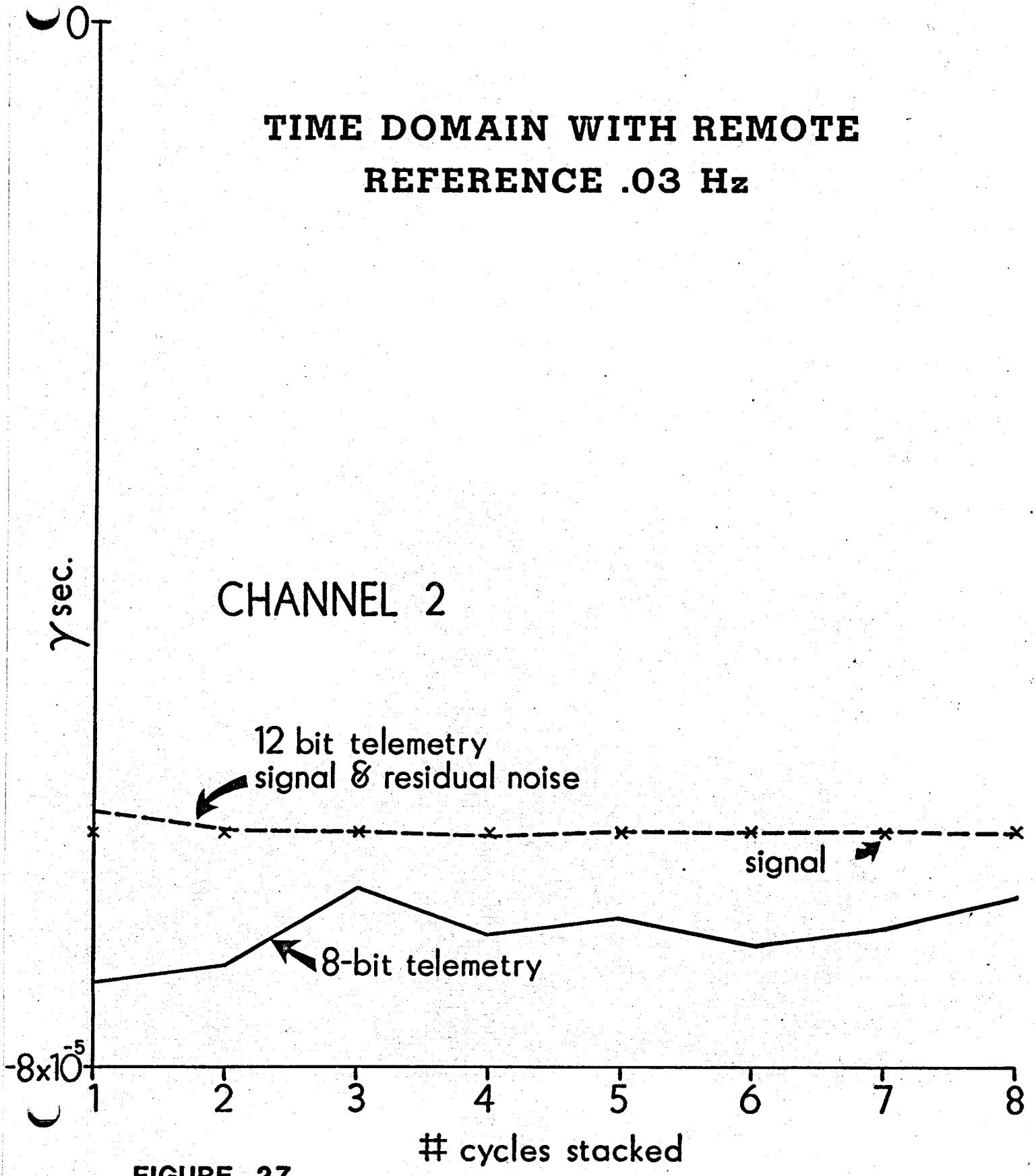
TIME DOMAIN WITH REMOTE
REFERENCE .03 Hz
0
γ sec.
CHANNEL 2
12 bit telemetry
signal & residual noise
signal
8-bit telemetry
-8x10⁻⁵
1
2
3
4
5
6
7
8
cycles stacked

FIGURE 27

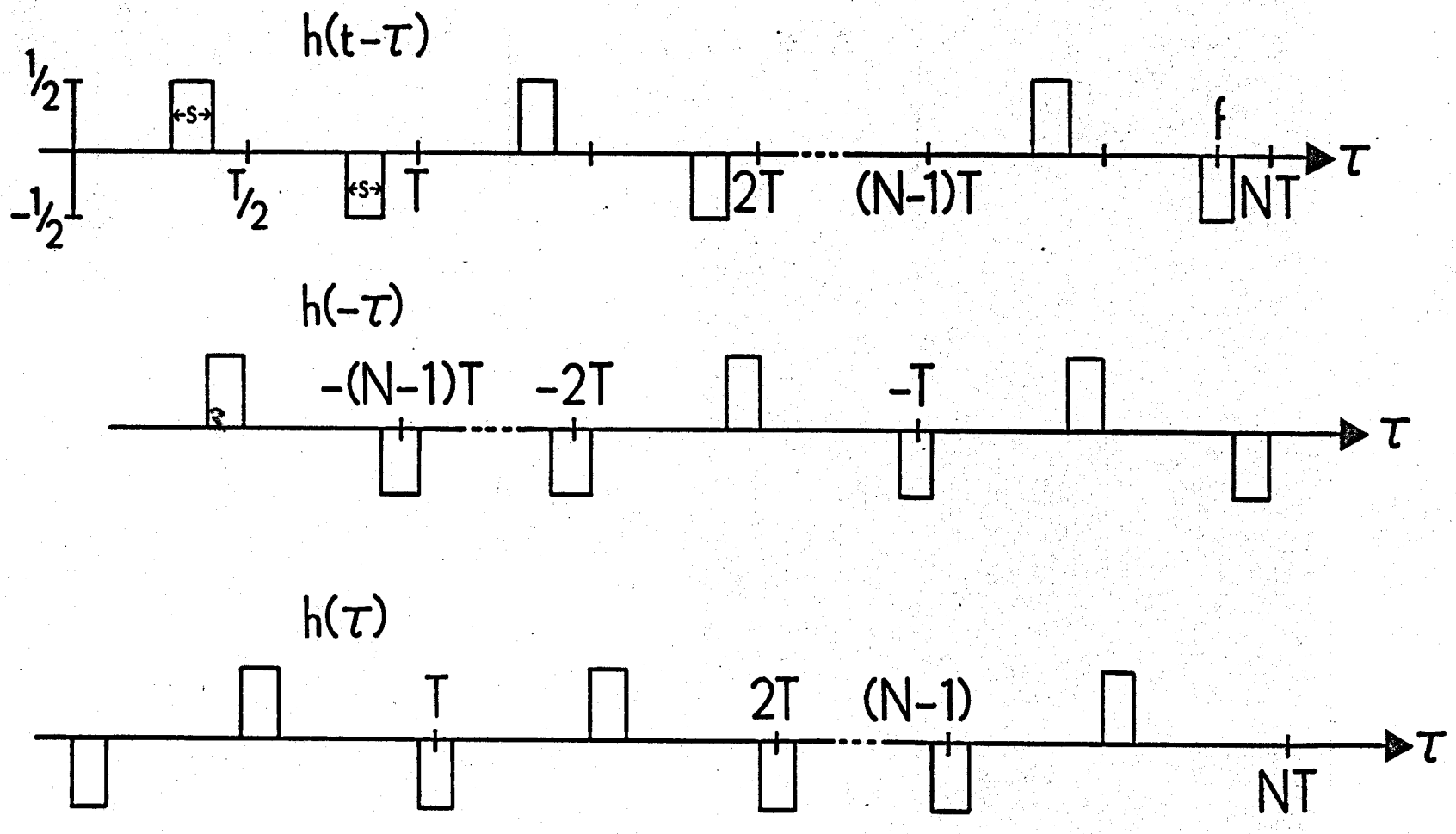

FIGURE A1